



Publicly Accessible Penn Dissertations

---


1-1-2014

# Nanoparticle-Shelled Bubbles for Lightweight Materials

Teresa Brugarolas Brufau

University of Pennsylvania, [teresabr@seas.upenn.edu](mailto:teresabr@seas.upenn.edu)

Follow this and additional works at: <http://repository.upenn.edu/edissertations>

 Part of the [Chemical Engineering Commons](#), [Mechanical Engineering Commons](#), and the [Mechanics of Materials Commons](#)

---

## Recommended Citation

Brugarolas Brufau, Teresa, "Nanoparticle-Shelled Bubbles for Lightweight Materials" (2014). *Publicly Accessible Penn Dissertations*. 1215.

<http://repository.upenn.edu/edissertations/1215>

This paper is posted at Scholarly Commons. <http://repository.upenn.edu/edissertations/1215>

For more information, please contact [libraryrepository@pobox.upenn.edu](mailto:libraryrepository@pobox.upenn.edu).

---

# Nanoparticle-Shelled Bubbles for Lightweight Materials

## **Abstract**

Lightweight materials that are mechanically robust are of great interest in automotive, aerospace, and construction industries. However due to the nature of materials, it is challenging to obtain materials that have high strength, stiffness and toughness, and light weight simultaneously. One approach that tries to address this limitation is the use of composite materials containing hollow microparticles, also known as syntactic foams. The incorporation of hollow microparticles decreases the density of the material at the same time that increases its specific strength. Conventional methods of fabrication of hollow particles involving bulk reactions result in high heterogeneity in geometry as well as mechanical properties, and little or no control over the shell nanostructure. This variability in the structure and properties of the hollow microparticles adversely affects the macroscopic properties of the syntactic foams and hinders the understanding of the structure-property relationship. The use of microfluidics for the generation of shelled-bubbles addresses these limitations. This microfluidic technique, in contrast to bulk methods, is based on single droplet formation, allowing for the generation of highly uniform bubbles, and enabling the assembly of nanoparticles at the interface forming stable nanoparticle-shelled bubbles. Microfluidics allow a precise control over the geometry, nanostructure and properties of the shelled-bubbles, further enabling the functionalization of the shell surface to present amphiphilicity, or the modification of the shell structure with thermal processes to enhance their mechanical behavior. These versatile nanoparticle-shelled bubbles are optimal candidates to form hierarchically assembled lightweight composites with targeted mechanical properties. In composites, the precise control over the structure and properties of the fillers allows the determination of the structure-property relationship, and enables a better understanding of the effect of the nanostructure on the macroscopic mechanical response.

## **Degree Type**

Dissertation

## **Degree Name**

Doctor of Philosophy (PhD)

## **Graduate Group**

Chemical and Biomolecular Engineering

## **First Advisor**

Daeyeon Lee

## **Keywords**

composites, lightweight, mechanical properties, microfluidics, nanoparticle-shelled bubbles, nanostructure

## **Subject Categories**

Chemical Engineering | Mechanical Engineering | Mechanics of Materials

NANOPARTICLE-SHELLED BUBBLES FOR LIGHTWEIGHT MATERIALS

Teresa Brugarolas Brufau

A DISSERTATION

in

Chemical and Biomolecular Engineering

Presented to the Faculties of the University of Pennsylvania

in

Partial Fulfillment of the Requirements for the

Degree of Doctor of Philosophy

2014

Supervisor of Dissertation

---

Daeyeon Lee, Associate Professor, Chemical and Biomolecular Engineering

Graduate Group Chairperson

---

Raymond Gorte, Professor, Chemical and Biomolecular Engineering

Dissertation Committee

John C. Crocker, Associate Professor, Chemical and Biomolecular Engineering

Daniel S. Gianola, Assistant Professor, Materials Science and Engineering and

Mechanical Engineering and Applied Mechanics

Shu Yang, Professor, Materials Science and Engineering

**NANOPARTICLE-SHELLED BUBBLES FOR LIGHWEIGHT MATERIALS**

COPYRIGHT

2014

Teresa Brugarolas Brufau

*A mi familia*

# Acknowledgments

I would like to thank in the first place my advisor, Prof. Daeyeon Lee, for his guidance and useful discussions throughout my research, and for helping me to make the most out of these five years.

I would also like to thank my thesis committee members Prof. Crocker, Prof. Yang and especially Prof. Gianola, for his suggestions, his teachings and his help with experiments. Also, I appreciate the collaboration and dedication of Prof. Feng and Prof. Bassani that made of this project a great learning experience.

I wish to thank *La Fundación Caja Madrid* and *Obra Social “La Caixa”* for their graduate fellowships that gave me the opportunity to spend several years learning and working with some of the brightest minds in the field.

Life in graduate school would not have been the same without my colleagues and friends. If I try to mention everyone this list would not end. I want to extend my gratitude to each member of the Lee Group, past and present, for their support, suggestions, teachings, encouragement and friendship, especially Kwadwo, Maj, Sang-Wook, Myung Han, Bum Jun, Lei, Diya, Iris, Fuquan, Jacob, Ankit, Yun-Ru, Elio, Sarah, Rohini, Gang, Jyo Lyn, WeiYang, Likai and all other members of the group that made my time at Penn really especial. I would like to express my gratitude to my friends in Philadelphia that throughout the years have been next to me, particularly Angélica, Milen, Vicky, Jiyeon,

Francesca, Monica, Kasey, Kaitlyn, Sandra, Ignacio, Christine, Nuria, Vinayak, and especially Alfredo. And my friends in Spain that inspire me and encourage me across the distance.

Finally, I would like to thank my parents, Antonio and Concepción, and my siblings, Jim, Paul, Claudia, M<sup>a</sup> Javier, Pedro, Miguel, Rita, and Juan, for their continuous advice, encouraging words, and constant support that has always accompanied me.

# ABSTRACT

## **NANOPARTICLE-SHELLED BUBBLES FOR LIGHTWEIGHT MATERIALS**

Teresa Brugarolas Brufau

Daeyeon Lee

Lightweight materials that are mechanically robust are of great interest in automotive, aerospace, and construction industries. However due to the nature of materials, it is challenging to obtain materials that have high strength, stiffness and toughness, and light weight simultaneously. One approach that tries to address this limitation is the use of composite materials containing hollow microparticles, also known as syntactic foams. The incorporation of hollow microparticles decreases the density of the material at the same time that increases its specific strength. Conventional methods of fabrication of hollow particles involving bulk reactions result in high heterogeneity in geometry as well as mechanical properties, and little or no control over the shell nanostructure. This variability in the structure and properties of the hollow microparticles adversely affects the macroscopic properties of the syntactic foams and hinders the understanding of the structure-property relationship. The use of microfluidics for the generation of shelled-bubbles addresses these limitations. This microfluidic technique, in contrast to bulk methods, is based on single droplet formation, allowing for the generation of highly



uniform bubbles, and enabling the assembly of nanoparticles at the interface forming stable nanoparticle-shelled bubbles. Microfluidics allow a precise control over the geometry, nanostructure and properties of the shelled-bubbles, further enabling the functionalization of the shell surface to present amphiphilicity, or the modification of the shell structure with thermal processes to enhance their mechanical behavior. These versatile nanoparticle-shelled bubbles are optimal candidates to form hierarchically assembled lightweight composites with targeted mechanical properties. In composites, the precise control over the structure and properties of the fillers allows the determination of the structure-property relationship, and enables a better understanding of the effect of the nanostructure on the macroscopic mechanical response.

# Table of Contents

<b>Acknowledgments</b> .....	<b>iv</b>
<b>ABSTRACT</b> .....	<b>vi</b>
<b>Table of Contents</b> .....	<b>viii</b>
<b>List of Tables</b> .....	<b>x</b>
<b>List of Figures</b> .....	<b>xi</b>
<b>Chapter 1. Introduction</b> .....	<b>1</b>
1.1 Background and Motivation .....	1
1.2 Thesis Objectives and Outline .....	8
<b>Chapter 2. Generation of Amphiphilic Janus Bubbles and Their Behavior at an Air-Water Interface</b> .....	<b>10</b>
2.1 Introduction.....	10
2.2 Experimental Section .....	11
2.3 Results and Discussion .....	14
2.4 Conclusions.....	30
<b>Chapter 3. Tailoring the Mechanical Properties of Nanoparticle-Shelled Bubbles</b> .	<b>31</b>
3.1 Introduction.....	31
3.2 Experimental Section .....	33
3.3 Results and Discussion .....	38
3.4 Conclusions.....	56
<b>Chapter 4. Understanding the Mechanical Properties of Nanoparticle-Shelled Bubbles</b> .....	<b>58</b>

4.1	Introduction.....	58
4.2	Experimental Section.....	59
4.3	Results and Discussion .....	64
4.4	Conclusions.....	80
<b>Chapter 5. Effect of Roughness and Porosity on the Mechanical Response of Shelled-Bubbles/Polymer Composites.....</b>		<b>82</b>
5.1	Introduction.....	82
5.2	Experimental Section.....	84
5.3	Results and Discussion .....	89
5.4	Conclusions.....	98
<b>Chapter 6. Conclusions and Outlook .....</b>		<b>101</b>
<b>Appendix 1. Finite Element Analysis Code .....</b>		<b>106</b>
A1.1	Axisymmetric FEA .....	106
A1.2	Three Dimensional FEA with Von Mises Material Model.....	114
A1.3	Three dimensional FEA with Drucker-Prager Material Model .....	120
<b>Appendix 2. Supplemental Results.....</b>		<b>125</b>
<b>Bibliography .....</b>		<b>132</b>

# List of Tables

<b>Table 3.1</b> Diameter and shell thickness of mechanically characterized shelled bubbles .	43
<b>Table 4.1</b> Properties of nanoparticle films .....	64
<b>Table 4.2</b> FEA parameters of simulated as-assembled, calcined and sintered bubbles ...	65

# List of Figures

<b>Figure 1.1</b> Ashby plots: (a) stiffness, (b) strength, and (c) fracture toughness vs density. Reproduced from Ref. 3 with permission from the Royal Society Publishing.....	2
<b>Figure 1.2</b> Microfluidic generation of gas-in-oil-in-water (G/O/W) compound bubbles. (a) Diagram of the microfluidic device used for the fabrication of compound bubbles; (b) Optical micrograph of the generation of monodisperse G/O/W compound bubbles; (c) Schematic diagram of the shell formation when oil evaporates from the middle layer of the G/O/W compound bubble resulting in a nanoparticle-shelled bubble; and (d) Composition of the phases involved in the microfluidic generation of nanoparticle-shelled bubbles.....	5
<b>Figure 1.3</b> Diagram of hierarchically arranged nanoparticles in multiple levels. Particles forming the shell of a bubble/emulsion, and nanoparticle-shelled bubbles/emulsions forming a three dimensional macrostructure. ....	7
<b>Figure 2.1.</b> Schematic illustrations of (a) Janus bubble formation via metal deposition and (b) the generation of air-in-oil-in-water (A/O/W) compound bubbles using a microfluidic device. These A/O/W compounds are used as templates to form nanoparticle-shelled bubbles.....	15
<b>Figure 2.2</b> High-magnification SEM image of a bubble shell showing nanoparticles (scale bar = 500 $\mu\text{m}$ ). Inset represents a higher magnification image (scale bar = 200 nm) .....	16
<b>Figure 2.3</b> (a) Optical microscopy images and size distribution of nanoparticle-shelled bubbles before drying and after re-suspending in water; and (b) SEM image of dried nanoparticle shelled bubbles on a glass substrate (scale bar = 50 $\mu\text{m}$ ).....	17
<b>Figure 2.4</b> Stability state diagram showing the percentage of nanoparticle-shelled bubbles that remain intact after drying. The stability of bubbles strongly depends on the dimension of the bubbles: the thickness of the bubble shell ( $z$ ) and bubble diameter ( $d$ ). The dashed line that goes through the origin indicates the critical ratio of shell thickness to bubble diameter $(z/d)_c$ and has a slope of $0.042 \pm 0.007$ . ....	18
<b>Figure 2.5</b> Optical microscopy image of a monolayer of dried bubbles significantly damaged during drying. Scale bar = 200 $\mu\text{m}$ .....	19
<b>Figure 2.6</b> SEM image of a monolayer of Janus bubbles after metal deposition with a gold layer on one hemisphere. Inset shows a high magnification image of a Janus bubble. Diffuse Janus boundary can clearly be seen close to the equator of the bubble. Scale bars = 50 $\mu\text{m}$ . ....	20

**Figure 2.7** (a) Schematic illustration of the assembly of bubbles at a convex air-water interface. Optical microscopy images of assemblies of (b) un-modified SiO<sub>2</sub> nanoparticle-shelled bubbles and (c) amphiphilic Janus bubbles at the top of a convex air-water interface..... 21

**Figure 2.8** (a) Center-to-center distance ( $R$ ) between two Janus bubbles as a function of time ( $t$ ) (bubble size  $d = 54.0 \mu\text{m}$ ). Inset figure shows the logarithmic plot  $R$  vs.  $(t-t_{max})$  where  $t_{max}$  is the time when the bubbles make contact. (b) Velocity of bubble approach as a function of interbubble distance ( $R$ ) converted from (a). Inset represents the attractive potential determined using Equation 2.2. .... 25

**Figure 2.9** Attractive interaction potential ( $-U(R)/k_B T$ ) between pairs of Janus bubbles of three different sizes as a function of interbubble distance ( $R$ )..... 26

**Figure 2.10** SEM images of (a) Janus bubbles and (b) un-modified SiO<sub>2</sub> nanoparticle-shelled bubbles embedded in PDMS slabs showing the difference in the position of bubbles with respect to the air-water interface, and (c) Janus bubbles attached to a double-sided tape showing their orientation at the air-water interface. Profilometry contour plots showing the shape of the interface around (d) Janus bubbles and (e) unmodified nanoparticle-shelled bubbles. White arrow and red arrow indicate positive and negative deformation of the air-water interface, respectively. Scale bars = 50  $\mu\text{m}$ . .. 28

**Figure 3.1** Permeability of calcined bubbles. A sample of calcined bubbles is wetted by DI water and the behavior is captured with an optical microscope for approximately 20 minutes. Water slowly permeates the porous shell and fills the shelled bubble with water. From (a) to (f) calcined bubbles at different times during the permeation of the water into the shell. Scale bar 200  $\mu\text{m}$ . .... 35

**Figure 3.2** Schematic illustration of nanoparticle-shelled bubble formation from a gas-in-oil-in-water (G/O/W) compound bubble generated with a microfluidic technique. The removal of the toluene forming the oil layer, drives jamming and compaction of the suspended silica nanoparticles, which forms a solid shell around the inner gas phase. ... 39

**Figure 3.3** Thermogravimetric analysis of as-assembled nanoparticle-shelled bubbles indicating a complete removal of organic components around 650°C. .... 40

**Figure 3.4** (a) Schematic representation of physical modification of nanoparticle-shelled bubbles with thermal treatment, (b) optical micrographs (inset: SEM micrographs) of nanoparticle-shelled bubbles on a substrate after heat treatment.  $d$  and  $p$  represent the outer diameter of the bubbles and the porosity of the bubble shells, respectively. Inset scale bars = 10  $\mu\text{m}$ . .... 41

**Figure 3.5** Determination of failure for calcined bubbles from nanoindentation results. 43

**Figure 3.6** (a) Schematic illustration of nanoindentation on a single bubble with a spherical indenter. Load-displacement results from *ex situ* nanoindentation tests performed

on (b) seven as-assembled bubbles, (c) five calcined bubbles, and (d) nine sintered bubbles. .... 45

**Figure 3.7** Superimposed SEM images of (a) as-assembled and (b) calcined bubbles before and after load-unload test. (c) Load-displacement curves of the two bubbles after load-unload cycles. Displacement for each bubble is kept low to ensure that no fracture is observed. .... 48

**Figure 3.8** Fracture mechanism of a characteristic as-assembled bubble (left) and calcined bubble (right) from quantitative *in situ* compression testing with flat punch; (a) to (h) different frames along the experiment. Scale bars 20  $\mu\text{m}$ . Inset graphs indicate the load-displacement at the specific time. Red arrows point at originated cracks. .... 50

**Figure 3.9** Load-displacement curves of in-situ experiments. Curves corresponding to (a) four as-assembled bubbles, and (b) four calcined bubbles. .... 52

**Figure 3.10** (a) Diameter,  $d$ , and shell thickness,  $t$ , of as-assembled, calcined and sintered bubbles. (b) Average failure load of bubbles at fracture,  $P_f$ , as measured by the maximum load registered before the first crack. (c) Average stiffness of bubbles,  $\Delta P/\Delta\delta$ , computed from the slope of the load-displacement curves in the elastic regions. For as-assembled bubbles the elastic region is consider at small deflections of  $\delta < 500$  nm. (d) Average maximum deflection of bubbles,  $\delta_f/d$ , measured just before fracture, normalized by the initial diameter of the bubble. (e) Average energy to failure,  $U_f$ , computed from the area under the load-displacement curves before the first fracture. .... 54

**Figure 3.11** (a) Layer-by-Layer (LbL) method used for the generation of polymer-bubble composites. (b) LbL structure composed of 10 bilayers for a total thickness of approximately 1 mm. (c) LbL structure made of as-assembled bubbles and polystyrene, and (d) LbL structure made of sintered bubbles and polystyrene. Scale bars = 200  $\mu\text{m}$ . 56

**Figure 4.1** Film thickness growth with number of deposition of particles by spin coating with subsequent calcinations steps between each deposition. The growth rate is 145nm per deposition. Values in graph are averaged from eight samples, and error bars correspond to standard deviation. .... 63

**Figure 4.2** Load-displacement simulation results of sintered bubbles. (a) Different outer diameters with constant  $t=2.6\mu\text{m}$  and  $E=76\text{GPa}$ , (b), (b) different Young's moduli with constant  $d=34.6\mu\text{m}$  and  $t=2.6\mu\text{m}$ , and (c) different thicknesses with constant  $d=34.6\mu\text{m}$  and  $E=76\text{GPa}$ . The deviation of each parameter represents the standard deviation measured experimentally. .... 68

**Figure 4.3** (a), (b) and (c) are load-displacement curves simulated using FEA for as-assembled, calcined and sintered bubbles, respectively, with comparisons to the experimental results (shaded regions). (d) Contour plots from FEA showing first principal stress of a sintered bubble under a spherical indenter at an indentation depth, in each case, corresponding to the average of the first fracture observed in the experimental

nanoindentation *ex situ* tests. Figures i, ii, and iii, represent different shell geometries (uniform, thin at bottom, and thin at top) indicating the differences in the first principal stress distribution along the shell at the maximum indentation depth predicted from the FEA. .... 70

**Figure 4.4** Load-displacement curves of *in situ* compression of (a) four as-assembled bubbles, and (b) four calcined bubbles, including both the first failure event as well as the secondary cracking events that occur on loaded remnants of the fracture shells. FEA results for the first failure event are included in the graphs for three different shell geometries (uniform shell, thin at top, and thin at bottom). FEA results for secondary cracks for uniform shells are also plotted including the responses when one or two halves of the shell remain under load between the indenter and the substrate. (c) Simulation results for the failure prediction of a sintered bubble lacking of experimental values. As-assembled bubbles (a) are simulated with elastic perfectly plastic von Mises (VM) and Drucker-Prager (DP) models. Calcined bubbles (b), and sintered (c) are simulated with an elastic model. .... 73

**Figure 4.5** Three dimensional FEA of calcined half shell modeled as a perfect elastic material. The maximum first principal stress is concentrated beneath the indenter presumably causing the secondary vertical cracks. The magnitude of the maximum principal stress at failure deflection (0.574 GPa) is consistent with the stress observed during first crack (0.617GPa) from the two dimensional FEA..... 75

**Figure 4.6** Von Mises stress in the inner and outer surfaces of a hemispherical as-assembled bubble shell. The hemispherical as-assembled shell is modeled using a von Mises material model (a), and a Drucker-Prager material model (b). .... 76

**Figure 4.7** Mean stress in the inner and outer surfaces of a hemispherical as-assembled bubble shell. The hemispherical as-assembled shell is modeled using (a) the von Mises material model and (b) the Drucker-Prager material model. .... 77

**Figure 4.8** Finite element simulation of half as-assembled bubble modeled as a von Mises material (a), and a Drucker-Prager material (b). In each case, the appropriate effective plastic strain is plotted over the inner and outer surfaces. Note the elevation of plastic strain near the mid-meridian plane for the Drucker-Prager material. .... 80

**Figure 5.1** (a) Laser cut mold in acrylic sheet, 1/8” thick, for composite sample preparation (scale bar 2 mm), (b) density of samples, (d) typical stress-strain curve obtained from compression testing of composite, insets correspond to samples before and after testing (height of samples ~1.8 mm). NT refers to non-treated surface. APS/BSA refers to the coupling agents used to treat the surface. .... 91

**Figure 5.2** Mechanical response of composites using sintered bubbles with different surface treatments: non-treated (NT), MPS, APS, and a combination of APS and BSA.



(a) Specific stiffness, (b) specific compressive strength, (c) peak strain, and (d) specific toughness..... 93

**Figure 5.3** Bar charts representing the mechanical properties of composites extracted from the compression testing to failure. (a) specific stiffness, (b) specific compressive strength, (c) peak strain, and (d) specific toughness. .... 96

**Figure 5.4** SEM images of bubbles in composites after mechanical testing: (a) Surface of a calcined bubble showing roughness, inset is a cross-section of a calcined shell in which individual particles can be observed; (b) Fracture surface of calcined APS/BSA 30% composite; (c) Surface of a sintered bubble with a smooth surface; and (d) Fracture surface of sintered NT 30% composite..... 98

**Figure 6.1** SEM image of a platelet bubble ..... 104

**Figure A2.1** (a) Bubble density approximated from the measured tapped density of dried bubbles and assuming a random close packing. (b) Young's modulus and porosity of nanoparticle films subjected to the same thermal treatments than the bubbles.....126

**Figure A2.2** (a) Density, (b) specific stiffness, and (c) specific compressive strength of composite samples made with as-assembled, 700, 850, 1000 and 1150 °C bubbles at 20 and 30 weight fraction of bubbles.....128

**Figure A2.3** (a) Strain at peak and (b) specific toughness of composite samples containing as-assembled, 700, 850, 1000 and 1150 °C bubbles at 20 and 30 weight fraction of bubbles.....130

# Chapter 1. Introduction

## 1.1 Background and Motivation

Lightweight materials that are mechanically robust have always been of great interest in engineering. They are especially pursued in applications such as automotive and aerospace,<sup>1</sup> in which lightweight materials will enhance the energy efficiency and contribute to reduce the emissions, and in construction industries,<sup>2</sup> in which specialized civil engineering applications may require light weight and high strength and toughness.

The mechanical properties of materials depend on the nature of the material, the size of the atoms and the forces that bind them together, and as a result the strength, the stiffness, and even the fracture toughness of materials are directly correlated with their density, as can be seen in the Ashby plots of Figure 1.1.<sup>3</sup>

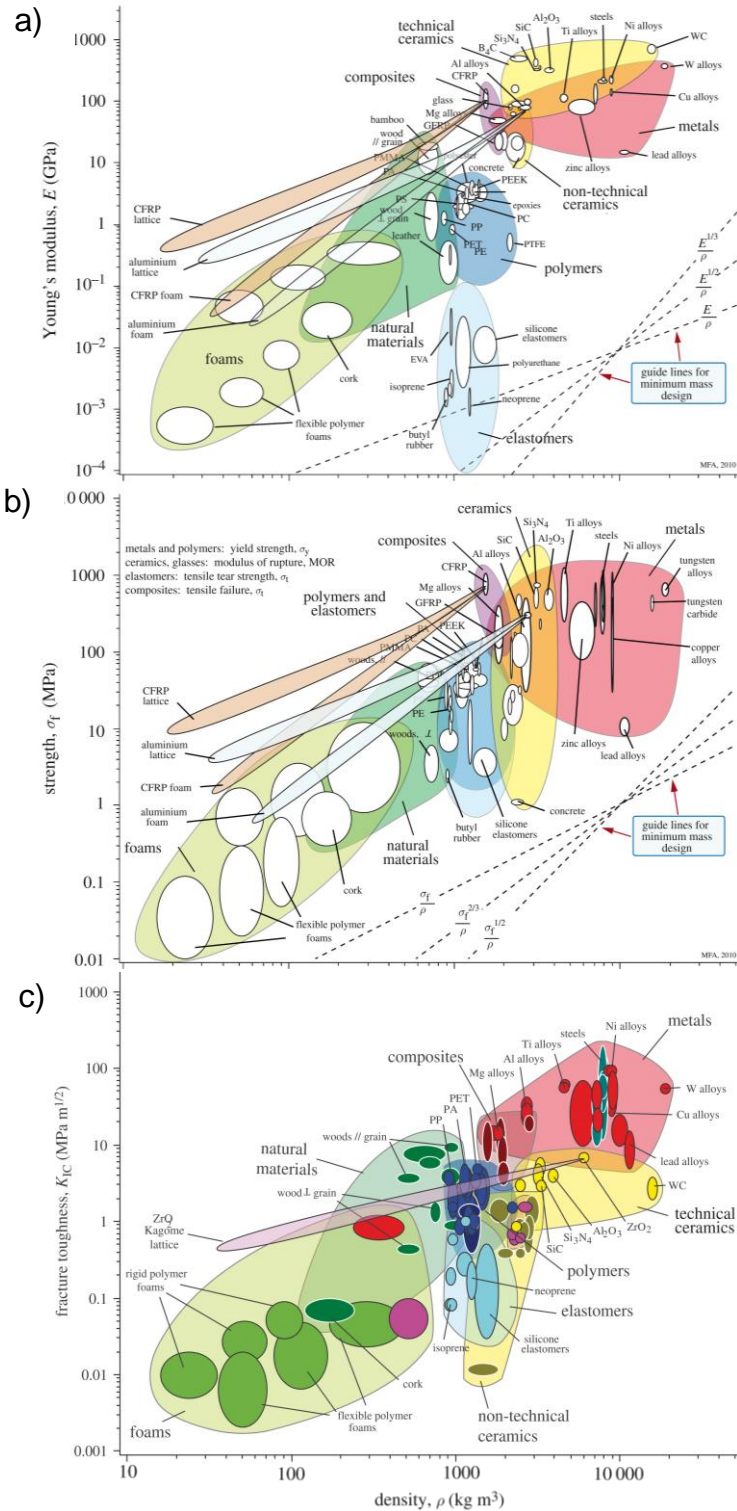


**Figure 1.1** Ashby plots: (a) stiffness, (b) strength, and (c) fracture toughness vs density. Reproduced from Ref. 3 with permission from the Royal Society Publishing.

These material property charts show the stiffness, the strength and the fracture toughness versus the density of common materials. It is interesting to note that all three mechanical properties correlate positively with the density, implying that high stiffness, strength and fracture toughness may only be achieved by high density materials. Therefore, the generation of lightweight materials with high mechanical properties is very challenging.

One of the approaches that tries to address this limitation is the fabrication of syntactic foams, which are composites made of hollow microparticles, usually glass, randomly distributed in a polymeric matrix, forming a closed-cell foam structure.<sup>4</sup> The presence of the hollow microparticles decreases the density of the final composite at the same time that increases its specific strength.<sup>5</sup> The mechanical properties of the constituents will determine the mechanical properties of the syntactic foam. In general, the compressive properties of the syntactic foams depend primarily on the properties of the hollow microparticles properties, whereas the tensile properties depend on the matrix material used.<sup>5</sup> However, the relation between components and macroscopic properties of the composite is not that simple. Conventional methods of fabrication of glass hollow microparticles involve the addition of a grained solid and a blowing agent into a bubble promoting medium leading to gelled microbubbles which after firing result in ceramic hollow microparticles.<sup>6</sup> These bulk methods have no control over the shell structure and result in hollow spheres with large heterogeneity in size and shell thickness,<sup>6</sup> which unfortunately leads to a broad range of mechanical properties. This lack of control over the structure and properties of the hollow microparticles jeopardizes the macroscopic

response of the composite and hinders the ability to predict the structure-property relationship when incorporated in syntactic foams.

Furthermore, the interface between filler (hollow microparticles) and matrix in the syntactic foams plays a critical role on the ultimate mechanical properties.<sup>5, 7</sup> A weak interface between hollow microparticles and matrix will cause debonding during loading inducing an early failure. The control over the strength of the interface between filler and matrix in syntactic foams remains still a challenge. In some cases, the hollow microparticles are coated or chemically functionalized with different surface treatments to improve adhesion,<sup>8</sup> or the composite is reinforced with fibers to improve their toughness,<sup>9</sup> however these efforts have shown slight improvement or in some cases a negative effect on the interfacial strength. The lack of control over the structure and properties of the hollow microparticles contributes to the difficulty of improving the quality of the interface between fillers and matrix.

One method that overcomes many of these challenges consists of using microfluidics to generate the bubbles, or hollow microparticles. Microfluidics are based on continuous single droplet formation, in contrast to bulk methods, allowing for the generation of highly uniform and complex emulsions and bubbles.<sup>10</sup> The mechanism of formation relies on the intricate balance between surface tension and viscous forces. The geometry of monodisperse emulsion droplets and gas bubbles depends strongly on the dimension of the microfluidic channels, the flow rates and the solution properties (e.g., surface tension, viscosity and density) of the fluids.<sup>11</sup>

Different microfluidic devices and geometries have been proposed for the generation of bubbles, and one example is shown in the diagram and the optical micrograph of Figure 1.2a and b, in which a glass microfluidic device assists the formation of gas-in-oil-in-water compound bubbles from three initial immiscible fluid phases detailed in Figure 1.2d. This versatile microfluidic device permits the incorporation of dissolved polymers or suspended particles in the different fluid phases to generate polymer- or nanoparticle-shelled bubbles.<sup>12-14</sup> The use of a colloidal suspension of silica nanoparticles in toluene as middle phase leads to the formation of a shell of jammed nanoparticles when the toluene in the middle layer evaporates (Figure 1.2c).

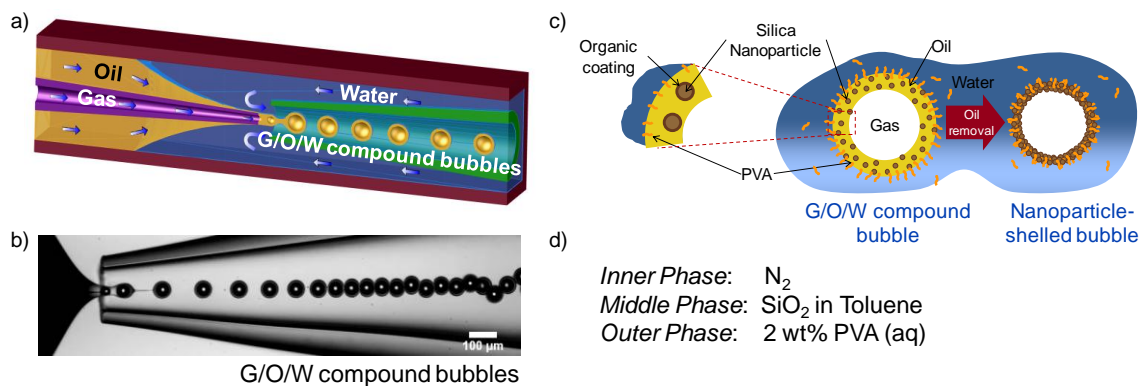


**Figure 1.2** Microfluidic generation of gas-in-oil-in-water (G/O/W) compound bubbles. (a) Diagram of the microfluidic device used for the fabrication of compound bubbles; (b) Optical micrograph of the generation of monodisperse G/O/W compound bubbles; (c) Schematic diagram of the shell formation when oil evaporates from the middle layer of the G/O/W compound bubble resulting in a nanoparticle-shelled bubble; and (d) Composition of the phases involved in the microfluidic generation of nanoparticle-shelled bubbles.

This microfluidic technique allows not only the generation of monodisperse bubbles but also enables a precise control over the geometry, size and thickness, of the final shelled bubble by controlling the flow rates of the middle and outer phases and the

pressure of the inner phase. It has been shown that the generated nanoparticle-shelled bubbles using this method are very stable against dissolution and coalescing because of the formation of the close-packed layers of nanoparticles at the air-water interface.<sup>12</sup> The ability of generating stable bubbles with precise control over the geometry and the shell structure and properties opens up a myriad of opportunities. Microfluidic nanoparticle-shelled bubbles can be dried and resuspended without compromising their stability, what allows the functionalization of the shell surface, and tailoring of the shell structure and properties using thermal treatments.

More importantly, this microfluidic technique presents new possibilities to generate macroscopic three-dimensional hierarchical structures from nanoscale materials by further assembling the particle-covered bubbles as illustrated in Figure 1.3. These hierarchical assemblies have great potential for the generation of porous structures, including syntactic foams, to design lightweight materials with targeted mechanical properties for structural applications.<sup>15</sup> Using microfluidic bubbles as structure directing agents provides an exquisite control over the nanostructure, geometry and properties of these hierarchical assemblies. The incorporation of these nanoparticle-shelled bubbles in composites forming syntactic foams allows a better study of the structure-property relationship and additionally provides new means to assess the structural factors and optimize their effect on the interfacial strength between fillers and matrix. Since these bubbles can be functionalized and structurally modified, it is possible to generate higher order structures with tailored properties.

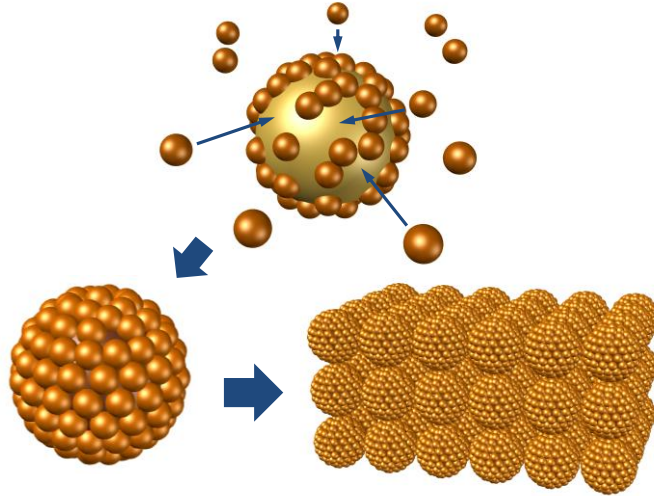


**Figure 1.3** Diagram of hierarchically arranged nanoparticles in multiple levels. Particles forming the shell of a bubble/emulsion, and nanoparticle-shelled bubbles/emulsions forming a three dimensional macrostructure.

In summary, the motivation of this thesis is to generate hierarchical lightweight materials with desired mechanical properties. Assembling nanoparticles using microfluidic bubbles as templates gives precise control on the final shell geometry, the nanostructure and the mechanical properties, and allows for further tailoring using thermal treatment or surface modification. An in depth study of the structure-property relationship of nanoparticle-shelled bubbles complements the generation of these versatile assemblies demonstrating their applicability, feasibility and potential uses. Furthermore, this thesis aims to address the challenge of generating hierarchical lightweight composites using tailored nanoparticle-shelled bubbles, investigating the effect of the nanostructure on the macroscopic properties of the ultimate material.



## **1.2 Thesis Objectives and Outline**

### **1.2.1 Objectives**

The main purpose of this thesis is to generate advanced functional macrostructures that are lightweight and possess high stiffness, strength and toughness. This thesis investigates the assembly of nanoparticles on microfluidic bubbles and the ability to tailor their structure and properties with thermal treatments and surface modification. Another challenge that is addressed is the determination of the structure-property relationship on the as-assembled and thermally treated nanoparticle-shelled bubbles. In addition, this thesis explores the assembly of these microfluidic nanoparticle-shelled bubbles in composites investigating the effect of the nanostructure on the macroscopic properties of the composite.

### **1.2.2 Thesis Outline**

*Chapter 2* addresses the objective of exploring the potential of silica nanoparticle-shelled bubbles generated with microfluidics, which can be dried and re-suspended without compromising their stability or undergoing structural changes. In addition, this chapter describes the possibility of partially modifying the surface of these nanoparticle-shelled bubbles resulting in amphiphilic Janus bubbles, and observing their behavior at an air-water interface.

*Chapter 3* addresses the goal of exploring the ability to tailor the structure and mechanical behavior with thermal processes of nanoparticle-shelled bubbles. The mechanical response of these as-assembled and thermally modified nanoparticle-shelled bubbles is characterized in detail contributing to understand the structure-property relationship. These silica nanoparticle-shelled bubbles, as-assembled and thermally modified, are presented as building blocks for three dimensional structures.

*Chapter 4* complements the experimental results of *Chapter 3* by describing the mechanical behavior of the as-assembled and thermally modified silica nanoparticle-shelled bubbles with finite element analysis (FEA). The simulation work of this chapter augments the understanding of the mechanical response observed experimentally.

*Chapter 5* addresses the goal of using thermally modified silica nanoparticle-shelled bubbles generated using microfluidics as building blocks in hierarchical lightweight composites, and investigates the effect of the nanostructure of these bubbles to further enhance the interfacial strength between fillers and matrix, and the overall mechanical response of the composite.

*Chapter 6* summarizes the findings of this thesis and includes some suggestions for future directions.

# Chapter 2. Generation of Amphiphilic Janus Bubbles and Their Behavior at an Air-Water Interface

Reprinted (adapted) with permission from T. Brugarolas, B. J. Park, M. H. Lee, D. Lee. Generation of Amphiphilic Janus Bubbles and Their Behavior at an Air-Water Interface. *Advanced Functional Materials*, 2011, 21, 3924-3931. Copyright (2011) WILEY-VCH Verlag GmbH & Co. KGaA, Weinheim.

## 2.1 Introduction

Despite recent progress in the generation of engineered bubbles<sup>13, 16-20</sup> and their applications,<sup>21-26</sup> most studies to date have focused on the synthesis and utilization of homogeneously modified bubbles. It is interesting to note that recent advances involving solid particles have shown that asymmetric functionalization of the particle surface leads to novel phenomena that are of fundamental and practical importance. It has been shown, for example, that the assembly of Janus particles – solid particles with polar and apolar hemispheres – leads to the formation of novel colloidal aggregate structures.<sup>27-36</sup> In addition, electrically or magnetically switchable systems based on Janus and patchy particles have been reported for applications in optical devices,<sup>28</sup> self-propulsion<sup>37</sup> and emulsion stabilization.<sup>38-39</sup> This recent progress based on Janus and patchy particles suggest that asymmetric functionalization of gas bubbles could potentially lead to unique opportunities. For instance, the formation of bubble rafts consisting of asymmetric bubbles could result in major advances in the understanding of atomic solids with anisotropic interactions. Bubbles with directional interactions could also enable the

formation of novel three-dimensional structures that could be useful for acoustic metamaterial applications.<sup>40</sup>

In this work, we present the generation of amphiphilic Janus bubbles and study their interfacial behavior at an air-water interface. Analogous to Janus particles, Janus bubbles are asymmetric bubbles with two hemispheres that have different wetting, optical, electrical, or magnetic properties.<sup>20</sup> Owing to their buoyancy, Janus bubbles provide a unique opportunity to study the behavior of Janus spheres at an air-water interface. It is interesting to note that P. G. de Gennes remarked in his Nobel Lecture that an assembly of Janus particles at an air-water interface would form a porous membrane, which could have important fundamental and practical implications.<sup>41</sup> By enabling the synthesis of Janus bubbles using ultra-stable nanoparticle-shelled bubbles, we show that Janus bubbles exhibit a unique assembly behavior at an air-water interface. We investigate the nature of interactions between Janus bubbles at the interface and find that lateral capillary interactions between bubbles are responsible for their assembly behavior.

## **2.2 Experimental Section**

### **2.2.1 Preparation of Nanoparticle-Shelled Bubbles**

The generation of nanoparticle shelled bubbles is performed following a previously reported method<sup>12</sup>. Briefly, air-in-oil-in-water (A/O/W) compound bubbles are formed using a microfluidic device, using nitrogen (N<sub>2</sub>) as the inner phase, a suspension of

hydrophobic SiO<sub>2</sub> particles in toluene as the middle phase (Nissan Chemical Industries, Ltd. average diameter = ~ 15 nm), and an aqueous solution of poly(vinyl alcohol) (PVA, 87-89% hydrolyzed, average Mw = 13 000 - 23 000, purchased from Sigma-Aldrich) as the outer phase. A/O/W compound bubbles are collected in a petri dish (35x10mm) filled with water forming a convex meniscus; this procedure prevents bubbles from forming multiple layers near the wall of the vessel. After complete solvent evaporation, the water in the petri dish is changed three times to remove excess PVA from the bubble surface. A thin layer of PVA remains attached to the surface of the nanoparticle-shelled bubbles rendering the bubble surface hydrophilic. A drop of bubble suspension is placed on a glass slide and air dried to form a monolayer of SiO<sub>2</sub> nanoparticle-shelled bubbles on the surface.

### **2.2.2 Generation of Amphiphilic Janus Bubbles**

A thermal evaporator (Thermonics Laboratory Inc., VE-90) is used for the selective coating of an adhesive layer of chromium (~ 3 nm) and a subsequent layer of gold (~ 30 nm) onto the dried monolayer of SiO<sub>2</sub> nanoparticle-shelled bubbles. To impart amphiphilicity to Janus bubbles, the gold hemisphere is modified with 1-octadecanethiol (ODT, Sigma-Aldrich) by immersing the Janus bubble attached to a glass slide into a 1 mM solution of ODT in toluene for 15 min. Janus bubbles from the glass slide are recovered by re-suspending them in a petri dish filled with water. The glass slide is immersed into water at an angle of 90-100° with respect to the air-water surface.

### 2.2.3 Bubble Characterization

An upright microscope (Carl Zeiss Axio Plan II) equipped with a CCD camera (Qimaging Retiga 2000R Fast 1394) is used to obtain optical microscope images to analyze the average bubble size, size distribution and stability of bubbles. Image J software is used for image analysis. The thickness of the bubble shell is determined by performing a mass balance on the middle and inner fluid phases of A/O/W compound bubbles. The packing density of SiO<sub>2</sub> nanoparticles in the shell after solvent removal is assumed to be 0.64 (*i.e.*, packing density for randomly packed spheres). The percentage of stable bubbles after drying is determined by the visual identification and enumeration of damaged bubbles from optical microscope images of dried bubbles. An average of 300 bubbles was analyzed for each data point in the stability diagram (Figure 2.4). The percentage of bubbles that are recovered after re-suspension is determined using a similar procedure by visually enumerating recovered bubbles. Particle tracking movies are recorded using an inverted microscope (Nikon Diaphot 300) with a high-speed camera (Phantom V7.1). Scanning electron microscopy (SEM) images are taken using a FEI Quanta 600 FEG ESEM at 2.00-5.00 kV. The gel trapping technique is carried out using 1 wt% Phytigel in water at a temperature of 45-50 °C. Previous studies have shown that the surface tension of water is not significantly influenced in the presence of the gel<sup>42-44</sup>. A dilute suspension of Janus bubbles is then placed on top of a gel precursor (1 wt% Phytigel in water). Subsequently, the aqueous phase is allowed to undergo gelation at room temperature, which traps the bubbles at the interface. Subsequently the precursor of

polydimethylsiloxane (PDMS, Sylgard<sup>®</sup> 184 silicone elastomer kit, Dow Corning) is placed on top of the gelled aqueous phase. Bubbles are transferred to solidified PDMS after curing the precursor at room temperature for 48 hr. Double-sided carbon tape is used to perform a second transfer in order to visualize the equilibrium position of the bubbles at the air-water interface. Contour plots of the interfacial profile around bubbles trapped at the air-gel interface are obtained using a Zygo NewView 6K series optical profilometer.

## **2.3 Results and Discussion**

### **2.3.1 Generation of Amphiphilic Janus Bubbles**

Selective deposition of a metal on one hemisphere of bubbles is used for the generation of Janus bubbles. This method consists of the sequential deposition of chromium and gold onto a monolayer of dried bubbles on a planar substrate as schematically illustrated in Figure 2.1a. The gold hemisphere can subsequently be modified with a self-assembled monolayer (SAM) of an alkane thiol to modify its wettability.<sup>45-48</sup> Although this process has been used for the generation of solid Janus particles,<sup>49</sup> it is challenging to apply this method to fabricate Janus bubbles because typical bubbles cannot be dried onto a surface without significant changes to their properties and structure. Thus, it is critical to use bubbles that can withstand drastic changes such as drying.

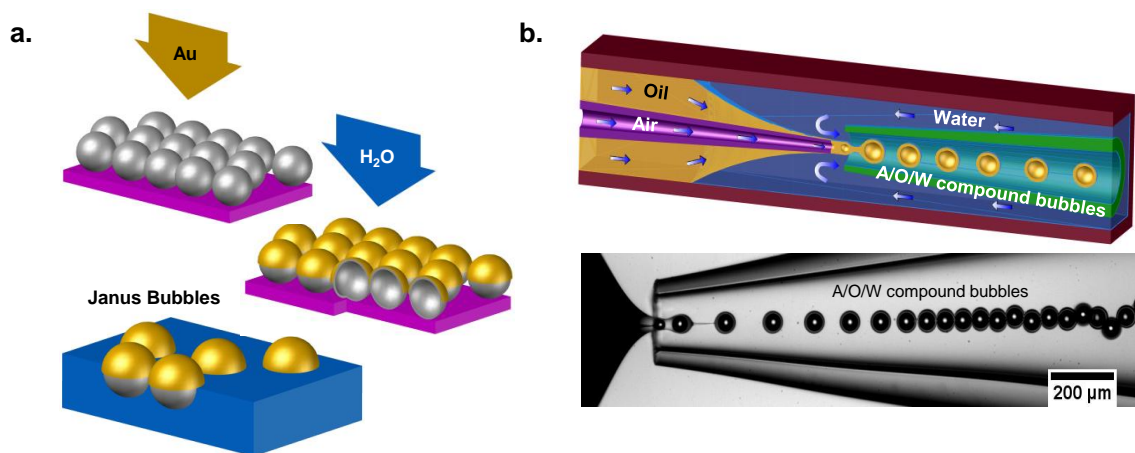


**Figure 2.1.** Schematic illustrations of (a) Janus bubble formation via metal deposition and (b) the generation of air-in-oil-in-water (A/O/W) compound bubbles using a microfluidic device. These A/O/W compounds are used as templates to form nanoparticle-shelled bubbles.

To enable the generation of Janus bubbles using the selective deposition of gold, we prepare ultra-stable bubbles using a microfluidic method. We recently developed a method to generate highly stable monodisperse bubbles by using air-in-oil-in-water (A/O/W) compound bubbles as templates.<sup>12</sup> A glass microfluidic device that allows for the control of flow of three immiscible fluids (gas, oil and water) is used to generate a monodisperse A/O/W compound bubble. The three fluid phases typically consist of nitrogen as the inner phase, a suspension of hydrophobic SiO<sub>2</sub> particles in toluene as the middle phase (~ 28 wt%), and a 2 wt% poly(vinyl alcohol) (PVA) aqueous solution as the outer phase. The outer stream funnels the inner and middle streams into the collection tube and breaks them into monodisperse A/O/W compound bubbles as shown in Figure 2.1. PVA adsorbs at the oil-water interface and stabilizes the A/O/W compound bubble against coalescence.<sup>12</sup> Monodisperse nanoparticle-shelled bubbles are subsequently



generated by removing toluene from the middle phase of the compound bubbles via evaporation. Figure 2.2 shows a high magnification SEM image of a nanoparticle shell.

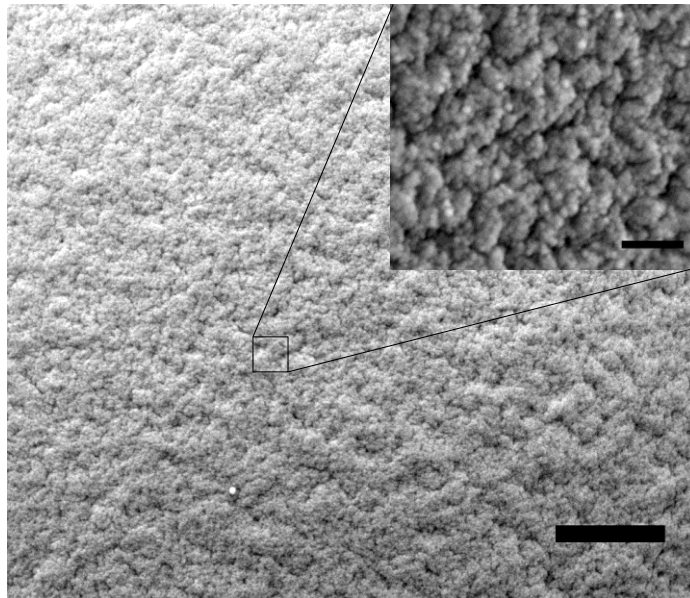


**Figure 2.2** High-magnification SEM image of a bubble shell showing nanoparticles (scale bar = 500  $\mu\text{m}$ ). Inset represents a higher magnification image (scale bar = 200 nm)

Nanoparticle-shelled bubbles, generated using the microfluidic method, are remarkably stable. These bubbles can be dried and re-suspended with negligible change in their size and shape. As can be seen in Figure 2.3, the size distribution of the bubbles before drying (average diameter  $d_1 = 54.8 \mu\text{m}$ , standard deviation  $\sigma_1 = \pm 1.2 \mu\text{m}$ , polydispersity  $\delta_1 = 2.25\%$ ) and after re-suspending ( $d_2 = 55.4 \mu\text{m}$ ,  $\sigma_2 = \pm 1.2 \mu\text{m}$ ,  $\delta_2 = 2.27\%$ ) do not show any significant difference, clearly indicating that the stiff nanoparticle shell prevents significant changes in the structure and size of the bubbles during drying and re-suspending. Direct observation of dried bubbles on a surface using

scanning electron microscopy (SEM) also confirms that dried nanoparticle-shelled bubbles remain spherical as shown in Figure 2.3.

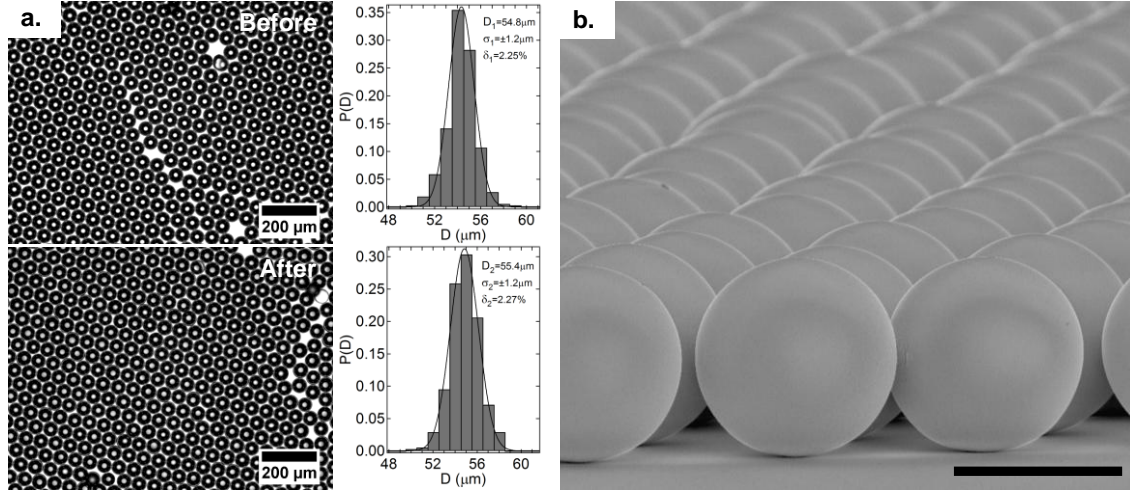


**Figure 2.3** (a) Optical microscopy images and size distribution of nanoparticle-shelled bubbles before drying and after re-suspending in water; and (b) SEM image of dried nanoparticle shelled bubbles on a glass substrate (scale bar = 50 μm).

The stability of nanoparticle-shelled bubbles against irreversible deformation during drying strongly depends on the dimension of bubbles, which can be precisely controlled by changing the flow rates of the three fluid phases in the microfluidic device. Figure 2.4 shows the dependence of the stability of nanoparticle-shelled bubbles on their dimensions. The stability of nanoparticle-shelled bubbles during drying depends on the ratio of the thickness of bubble shell ( $z$ ) to the size of bubble ( $d$ ). As the ratio of shell thickness to bubble diameter ( $z/d$ ) increases the stability of bubbles against destruction during drying also increases. The critical ratio of shell thickness to bubble diameter,  $(z/d)_c$ , is determined to be  $0.042 \pm 0.007$ .

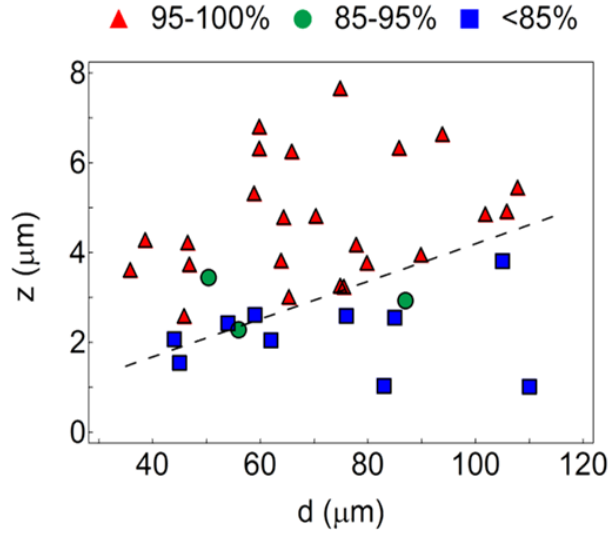


**Figure 2.4** Stability state diagram showing the percentage of nanoparticle-shelled bubbles that remain intact after drying. The stability of bubbles strongly depends on the dimension of the bubbles: the thickness of the bubble shell ( $z$ ) and bubble diameter ( $d$ ). The dashed line that goes through the origin indicates the critical ratio of shell thickness to bubble diameter  $(z/d)_c$  and has a slope of  $0.042 \pm 0.007$ .

Although the physical mechanism for the destruction of bubbles is quite different, a recent study also showed that the ratio of shell thickness to bubble diameter is a critical parameter in the formation of wrinkle-free polymer-shelled bubbles from A/O/W compound bubbles.<sup>13</sup> Debris from damaged bubbles is highly undesirable because they become impurities and imperfections during gold deposition and the subsequent re-dispersion of Janus bubbles (Figure 2.5 shows a microscope image of bubbles that have been significantly damaged during drying). Thus, we control the dimension of A/O/W compound bubbles to obtain nanoparticle-shelled bubbles in the stable regime of the state diagram in Figure 2.4 (i.e.,  $z/d > 0.042 \pm 0.007$ ). Approximately 95 % of dried nanoparticle-shelled bubbles in the stable regime can be recovered in the re-suspension step. While it is not the focus of this work, the mechanical instability of spherical shells

upon drying from a liquid suspension has not been studied in detail, and our work provides important insights.

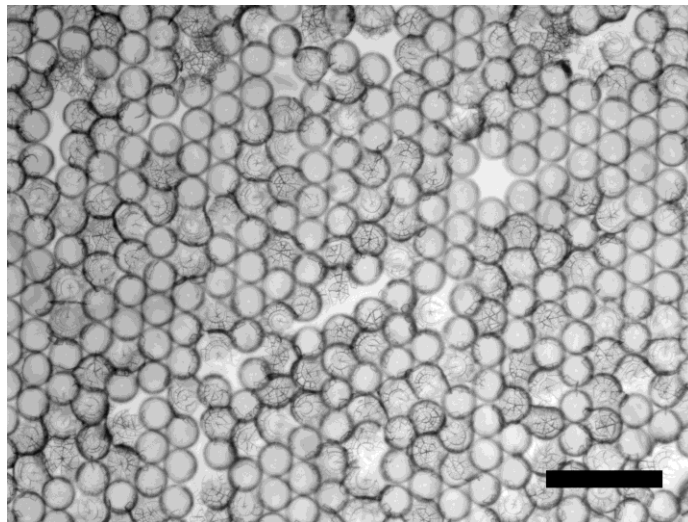


**Figure 2.5** Optical microscopy image of a monolayer of dried bubbles significantly damaged during drying. Scale bar = 200  $\mu\text{m}$

The excellent stability of nanoparticle-shelled bubbles enables the subsequent surface modifications for the Janus bubble preparation. Amphiphilic Janus bubbles are generated by successive deposition of an adhesive layer of chromium ( $\sim 3$  nm) and gold ( $\sim 30$  nm) via thermal evaporation.<sup>49</sup> This process results in the selective formation of a gold layer on the hemisphere of the bubbles facing the gold source as shown in Figure 2.6. The gold hemisphere is rendered hydrophobic by forming a self-assembled monolayer (SAM) of 1-octadecanethiol (ODT).<sup>45-48</sup> The water contact angles of poly(vinyl alcohol) (PVA)-modified  $\text{SiO}_2$  nanoparticle surface and ODT-treated gold layer atop silica nanoparticles are  $65^\circ$  and  $110^\circ$ , respectively.<sup>50-51</sup> These results verify that

the generated Janus bubbles are amphiphilic. To our best knowledge, this is the first report of the formation of amphiphilic Janus bubbles.

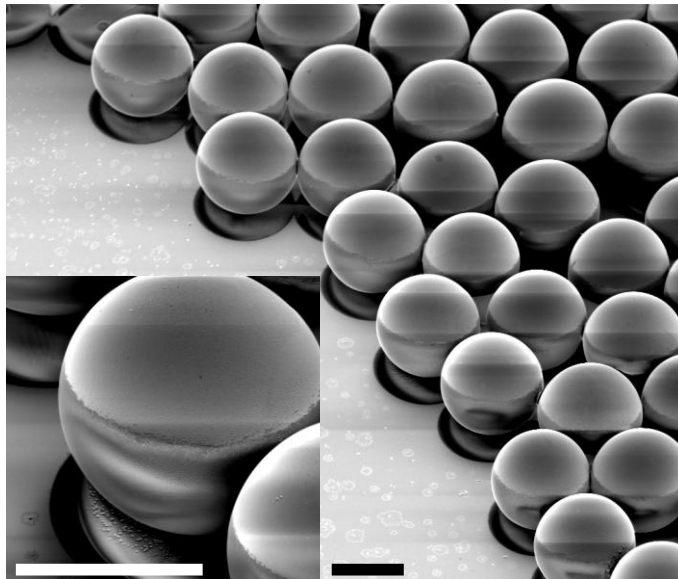


**Figure 2.6** SEM image of a monolayer of Janus bubbles after metal deposition with a gold layer on one hemisphere. Inset shows a high magnification image of a Janus bubble. Diffuse Janus boundary can clearly be seen close to the equator of the bubble. Scale bars = 50  $\mu\text{m}$ .

### 2.3.2 Interfacial Behavior of Janus Bubbles at an Air-Water Interface

Un-modified  $\text{SiO}_2$  nanoparticle-shelled bubbles and amphiphilic Janus bubbles show strikingly different assembly behavior at an air-water interface. Un-modified and Janus bubbles are allowed to collect at the top of a convex air-water interface as shown in Figure 2.7a. In the case of un-modified bubbles (Figure 2.7b), the buoyancy force packs the bubbles into a hexagonal array at the top of the convex air-water surface. The array of collected bubbles shows grain boundaries and defects, which have been observed in two-dimensional bubble rafts.<sup>52</sup> In contrast, Janus bubbles assemble into a fractal-like

structure at an air-water interface as shown in Figure 2.7c. During the assembly, it can be clearly observed that some bubble clusters rotate before assembling into larger clusters. This observation indicates the existence of directional interactions between amphiphilic Janus bubbles at the interface (movies showing the assembly of un-modified and Janus bubbles at a convex air-water interface are available in the Supporting Information of Ref 14).

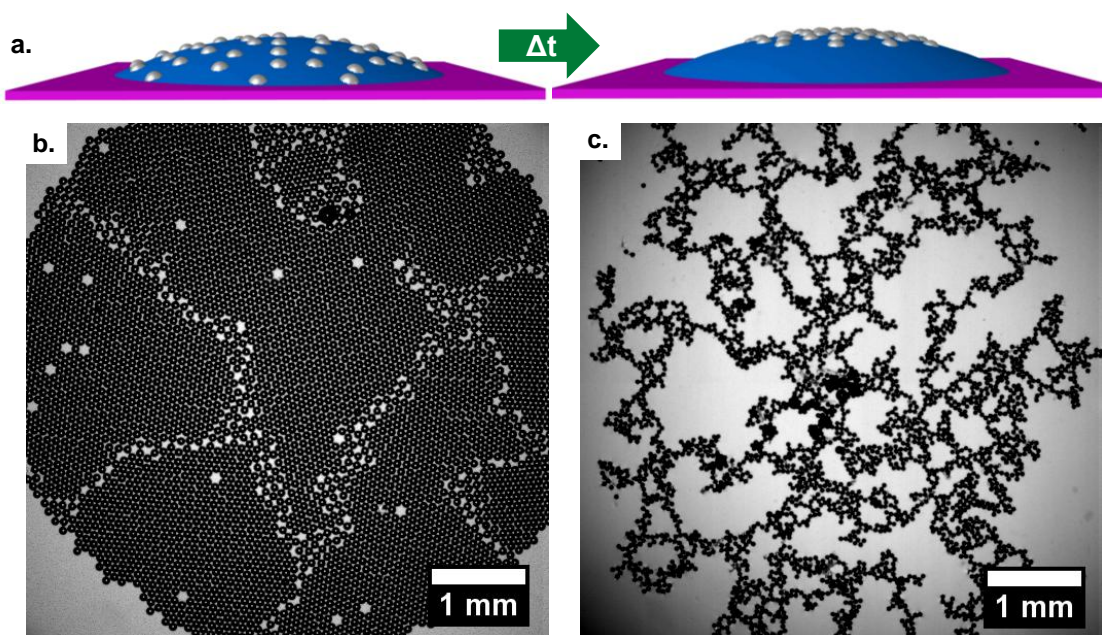


**Figure 2.7** (a) Schematic illustration of the assembly of bubbles at a convex air-water interface. Optical microscopy images of assemblies of (b) un-modified  $\text{SiO}_2$  nanoparticle-shelled bubbles and (c) amphiphilic Janus bubbles at the top of a convex air-water interface.

The assembly of amphiphilic Janus bubbles at an air-water interface suggests that the bubbles interact with one another via long-ranged attractions with directional bonding. We believe the origin of this long-ranged attraction is lateral capillary forces due to the undulation of the three-phase contact line around Janus bubbles. Previous

studies report that the contact line around an amphiphilic Janus particle trapped at an oil/water interface is anchored at the boundary between the two hemispheres.<sup>53-54</sup> It is assumed, in these studies, that the fluid/fluid interface around the particles would remain flat. However, in our case, the boundary between the two sides is not perfectly sharp but rather diffuse and rugged, as can be seen in Figure 2.6. Such diffuse boundary resulting from the line-of-sight evaporation of gold has been observed by others as well.<sup>28, 55-56</sup>

We believe the heterogeneity at the boundary between the two hemispheres plays a critical role in the development of attractions between the amphiphilic Janus bubbles at the air-water interface. Previous theoretical studies report that an irregular contact line around spherical particles trapped at a fluid-fluid interface leads to the deformation of the interface. It is predicted that even small deformations in the interface would induce strong capillary interactions between the particles, much greater than  $k_B T$ . In the case of 1  $\mu\text{m}$  spheres, for example, an interface deformation of 50 nm results in an interaction energy of  $\sim 10^4 k_B T$ .<sup>57-58</sup> These long ranged capillary interactions have been shown to induce the aggregation of interface-trapped particles. Such rugged meniscus around interface-trapped particles is likely due to chemical inhomogeneity, surface roughness or irregular particle shape.<sup>58</sup> In the case of Janus bubbles, chemical heterogeneity is presented by the diffuse boundary between the two hemispheres (Janus boundary). For un-modified bubbles with diameter between 20 and 100  $\mu\text{m}$ , the undulation of the three phase contact line around the bubbles is negligible because the Bond number ( $Bo$ ), which is the ratio of body forces (including gravity and buoyancy forces) to the surface tension, is very small ( $Bo = 10^{-5} \sim 10^{-3}$ ) and also the surface properties of these bubbles are homogeneous.

Thus, un-modified bubbles do not interact with each other via noticeable capillary interactions.

The nature of the attractive interactions between amphiphilic Janus bubbles is characterized by measuring the interaction potential between pairs of Janus bubbles at an air-water interface. To determine the pair potential between amphiphilic Janus bubbles, a force balance is performed using equation 2.1.<sup>59</sup>

$$F_{\text{inert}} = F_{\text{drag}} + F_{\text{inter}} + F_{\text{fluc}} \quad 2.1$$

where  $F_{\text{inert}}$ ,  $F_{\text{drag}}$ ,  $F_{\text{inter}}$  and  $F_{\text{fluc}}$  represent inertial force, drag force, interaction force and thermal fluctuation force, respectively. For a typical velocity on the order of  $100 \mu\text{m s}^{-1}$  and a typical bubble size of  $50 \mu\text{m}$ , inertial and thermal fluctuation forces are negligible compared to interaction and drag forces.<sup>60</sup> Therefore, the interaction force can be obtained by determining the drag force, which can be calculated using the Stokes equation (Equation 2.2):<sup>61</sup>

$$F_{\text{inter}} = -F_{\text{drag}} = -3\pi f_d \eta d v \quad 2.2$$

where  $\eta$  is the viscosity of the fluid,  $d$  is the diameter of the particle, and  $f_d$  denotes the dimensionless drag coefficient for a particle trapped at a fluid-fluid interface. As will be shown below, approximately half of a Janus bubble is submerged under water; thus, we use 0.5 for  $f_d$ .<sup>62-63</sup> The interaction potential is calculated as the integral of the drag force over the interparticle distance,  $R$  (i.e.,  $U(R) = \int F_{\text{inter}} dR$ ). If this pair interaction potential



corresponds to capillary interactions between a pair of Janus bubbles, this energy of interaction is expected to scale as:<sup>58</sup>

$$U(\gamma, H, d, R, m_i) \sim \gamma H^2 \frac{d^{m_A+m_B}}{R^{m_A+m_B}} \sim U_0(\gamma, H, m_i, d) \frac{1}{R^{m_A+m_B}} \quad 2.3$$

where  $\gamma$  is the surface tension,  $H$  is the amplitude of the undulation of the three-phase contact line,  $d$  is the diameter of the bubble,  $R$  is the interbubble distance.  $m_{i (i=A \text{ or } B)}$  is the multipole order on each bubble and the values of  $m_i$  depend on the shape of multipoles.<sup>58</sup> The potential stemming from capillary forces between particles with a randomly undulating three-phase contact line leads to  $m = 4$  (where,  $m = m_A + m_B$ ;  $m_A$  and  $m_B = 2.0$ ).<sup>57-58</sup>

Determination of the interaction potential between pairs of Janus bubbles verify our hypothesis that Janus bubbles are interacting with each other based on quadrupolar capillary interactions. Several movies recording pairs of interacting Janus bubbles ( $d = 54 \mu\text{m}$ ) are digitized by tracking the center-to-center distance ( $R$ ) with time using a standard particle tracking routine<sup>64</sup> (a representative movie is provided in the Supporting Information of Ref<sup>14</sup>). Figure 2.8a shows the particle separation as a function of time showing long-ranged attractions, which can be described by a power law (inset of Figure 2.8a). Janus bubbles are seen to accelerate as they approach each other as seen in Figure 2.8b. The energy of interaction  $U(R)$ , as a function of interbubble spacing ( $R$ ), is calculated using the drag force as a function of separation distance (inset of Figure 2.8b). The attractive potential between these Janus bubbles ( $U_0$ ) is found to be on the order of

$10^6 k_B T$ , confirming the presence of strong capillary interactions between Janus bubbles at the air-water interface.

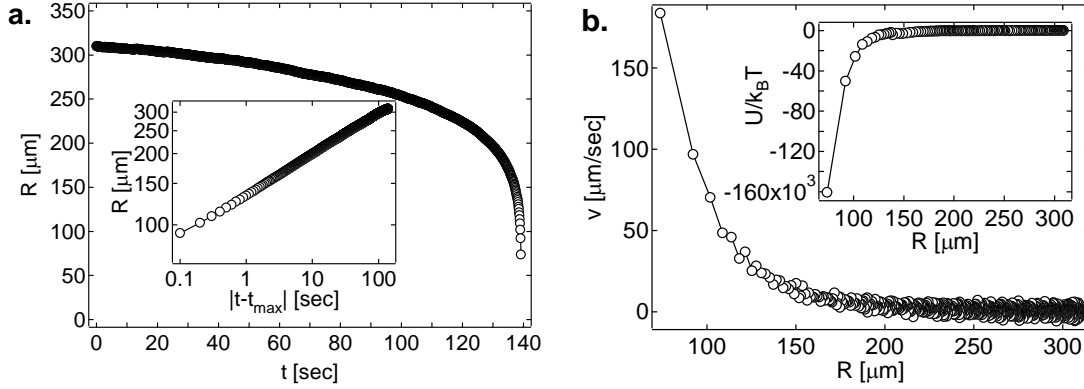


**Figure 2.8** (a) Center-to-center distance ( $R$ ) between two Janus bubbles as a function of time ( $t$ ) (bubble size  $d = 54.0 \mu\text{m}$ ). Inset figure shows the logarithmic plot  $R$  vs.  $(t-t_{max})$  where  $t_{max}$  is the time when the bubbles make contact. (b) Velocity of bubble approach as a function of interbubble distance ( $R$ ) converted from (a). Inset represents the attractive potential determined using Equation 2.2.

To gain deeper insights into the nature of the attractive interactions, we determine the interaction potential for three pairs of Janus bubbles with different sizes. Attractive potential between amphiphilic Janus bubbles, regardless of their size, is consistent with the quadrupolar attractive interactions as can be seen by the slope of the potential as a function of interbubble distance in Figure 2.9 ( $\log U(R)$  vs.  $\log R$ ).<sup>57-58, 65</sup> As Equation 2.3 suggests, the interaction potential between Janus bubbles strongly depends on the diameter of the bubbles ( $d$ ). The attractive potential for three pairs of Janus bubbles (with diameters  $d_1 = 36.0 \mu\text{m}$ ,  $d_2 = 55.6 \mu\text{m}$  and  $d_3 = 86.0 \mu\text{m}$ , respectively) shows that the magnitude of the attraction generally increases with the bubble size (Figure 2.9). The magnitudes of attractive interactions for Janus bubbles at an interbubble distance of  $R =$

100  $\mu\text{m}$  are  $5.1 \times 10^3$ ,  $1.6 \times 10^4$  and  $2.2 \times 10^5 k_B T$  for bubbles with 36.0, 55.6 and 86.0  $\mu\text{m}$  diameter, respectively.

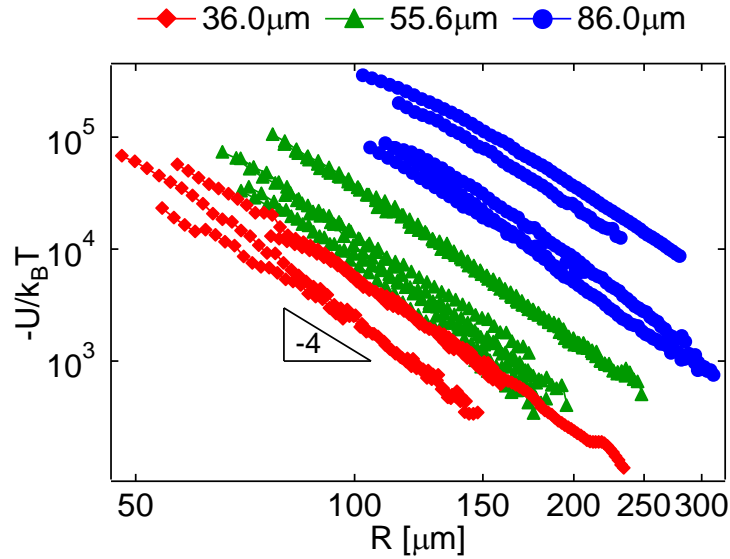


**Figure 2.9** Attractive interaction potential ( $-U(R)/k_B T$ ) between pairs of Janus bubbles of three different sizes as a function of interbubble distance ( $R$ ).

It is important to note, however, that Janus bubbles of the same size do not necessarily have the exact same potential profile in Figure 2.9; that is, attractive interactions between pairs of Janus bubbles of the same size are heterogeneous. The rugged Janus boundary on the bubble surface generates an irregular contact line with a random undulation. This random undulation and its amplitude are likely to be heterogeneous among bubbles of the same size and are believed to be responsible for the heterogeneity in the interaction potentials.<sup>66-67</sup>

### 2.3.3 Direct Observation of Amphiphilic Janus Bubbles at an Air-Water Interface

In addition to the interbubble potential determined based on the force balance (Equation 2.1), the direct observation of Janus bubbles also supports our hypothesis that the deformation of the air-water interface is responsible for the observed long-ranged capillary attractions. We determine the orientation and position of amphiphilic Janus bubbles at the free surface by trapping the bubbles with a gel-based technique<sup>42, 44</sup> and characterize the wetting profiles around the bubbles using optical profilometry. Interface-trapped bubbles are transferred to polydimethylsiloxane (PDMS) and directly imaged under scanning electron microscopy (see Experimental Section for details). The exposed region of the trapped bubbles above the PDMS slabs in Figure 2.10a and b corresponds to the portion of the bubbles that were submerged in the aqueous phase. These images show that approximately half of the amphiphilic Janus bubbles were submerged below the interface (Figure 2.10a), whereas the majority of the un-modified bubbles were immersed in the water (Figure 2.10b). These results clearly show that the position of amphiphilic Janus bubbles is significantly different from that of the un-modified bubbles with respect to the air-water interface.

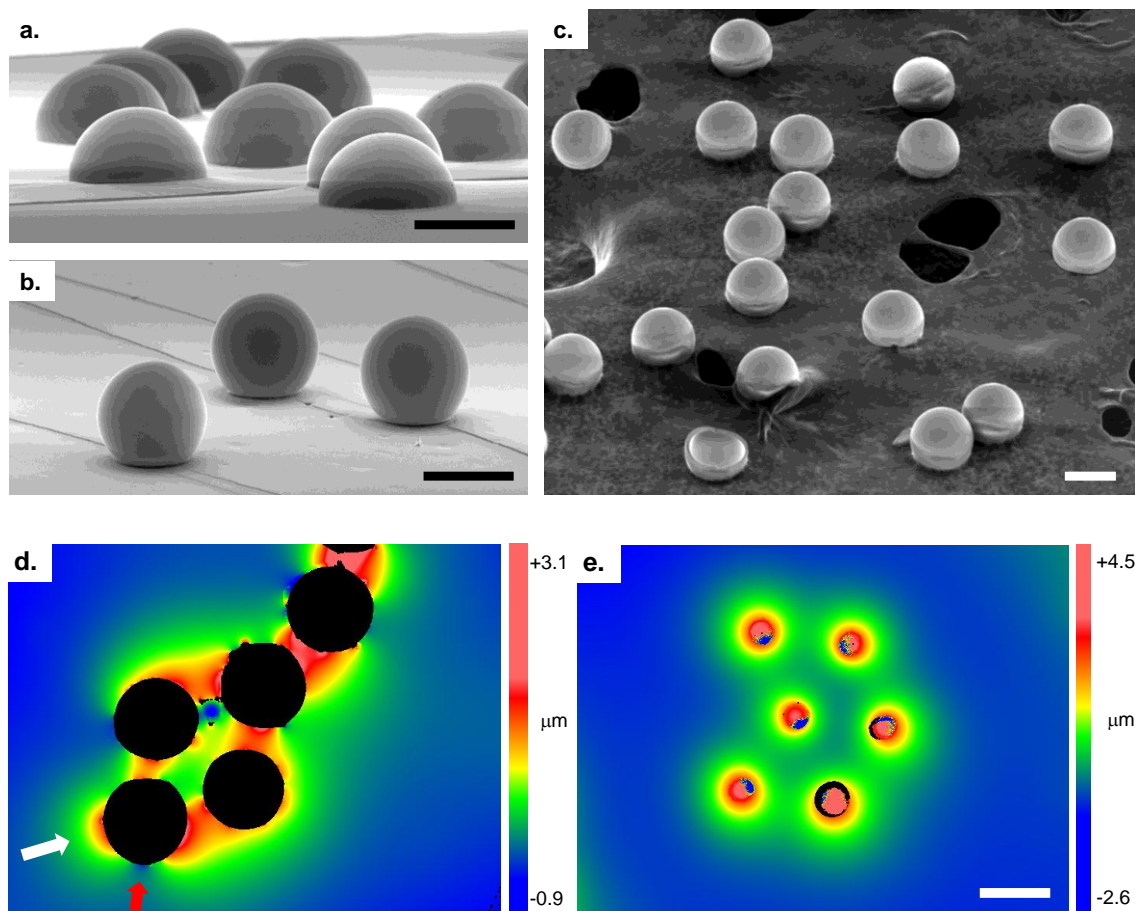


**Figure 2.10** SEM images of (a) Janus bubbles and (b) un-modified SiO<sub>2</sub> nanoparticle-shelled bubbles embedded in PDMS slabs showing the difference in the position of bubbles with respect to the air-water interface, and (c) Janus bubbles attached to a double-sided tape showing their orientation at the air-water interface. Profilometry contour plots showing the shape of the interface around (d) Janus bubbles and (e) unmodified nanoparticle-shelled bubbles. White arrow and red arrow indicate positive and negative deformation of the air-water interface, respectively. Scale bars = 50 μm.

To analyze the orientation of the bubbles at the interface, the bubbles embedded in a PDMS slab are transferred to a piece of double-sided carbon tape and imaged using SEM.<sup>65</sup> As shown in Figure 2.10c, 90% of the Janus bubbles are oriented with the gold hemisphere facing the air phase. This result confirms that most of the Janus bubbles

remain at their equilibrium position at the air-water interface as suggested by theories and simulations.<sup>32, 39, 53, 68</sup>

In addition to these results, the optical profilometry of interface-trapped amphiphilic Janus bubbles directly proves the presence of interface deformation. Interface deformation around amphiphilic Janus bubbles and un-modified bubbles are shown in Figure 2.10d and e, respectively. It can be seen that the upper hemisphere of Janus bubbles protrudes above the level of the flat interface (Figure 2.10d), whereas most of un-modified SiO<sub>2</sub> nanoparticle-shelled bubbles is immersed in the aqueous phase. These results are consistent with those based on the gel-trapping method (Figure 2.10a and b). More importantly, the interface around Janus bubbles is seen to rise above and also deflect below the flat interface, which are indicated by white and red arrows in Figure 2.10d, respectively. In addition, between the Janus bubbles that are in contact with each other, the interface undergoes capillary imbibitions rising above the level of the flat interface. Such an interface deformation is a strong indication that the bubbles are interacting with each other through capillary attractions.<sup>69-71</sup> In contrast, the air-water interface around the un-modified bubbles does not show any significant undulation as seen in Figure 2.10e. The lack of the interface deformation and of capillary imbibitions is consistent with the lack of detectable attractive interactions between un-modified bubbles. These results clearly verify our hypothesis that the heterogeneity in chemical composition around Janus boundary generates irregularities in the three-phase contact line, which causes long-ranged capillary attractions that can be approximated by capillary quadrupolar interactions.

## 2.4 Conclusions

We present a new method for the generation of amphiphilic Janus bubbles using ultra-stable nanoparticle-shelled bubbles and investigate the assembly of these Janus bubbles at an air-water interface. These shelled bubbles are prepared using a microfluidic technique, which enables a precise control over the dimensions of the bubbles. Bubbles with thick shells can overcome drying and re-suspension processes without significant changes in their structure, allowing us to generate Janus bubbles by metal evaporation onto a dried bubble monolayer. We observe long ranged capillary attractions between Janus bubbles at an air-water interface and confirm that these attractive interactions are due to capillary quadrupoles. In addition to the determination of interbubble potential, optical profilometry directly shows that the random undulation of the air-water interface caused by the diffuse Janus boundary is the source of the capillary quadrupolar interactions. We believe the anisotropic interactions between Janus bubbles at the air-water interface represent a unique method to form a percolated structure at a low surface coverage to make, for example, a conductive network. Also, this fractal like structure can potentially be used for the assembly of porous materials with unique acoustic properties. In addition, Janus bubbles could be used to generate bubble rafts with anisotropic interactions, which will serve as a model system to study atomic solids with directional bonding.

# Chapter 3. Tailoring the Mechanical Properties of Nanoparticle-Shelled Bubbles

Adapted from T. Brugarolas, D. S. Gianola, L. Zhang, G. M. Campbell, J. L. Bassani, G. Feng, and D. Lee. Tailoring and Understanding the Mechanical Properties of Nanoparticle-Shelled Bubbles, 2014, ACS Applied Materials & Interfaces DOI: 10.1021/am502290h. Copyright (2014) American Chemical Society.

## 3.1 Introduction

Light-weight materials enhance the energy efficiency of vehicles and equipment used in transportation, aerospace and construction industries;<sup>72-75</sup> however, finding a low-density material that possesses a desirable set of mechanical properties is challenging because the stiffness and strength of materials are generally proportional to their density.<sup>3, 76-78</sup> One approach that addresses this limitation is the fabrication of composites made of polymer and strong hollow particles, also known as bubbles.<sup>79</sup> The presence of these bubbles made of an inorganic material, such as glass, decreases the density of the composite and at the same time increases its specific strength. In addition, the incorporation of bubbles can potentially impart unique thermal, optical and acoustic properties to the composites.<sup>80-85</sup>

Needless to say, the mechanical properties of individual bubbles greatly affect the properties of these composites, also known as syntactic foams.<sup>86-88</sup> It is highly desirable, therefore, to control the mechanical response of bubbles to suit the specific requirements of the final application. For example, high strength and light weight or high buoyancy is required in composite materials used for aircraft structures and underwater modules such



as deep-sea exploration vehicles.<sup>75, 89</sup> In contrast, hollow particles with high deformability would be useful in generating flexible portable devices,<sup>90</sup> noise control structures,<sup>91</sup> impact absorbers<sup>92</sup> and sports equipment.<sup>93</sup> In addition to achieving desirable mechanical properties, high uniformity in the size and properties of these hollow particles could enable accurate prediction of the structure-property relationship of the composites containing bubbles.<sup>94</sup> Unfortunately, conventional methods of bubble preparation result in particles with large heterogeneity in size and properties.<sup>6</sup> It is also challenging to tailor the mechanical response and to systematically characterize individual bubbles.<sup>95-96</sup> More importantly, even a small number of very weak (*i.e.*, defective) bubbles could result in mechanically fragile regions within the final composites, seriously jeopardizing the reliability of these hollow particles as fillers to generate mechanically robust composites for applications involving sustained stresses.<sup>97</sup>

In this Chapter, we use a microfluidic technique to generate highly monodisperse nanoparticle-shelled bubbles<sup>12, 98-99</sup> and demonstrate that their mechanical properties can be tailored using thermal treatment. The mechanical response of these bubbles is studied experimentally using quantitative *ex situ* and *in situ* characterization methods and computationally using finite element analysis (FEA, see Chapter 4). We show that thermal treatment significantly enhances the strength of nanoparticle-shelled bubbles and also changes the deformation mode of the bubbles under load. Furthermore, we show that the failure mode of these bubbles in a polymer-bubble composite depends strongly on the structure of the individual bubbles.

## 3.2 Experimental Section

### 3.2.1 Generation of Nanoparticle-Shelled Bubbles

Nanoparticle-shelled bubbles are generated using a glass microfluidic device that combines co-flow and flow-focusing geometry as previously reported.<sup>12</sup> The three immiscible fluid phases used are nitrogen (AirGas, Inc.) as the inner phase, hydrophobic silica nanoparticles (15 nm average diameter) suspended in toluene (Nissan Chemical Industries, Ltd.) at an approximate concentration of 28 wt% as the middle phase, and an aqueous solution containing poly(vinyl alcohol) (PVA, 87-89% hydrolyzed, average Mw=13000-23000, Sigma-Aldrich Co. LLC) at a concentration of 2wt% as the outer phase. The geometry of the gas-in-oil-in-water (G/O/W) compound bubbles is controlled by tuning the flow rates during the microfluidic generation. The shell thickness and diameter of the bubble are tuned to be above a critical value to ensure the bubbles remain stable upon drying.<sup>98</sup> The G/O/W compound bubbles are collected in a convex air-water interface forming a monolayer of bubbles to facilitate the fast evaporation of the toluene in the middle phase. When the nanoparticle-shelled bubbles are formed, they are washed to remove the excess of PVA by exchanging the water in the collecting container for three times. A monolayer of as-assembled bubbles is formed by drying a drop of bubble suspension on a piece of silicon wafer.

### **3.2.2 Thermal Treatment: Calcination and Sintering Processes**

Thermal treatment is performed on the monolayer of dried bubbles on a silicon wafer. The bubbles are calcined at 700 °C using a Thermo Scientific Thermolyne Furnace Benchtop Muffle type F47900 for approximately 3 hours. The sample is then cooled down to room temperature by removing the sample from the furnace. For the generation of sintered bubbles, a monolayer of as-assembled bubbles on a silicon wafer is sintered at 1200 °C for a short period of time. The furnace is allowed to reach 1200 °C and then is turned off to cool down, when temperature in the furnace cools down to 700-800 °C the sample is taken out of the furnace.

### **3.2.3 Characterization of Bubbles and Bubble Shells**

As-assembled, calcined and sintered bubbles are resuspended in water to verify their integrity and geometry. Calcined bubbles easily detach from the silicon wafer by placing a drop of water. Calcined bubbles allow water to permeate through the shells into their cores due to their porosity and change in their wettability (see Figure 3.1). Sintered bubbles occasionally remain attached to the substrate after the sintering process. The detachment of the bubbles from the substrate is achieved by introducing the silicon wafer with the attached bubbles in a glass vial containing DI water, and performing a brief ultrasonication (< 1 sec) using a bath ultrasonicator (9.5 L Fisher-Scientific FS-110D). Approximately, 90% of the bubbles detach from the Si wafer without significant damage.

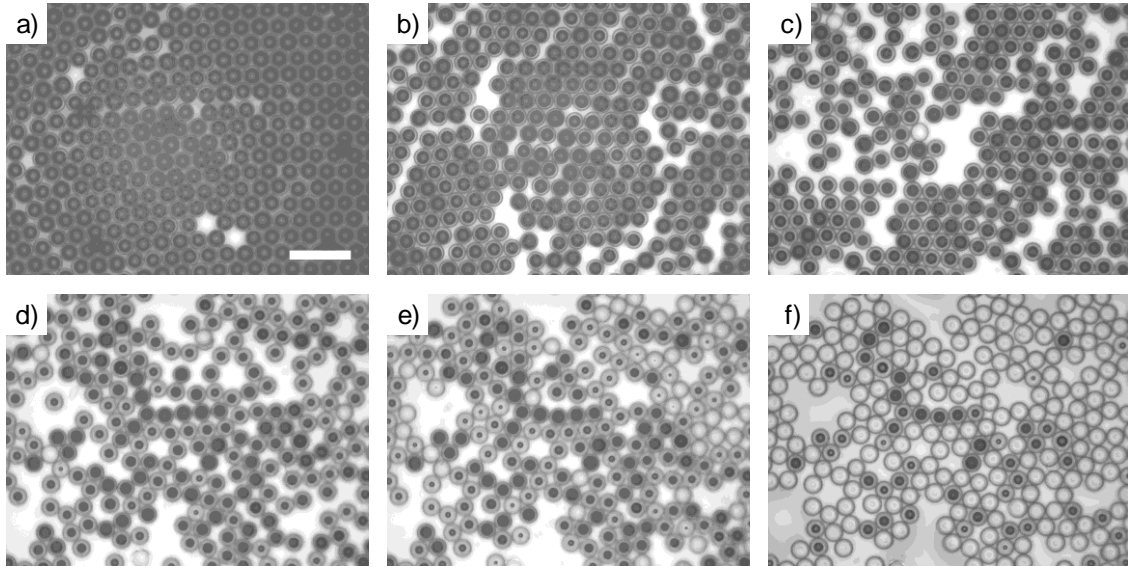


**Figure 3.1** Permeability of calcined bubbles. A sample of calcined bubbles is wetted by DI water and the behavior is captured with an optical microscope for approximately 20 minutes. Water slowly permeates the porous shell and fills the shelled bubble with water. From (a) to (f) calcined bubbles at different times during the permeation of the water into the shell. Scale bar 200  $\mu\text{m}$ .

Characterization of the as-assembled, calcined and sintered bubbles is performed by optical microscopy using a Zeiss Axioplan 2 upright microscope equipped with a Q-imaging Retiga 2000R Fast 1394 CCD digital camera. Images of the monolayer of dried bubbles atop a silicon wafer before and after the heat treatment are taken in reflection mode while resuspended bubbles are imaged in transmission mode. Image J software is used for the image analysis to determine average bubble diameter, size distribution, stability and permeability. Scanning electron microscopy (SEM) images are taken using a FEI Quanta 600 FEG ESEM at 5-10 kV. Average shell thickness values are determined by averaging measurements obtained from the analysis of SEM images taken on fractured bubbles.

### 3.2.4 Nanoindentation

Nanoindentation on as-assembled, calcined and sintered bubbles is performed using a Nano Indenter™ G200 from Agilent™ Technologies Inc. A 10 μm radius 60° sphero-conical rigid indenter is used to obtain load-displacement curves using a constant ratio of loading rate to load ( $\dot{P}/P = \text{constant}$ ) of 0.04 s<sup>-1</sup>. Thermal drift correction is performed. For nanoindentation tests, the bubbles are deposited onto Si wafers. The Si wafer plates are much stiffer than the bubbles and undergo negligible deformation.

### 3.2.5 *In situ* Compression

Quantitative *in situ* mechanical testing of bubble specimens is performed using a novel custom-built micro- and nanomechanical testing system installed in a high resolution field-emission SEM (FEI Quanta 600F).<sup>100</sup> The testing platform consists of three primary components: (i) a stiff piezoelectric actuator operated in closed-loop control mode (1 nm resolution), enabling displacement-controlled testing, (ii) a 6 degree-of-freedom closed-loop nanopositioning system (SmarAct SmarPod, with 1 nm and 1 μrad resolution), and (iii) a capacitive based force sensing probe (Femtools FT-S10000 Microforce Sensing Probe, with 0.5 μN resolution at 10 Hz acquisition rate). A square Si flat punch (50 x 50 μm) at the tip of the load cell is used for compression testing.

Special considerations are made during testing to eliminate the effects of misalignment between the flat punch (and thus the load cell axis) and the testing specimen. Alignment is achieved by using the nanopositioning stage. In-plane alignment is relatively straightforward and achieved by rotation and translation of the tip relative to the specimen with feedback based on SEM observation. We achieve the optimal out-of-plane alignment by maximizing the contact stiffness as a function of rotation angle during low load indentation experiments on the substrate adjacent to bubble specimens. Compression tests are operated in displacement control to achieve displacement rates of approximately 40 nm/s and 37 nm/s, for as-assembled and calcined bubbles respectively, and SEM images are simultaneously acquired. For *in situ* compression tests, the bubbles are deposited onto Si wafers. The Si wafer plates are much stiffer than the bubbles and undergo negligible deformation.

### **3.2.6 Polymer-Bubble Composite Generation**

Layer-by-layer (LbL) polymer-bubble composite is generated by first spin coating a poly(vinyl alcohol) sacrificial layer on a glass slide (approximated size of 2 x 2 cm<sup>2</sup>) using a 2 wt% PVA (87-89% hydrolyzed, average Mw = 13000-23000, Sigma-Aldrich Co. LLC) in water solution at 2000 rpm. Subsequently a polystyrene (PS, approx Mw = 190000, Scientific Polymer Products, Inc.) layer is spin coated with a 20 wt% PS solution in toluene at 2000 rpm. Additional spin coating steps with PS solution are performed to increase the thickness of the final PS layer up to the desired thickness. The film is dried at

room conditions and is used to collect the bubbles using a Langmuir-Schaeffer technique.<sup>101</sup> A monolayer of bubbles is then dried on top of the PS film. Subsequently, a new layer of PS is spin coated on top of the bubbles covering the bubble monolayer. This process is repeated reaching the final desired composite thickness. The sacrificial PVA layer can be dissolved in water by immersing the film in water overnight obtaining a free standing LbL film of bubbles and polystyrene. Characterization of the fractured films is made by SEM.

## **3.3 Results and Discussion**

### **3.3.1 Generation and Thermal Treatment of Monodisperse Nanoparticle-Shelled Bubbles**

Nanoparticle-shelled bubbles are generated using microfluidic gas-in-oil-in-water (G/O/W) compound bubbles as templates.<sup>12-13, 16, 98, 102-107</sup> The three immiscible fluid phases used for the generation of G/O/W compound bubbles in a glass capillary microfluidic device are nitrogen, hydrophobic silica nanoparticles suspended in toluene and an aqueous solution containing polyvinylalcohol (PVA) forming the inner, middle and outer phases of the compound bubble, respectively. This microfluidic approach permits the preparation of monodisperse compound bubbles at a high rate with precise control over diameter and shell thickness by controlling the geometry of the microfluidic device as well as the flow rates and physical properties (viscosity, density, surface tension etc.) of the three fluids.<sup>12, 99</sup> PVA in the outer phase stabilizes the oil-water

interface during the microfluidic formation of the compound bubbles, preventing their coalescence and rupture.<sup>12, 108</sup> After the generation of G/O/W compound bubbles, the toluene from the middle phase is allowed to evaporate at room temperature. The suspended silica nanoparticles jam at the air-water interface, forming a solid and water-impermeable shell around the gas bubble as shown in Figure 3.2. This thin shell formed by the compaction of silica nanoparticles in the middle phase imparts long-term stability to the bubbles.<sup>12</sup> The shell comprises randomly packed silica nanoparticles and residual PVA remaining on the shell surface. It is important to note that the silica nanoparticles have an organic layer that renders them hydrophobic and colloidally stable in toluene. This organic coating on the silica nanoparticles remains in the shell after the evaporation of toluene from the oil phase of the compound bubble.

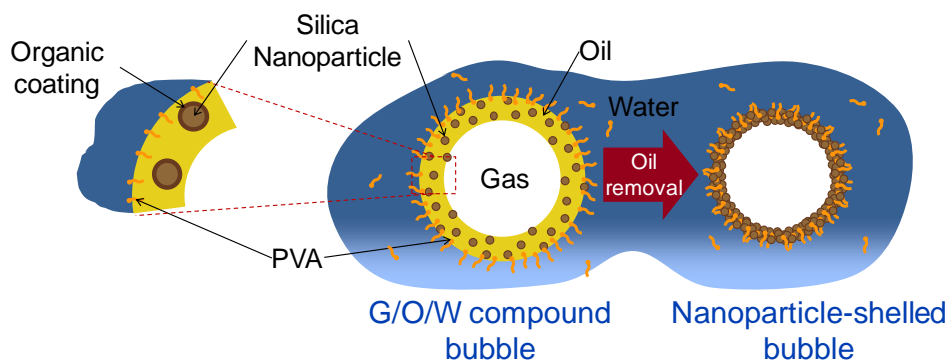


**Figure 3.2** Schematic illustration of nanoparticle-shelled bubble formation from a gas-in-oil-in-water (G/O/W) compound bubble generated with a microfluidic technique. The removal of the toluene forming the oil layer, drives jamming and compaction of the suspended silica nanoparticles, which forms a solid shell around the inner gas phase.

Nanoparticle-shelled bubbles are dried on top of a silicon substrate forming a monolayer of bubbles. Our previous study showed that it is important to keep the ratio of



shell thickness to bubble radius above a critical value (0.042) to keep these bubbles from collapsing during water evaporation.<sup>98</sup> In this work, we generate nanoparticle-shelled bubbles that have an initial diameter of 40 – 60  $\mu\text{m}$  and an average shell thickness of 2 – 3  $\mu\text{m}$ . The dried bubbles on the Si wafer are further modified by thermal treatment as shown in Figure 3.4a.<sup>109-111</sup> Bubbles are calcined at 700  $^{\circ}\text{C}$ , which completely removes all organic components from their shells as confirmed by thermogravimetric analysis (TGA; see Figure 3.3). The removal of the organic components renders the shell porous and water-permeable (see Figure 3.1). The diameter of the bubbles slightly decreases due to the elimination of the organics and the partial fusion of silica nanoparticles upon calcination. The calcination process, however, does not compromise the sphericity or integrity of the bubbles. The bubble outer surface remains rough and porous as shown by the SEM micrograph in the inset of Figure 3.4b.

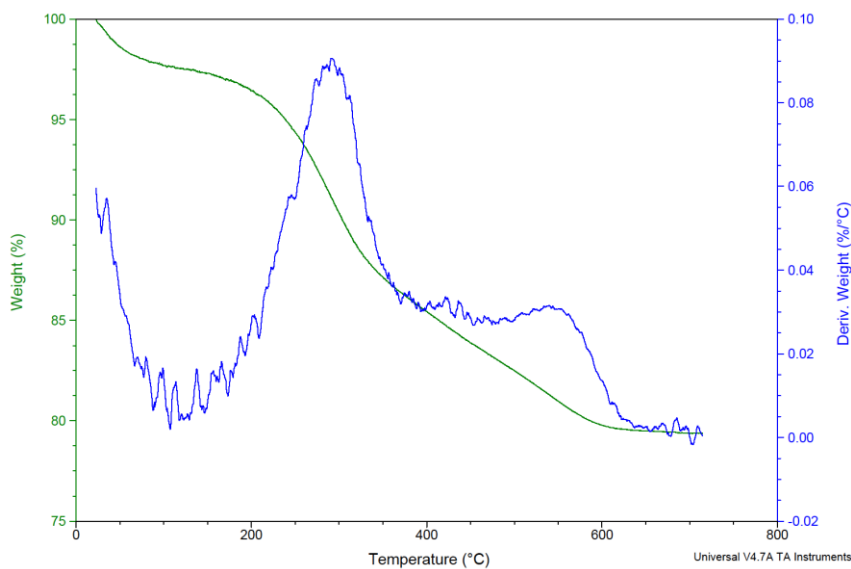


**Figure 3.3** Thermogravimetric analysis of as-assembled nanoparticle-shelled bubbles indicating a complete removal of organic components around 650 $^{\circ}\text{C}$ .

The bubbles can be further modified by subjecting them to a 1200 °C thermal treatment. At this temperature, silica nanoparticles in the shell completely sinter to form a non-porous solid silica structure. Although this temperature is well below the melting temperature of bulk SiO<sub>2</sub> (~ 1600 °C), the use of nanoparticles enhances the processability of these bubbles by lowering the sintering temperature significantly. The shell, as can be seen in the inset of Figure 3.4b, becomes smooth, indicating that it has lost its porosity.

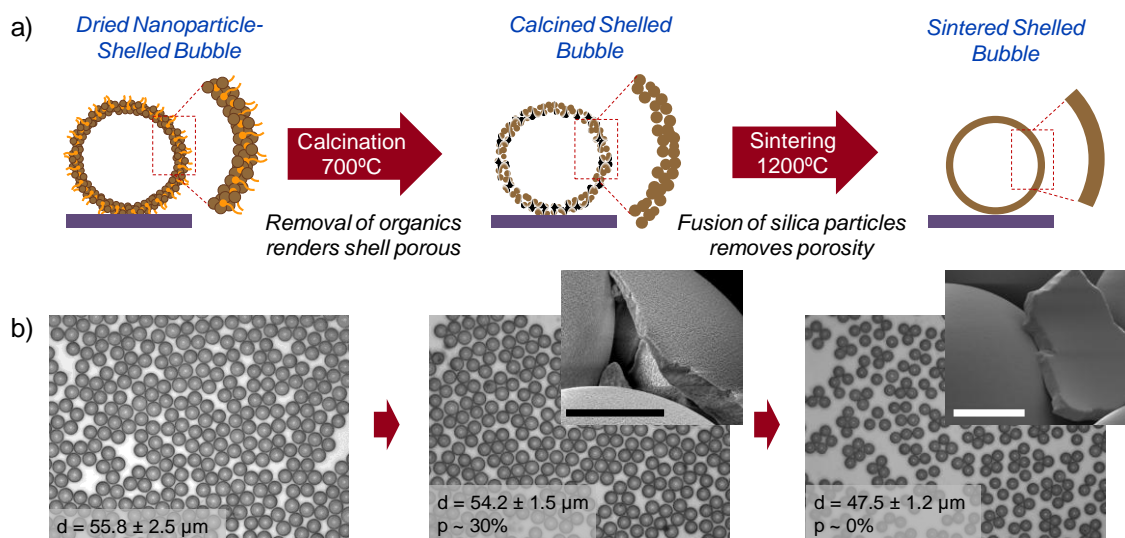


**Figure 3.4** (a) Schematic representation of physical modification of nanoparticle-shelled bubbles with thermal treatment, (b) optical micrographs (inset: SEM micrographs) of nanoparticle-shelled bubbles on a substrate after heat treatment.  $d$  and  $p$  represent the outer diameter of the bubbles and the porosity of the bubble shells, respectively. Inset scale bars = 10  $\mu\text{m}$ .

The diameter of the bubble and the shell thickness decrease significantly from their original values upon sintering; however, the bubbles maintain their spherical geometry. The sintering process partially fuses some bubbles with each other or with the

substrate, especially if the sintering time is extended beyond three hours. However, due to the high strength of the sintered shells, the bubbles can be readily separated and redispersed with little damage using brief sonication (< 1 sec). These bubbles float when redispersed in water, indicating that the shell has become dense and lost its porosity.

### 3.3.2 Mechanical Characterization of Bubbles using Nanoindentation

In addition to changes in the shell structure and dimension of the bubbles, the calcination and sintering processes described above significantly change the mechanical properties of individual nanoparticle-shelled bubbles. To fully understand the effect of thermal treatment on the mechanical response of nanoparticle-shelled bubbles, we perform *ex situ* nanoindentation on single bubbles.<sup>95, 112</sup> We use a 10  $\mu\text{m}$ -radius  $60^\circ$  sphero-conical indenter as schematically illustrated in Figure 3.6a. The indenter and a bubble on a flat substrate are aligned through the main axis perpendicular to the substrate, assuring that the bubble is center-loaded without any sliding during indentation test. The bubbles are loaded at a constant ratio of loading rate to load ( $\dot{P}/P = \text{constant}$ ) of  $0.04 \text{ s}^{-1}$  until failure is detected. Failure is assigned to the first large pop-in event observed on the load-displacement curve (see as example Figure 3.5).

The determination of failure by fracture during nanoindentation of individual bubbles is easily determined for as-assembled and sintered bubbles, where the corresponding load-displacement curves result in a sudden displacement reaching the substrate. In the case of calcined bubbles, the determination of failure is conservatively

assigned to the first large pop-in event observed in the load-displacement curve, because the possible cause of those pop-in events is likely to be cracks forming. Figure 3.5 shows the load-displacement data for the calcined bubbles tests, including the raw data and the data used for the analysis.

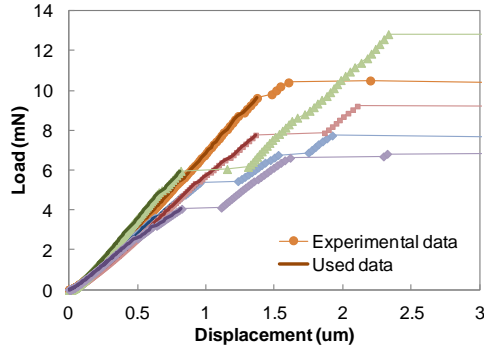


**Figure 3.5** Determination of failure for calcined bubbles from nanoindentation results.

The average diameter and shell thickness of as-assembled, calcined and sintered bubbles used for all subsequent mechanical characterization are summarized in Table 3.1. Load-displacement curves are recorded for all experiments and plotted as shown in Figure 3.6.

**Table 3.1** Diameter and shell thickness of mechanically characterized shelled bubbles

	Diameter, $d$ [ $\mu\text{m}$ ]	Shell thickness, $t$ [ $\mu\text{m}$ ]
As-assembled bubbles	$40.6 \pm 1.1$	$2.9 \pm 0.5$
Calcined bubbles	$37.8 \pm 1.6$	$2.7 \pm 0.6$
Sintered bubbles	$34.6 \pm 1.1$	$2.6 \pm 0.6$

Seven individual as-assembled bubbles are tested, and the load-displacement curves are shown in Figure 3.6b. The response of these as-assembled bubbles shows nonlinear mechanical behavior (Figure 3.6b), reaching an average failure load  $P_f = 3.6 \pm 1.1$  mN and an average failure deflection  $\delta_f = 3.5 \pm 0.8$   $\mu\text{m}$ , amounting to an 8.7 % deflection relative to the initial diameter ( $\delta_f/d$ ). The energy to failure extracted by integrating the load-displacement curves up to the point of failure, has an average value  $U_f = 7.7 \pm 3.2$  mN $\cdot\mu\text{m}$ . Pauchard and Rica previously studied the deformation mechanisms of an elastic spherical shell with a thick wall ( $t/R \sim 1/10$ , where  $t$  and  $R$  are the thickness and the radius of the shell, respectively), and observed a sharp transition to non-linear behavior when buckling occurs.<sup>113</sup> The nonlinear behavior of as-assembled bubbles cannot be tied to such a buckling phenomenon because the deflection of the bubbles in our test is relatively small ( $\delta/t < 2$ , where  $\delta$  is the deflection imposed on the shell). The nonlinear behavior suggests an inelastic response governing the mechanical properties of as-assembled bubbles, which we investigate in more detail below.

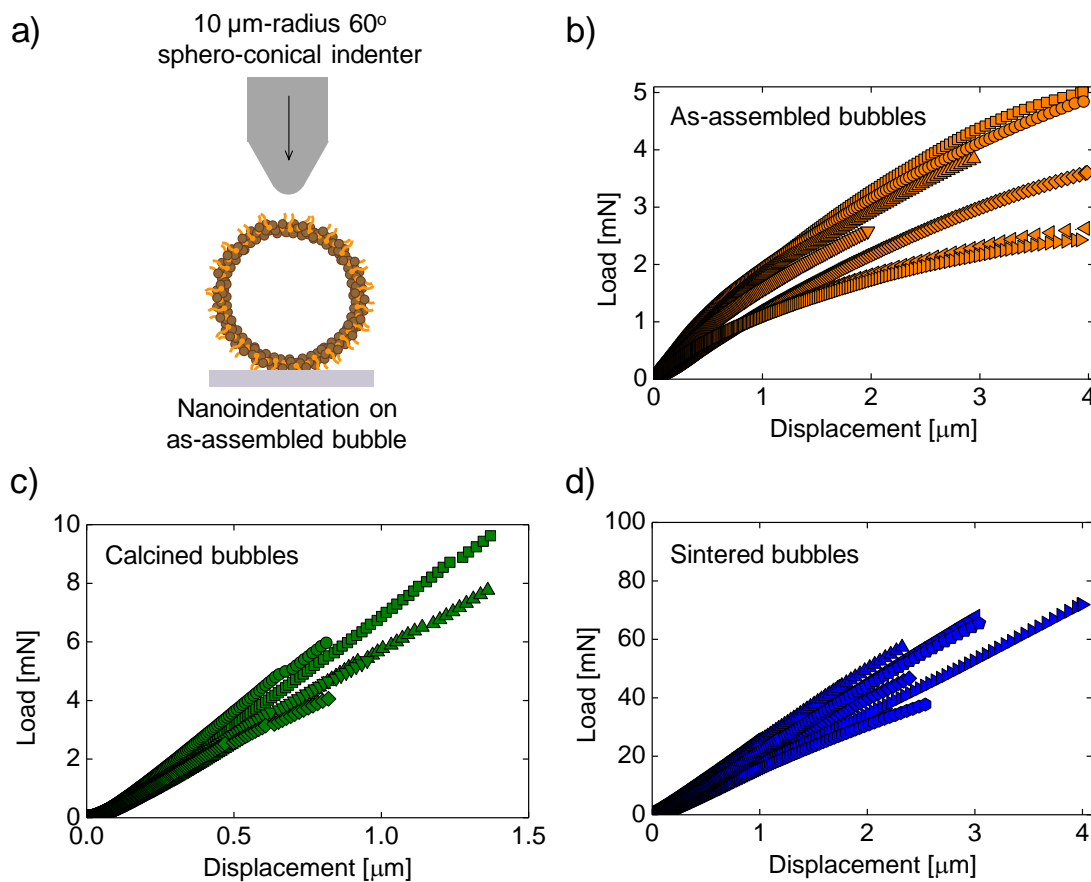


**Figure 3.6** (a) Schematic illustration of nanoindentation on a single bubble with a sphero-conical indenter. Load-displacement results from *ex situ* nanoindentation tests performed on (b) seven as-assembled bubbles, (c) five calcined bubbles, and (d) nine sintered bubbles.

Similar nanoindentation tests are performed on calcined and sintered bubbles. Figure 3.6c shows the load-displacement responses of five different calcined bubbles tested. In contrast to what is observed for the as-assembled bubbles, the calcined bubbles respond linearly to the applied load, implying a predominantly elastic behavior. The failure load of the calcined bubbles is larger than as-assembled bubbles, reaching an average load  $P_f = 6.5 \pm 2.1$  mN. The average failure deflection of calcined bubbles, however, is significantly smaller than that of the as-assembled bubbles; the average

deflection  $\delta_f = 1.1 \pm 0.3 \mu\text{m}$ , a mere 2.8 % of the initial diameter. The average energy to failure of the calcined bubbles  $U_f = 3.6 \pm 1.9 \text{ mN}\cdot\mu\text{m}$ . These results suggest that the calcination process has strengthened the bubble shells, but the absence of organics in the shell causes a more brittle response, reduced deformability and energy to failure.

Sintered bubbles also respond linearly to nanoindentation as shown by the nine bubbles tested in Figure 3.6d. The sintered bubbles present a significantly higher strength and stiffness compared to calcined and as-assembled bubbles. The average failure load for these sintered bubbles is  $P_f = 50.3 \pm 16.1 \text{ mN}$ , an order of magnitude larger than that of calcined ones. It is interesting to note that the deformability of sintered bubbles is also greater than that of calcined bubbles reaching an average deflection  $\delta_f = 2.5 \pm 0.8 \mu\text{m}$ , amounting to a 7.2 % of the initial diameter of the bubble. The average energy to failure of the sintered bubbles is  $U_f = 66.7 \pm 39.4 \text{ mN}\cdot\mu\text{m}$ . Remarkably, the maximum deflection of the sintered bubbles is quite similar to that of the original as-assembled bubbles, but the energy to failure is an order of magnitude higher. The sintering process has created a shell that is dense and non-porous, which significantly affect the mechanical response of the bubbles to indentation resulting in high strength, stiffness, large deformability, and exceptionally high energy to failure (toughness). The mechanical properties of the bubbles will be summarized and compared later.

### 3.3.3 Quantitative *In situ* Mechanical Characterization of As-Assembled and Calcined Bubbles

Quantitative *in situ* mechanical characterization methods provide invaluable information that cannot be readily obtained via *ex situ* techniques by allowing for real-time monitoring of deformation and failure processes.<sup>114</sup> Here we directly observe the mechanical response and failure of individual as-assembled and calcined bubbles under compression. A flat indenter installed inside a scanning electron microscope (SEM) chamber is used to apply uniaxial compression at a constant nominal strain rate  $\dot{\delta}/d = 0.001 \text{ s}^{-1}$  on individual bubbles on a planar substrate (Si wafer). We simultaneously obtain quantitative information on the load-displacement response that occurs during compression.<sup>100, 114</sup>

We directly observe the plasticity of an as-assembled bubble by applying and removing a compressive load prior to fracture. As can be seen from the overlaid SEM images of the as-assembled bubble after multiple load-unload tests (Figure 3.7a), the bubble undergoes a permanent deformation. In contrast, a calcined bubble returns to its original shape without any observable permanent deformation (Figure 3.7b), indicating a purely elastic response. The quantitative load-displacement curves for the two bubbles also show that the as-assembled bubble permanently deforms, whereas the calcined bubble completely recovers its original shape after one load-unload cycle (Figure 3.7c). Also noteworthy is the fact that the as-assembled bubbles display hysteresis in the load-displacement curves and permanent deformation upon unloading as seen in Figure 3.7c.



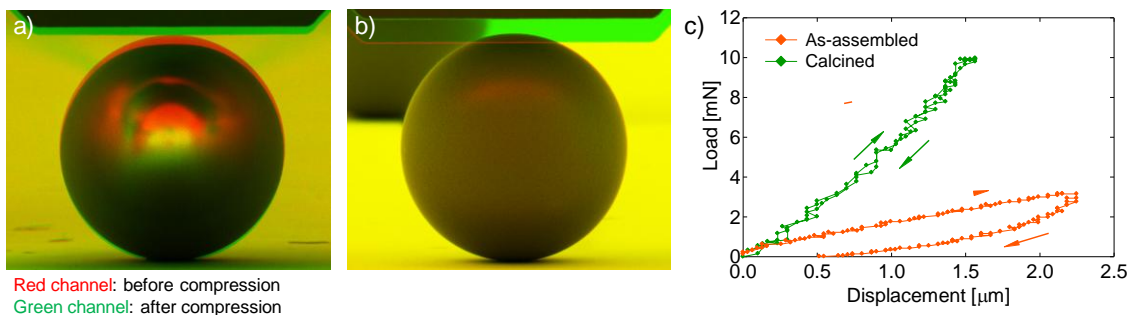


**Figure 3.7** Superimposed SEM images of (a) as-assembled and (b) calcined bubbles before and after load-unload test. (c) Load-displacement curves of the two bubbles after load-unload cycles. Displacement for each bubble is kept low to ensure that no fracture is observed.

We also compare the failure mechanisms of as-assembled and calcined bubbles by subjecting them to large compressive loads. Figure 3.8 presents a collection of movie frames showing the compression of an as-assembled bubble (left) and a calcined bubble (right) between two planar surfaces (full movies are available in the Supporting Information of Ref 115). Images on the left column of Figure 3.8 show that an as-assembled bubble undergoes a significant deformation before the indenter moves downward suddenly; this sudden downward movement coincides with a precipitous drop in the load-displacement curve (from b to c in the left column of Figure 3.8), indicating fracture of the as-assembled bubble. The crack, although not clearly visible because it runs parallel to the viewing plane, vertically splits the as-assembled bubble into two halves (indicated by the red arrow in Figure 3.8d of the left column). Following this first crack, the fractured bubble remains in contact between the two plates. We believe that this first crack initiates at the pole adjacent to the flat indenter. After the first fracture of as-assembled bubbles, the two split halves continue to deform significantly under further compression (additional 5  $\mu\text{m}$ ) before a second fracture initiates. Interestingly, the second

crack consistently propagates horizontally (parallel to the two plates), denoted by the red arrow in Figure 3.8e left, in all of the six as-assembled samples we test. Additional vertical cracks appear as the fractured bubble shell is further compressed, indicated by the red arrow in Figure 3.8f left.

The failure of stiffer calcined bubbles is quite different from that of as-assembled bubbles. After a calcined bubble comes in contact with the flat indenter, it undergoes smaller deformation than the as-assembled bubble before the first failure (from b to c in the right column of Figure 3.8) is observed, which also corresponds to a vertical crack. With continued loading, a second crack initiates and propagates in a vertical direction (perpendicular to the substrate) as indicated by the red arrow in Figure 3.8d right, which is strikingly different from the secondary horizontal cracks observed in the as-assembled bubbles. Both the first and second cracks in the calcined bubble initiate at a smaller deformation than the corresponding cracks in the as-assembled bubbles. Furthermore, subsequent cracks in the calcined bubble are all formed in the same way (red arrow in Figure 3.8e right) running vertically through the shell. The fractured pieces of the shell are expelled out of the field-of-view due to the large elastic energy accumulated in the broken shell, which is not the case for the plastically deforming as-assembled bubbles.

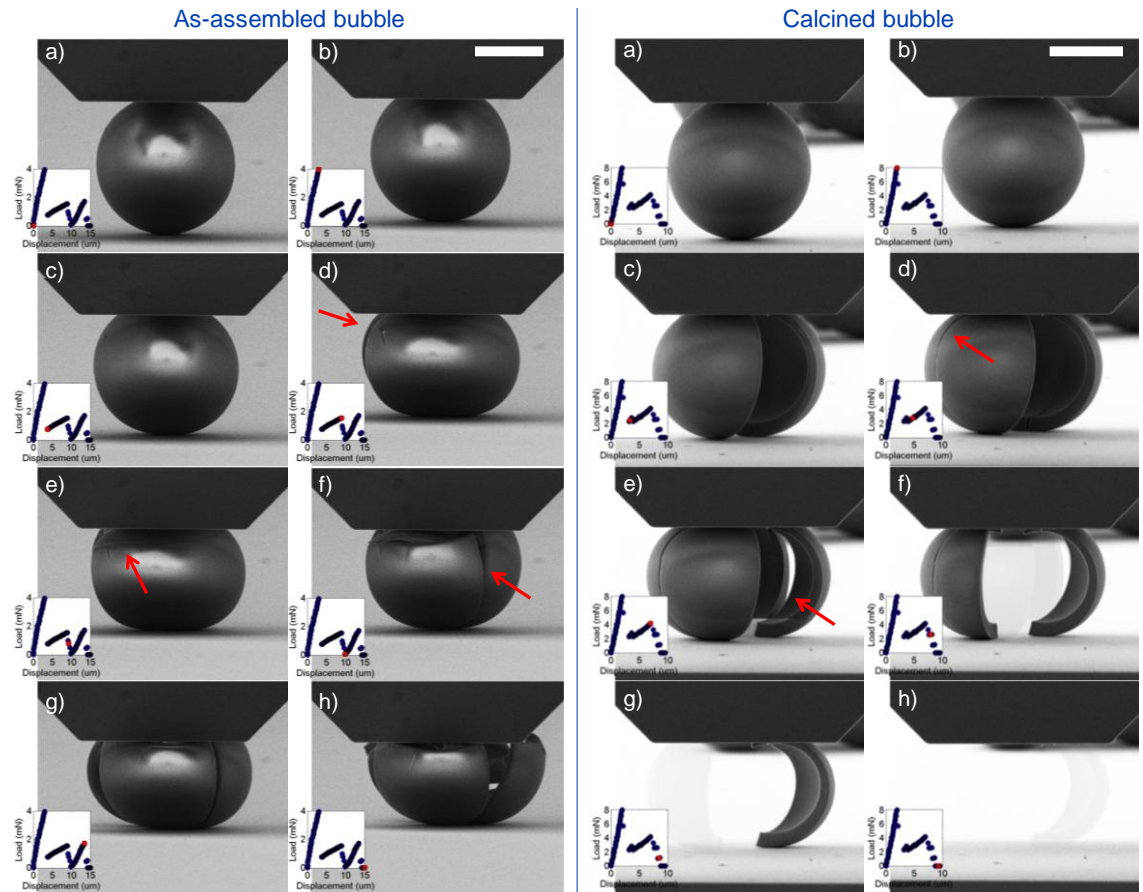


**Figure 3.8** Fracture mechanism of a characteristic as-assembled bubble (left) and calcined bubble (right) from quantitative *in situ* compression testing with flat punch; (a) to (h) different frames along the experiment. Scale bars 20  $\mu\text{m}$ . Inset graphs indicate the load-displacement at the specific time. Red arrows point at originated cracks.

The first failure event for both the as-assembled and the calcined bubbles occurs through the propagation of a vertical crack between the points of contact of the bubble shell with the plates. This result is consistent with the FEA results of Chapter 4 shown in Figure 4.4d, in which the maximum first principal stress is always observed beneath the indenter, and also with previous reports that studied the failure mechanism of elastic microballons.<sup>116-117</sup> However, the secondary cracking that develops after the first (vertical) fractures are strikingly different for the two types of bubbles. Understanding the

modes of subsequent failure (*i.e.*, vertical vs. horizontal secondary cracks) after the first cracks in these bubbles could be of importance in applications involving composites because once bubbles fail with horizontal cracks, their ability to bear compressive loads will be significantly compromised.<sup>118-119</sup> The load that the as-assembled bubble can bear after the formation of the second crack indeed decays to  $\sim 0$  as seen in Figure 3.8f left. In contrast, the fractured pieces of the calcined bubbles are able to withstand substantial load after the formation of multiple vertical cracks (Figure 3.8e-g right). Nevertheless, the fracture mechanisms of free-standing bubbles under compression may be different from the mechanisms of bubble failure in a composite material.

The quantitative load-displacement responses of the two types of bubbles obtained using *in situ* compression tests are consistent with the results from *ex situ* nanoindentation using the spherical indenter. As-assembled bubbles respond non-linearly (Figure 3.9a), whereas the response of calcined bubbles is nearly linear (Figure 3.9b). The breaks in the curves with significant load drops correspond to successive cracking events. The average failure loads, at the onset of the first cracking event of as-assembled and calcined bubbles are  $P_f = 3.9 \pm 0.7$  mN and  $9.9 \pm 1.4$  mN, respectively. The average failure deflections are  $\delta_f = 2.7 \pm 0.4$   $\mu\text{m}$  and  $2.0 \pm 0.2$   $\mu\text{m}$ , amounting to an 6.7 % and 5.3 % relative deflection ( $\delta_f/d$ ), respectively, indicating a larger deformability by the as-assembled bubbles compared to the calcined bubbles as one would expect. The average energies to failure of as-assembled and calcined bubbles are  $U_f = 5.5 \pm 0.9$  mN $\cdot\mu\text{m}$  and  $9.6 \pm 1.5$  mN $\cdot\mu\text{m}$ , respectively. The difference in the shape of the indenters in the two tests, sphero-conical for nanoindentation and flat for *in situ* tests, may have resulted in the

different values of energies to failure obtained from *in situ* and *ex situ* measurements. The results from *in situ* testing will be summarized and compared with *ex situ* results later.

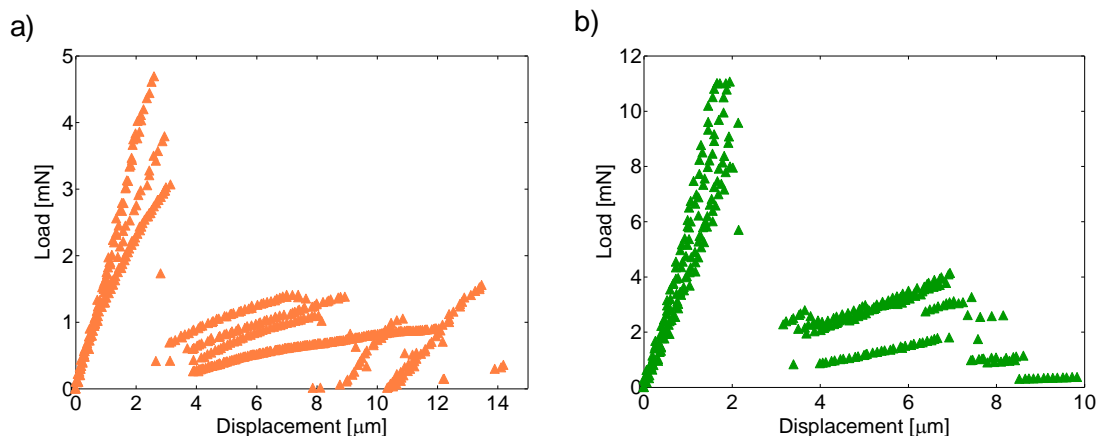


**Figure 3.9** Load-displacement curves of in-situ experiments. Curves corresponding to (a) four as-assembled bubbles, and (b) four calcined bubbles.

### 3.3.4 Summary of Mechanical Characterization

The results of mechanical characterization from the *ex situ* and *in situ* indentation tests are summarized for comparison in Figure 3.10. As seen in Figure 3.10a, the bubble outer diameter and the shell thickness decrease upon thermal treatment due to the removal of the organics (*i.e.*, PVA and the organic layer on nanoparticle surface) and the decrease in the shell porosity. The failure load significantly increases with the thermal treatment temperature (Figure 3.10b); that of the calcined bubbles is twice as large as that of the as-assembled ones, and the sintering process strengthens the bubbles by another order of magnitude. A similar trend is observed for the stiffness of the shelled-bubbles (Figure

3.10c). The measure of the stiffness can be extracted from the slope of the elastic regime in each load-displacement curve. While the calcined and sintered bubbles show linear responses, making it straightforward to obtain the slopes, the as-assembled bubbles show non-linear behavior, therefore we use linear regression between 0 and 500 nm deflection ( $R^2 \sim 0,997$  for *ex situ* nanoindentation, and  $R^2 \sim 0.957$  for *in situ* tests) to estimate their stiffness. Sintered bubbles present the largest stiffness, an order of magnitude larger than the as-assembled bubbles, followed by the calcined bubbles as shown in Figure 3.10c.

The energy to failure, *i.e.* fracture toughness, as well as the fracture strain, which correlate with the failure deflection (compression) of the bubbles in our experiments are important properties of the shelled-bubbles. Those properties, together with strength and the stiffness, will control the mechanical response and damage tolerance of the composites.<sup>8, 97, 118</sup> The average maximum deflection at failure normalized by the initial outer diameter of the bubble is plotted in Figure 3.10d for the different shelled-bubbles. As-assembled bubbles undergo a relatively large deflection at failure compared to calcined bubbles. Indeed, the presence of organics in the shell allows the as-assembled bubble to undergo relatively large inelastic (plastic) strains, and which increases the bubble ductility. Interestingly, deflection at failure increases when bubbles are treated at 1200 °C, likely due to the large strengthening effect of the fusion of silica nanoparticles and also the elimination of the small defects that porosity introduces in the calcined bubbles. Because of these factors, the energy to failure of the sintered bubbles is significantly greater than those of the as-assembled and calcined bubbles as seen in Figure 3.10e. Both the high deformability and high strength of the sintered bubbles

imparts an exceptional ability to absorb energy before undergoing fracture. A major difference in the behavior of the sintered bubbles and that of the as-assembled bubbles, of course, lies in the fact that the sintered bubbles are purely elastic, thus bubbles are able to fully recover their original shape, whereas as-assembled bubbles undergo plastic and thus irreversible deformation.

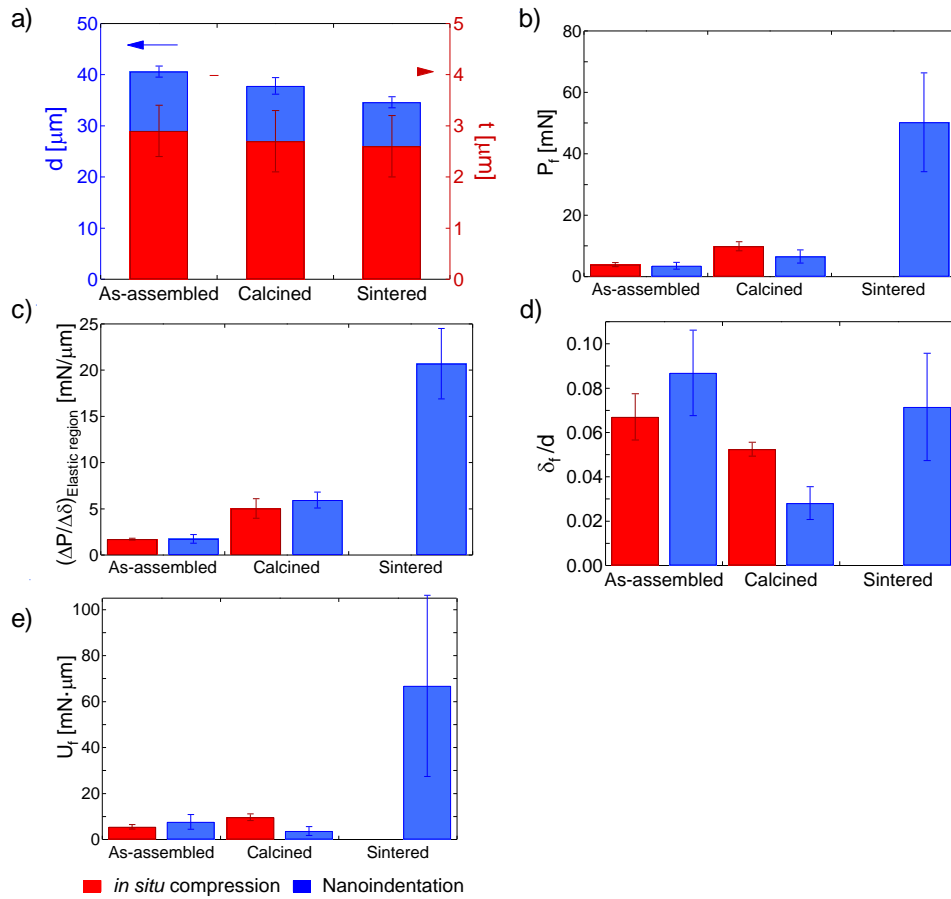


**Figure 3.10** (a) Diameter,  $d$ , and shell thickness,  $t$ , of as-assembled, calcined and sintered bubbles. (b) Average failure load of bubbles at fracture,  $P_f$ , as measured by the maximum load registered before the first crack. (c) Average stiffness of bubbles,  $\Delta P/\Delta\delta$ , computed from the slope of the load-displacement curves in the elastic regions. For as-assembled bubbles the elastic region is consider at small deflections of  $\delta < 500$  nm. (d) Average maximum deflection of bubbles,  $\delta_f/d$ , measured just before fracture, normalized by the initial diameter of the bubble. (e) Average energy to failure,  $U_f$ , computed from the area under the load-displacement curves before the first fracture.

### 3.3.5 Mechanical Response of Bubbles in Polymer-Bubble Composites

The results from the mechanical testing of individual bubbles presented above clearly show that thermal treatments have significant impact on the mechanical properties of nanoparticle-shelled bubbles. We expect these bubbles to behave very differently when they are incorporated into a polymer matrix. To illustrate the difference in the mechanical responses of the bubbles, we generate bubble-polymer composites using layer-by-layer (LbL) deposition. As shown in Figure 3.11a, bubbles are deposited on a silicon wafer using a process analogous to the Langmuir-Schaefer technique for nanoparticle printing.<sup>101</sup> Subsequently a solution of polystyrene is spin-coated on top of the dried layer of bubbles. Another layer of bubbles is deposited atop the polymer layer. This process is repeated to construct the LbL structure as shown in Figure 3.11b. A qualitative comparison of the response of the bubbles under a large mechanical stress can be made by cleaving the LbL structure atop the Si wafer. While a crack propagates through the bubbles in the composite with as-assembled bubbles (Figure 3.11c), the crack propagates around the bubbles in the sample with sintered bubbles (Figure 3.11d). This indicates that the weakest link in as-assembled bubble-polystyrene composite is the bubbles themselves, whereas that the weakest link in the sintered bubble-polystyrene composite is the bubble-matrix interface. The deformation mechanism of the bubble reinforced polymer composites are currently under investigation.



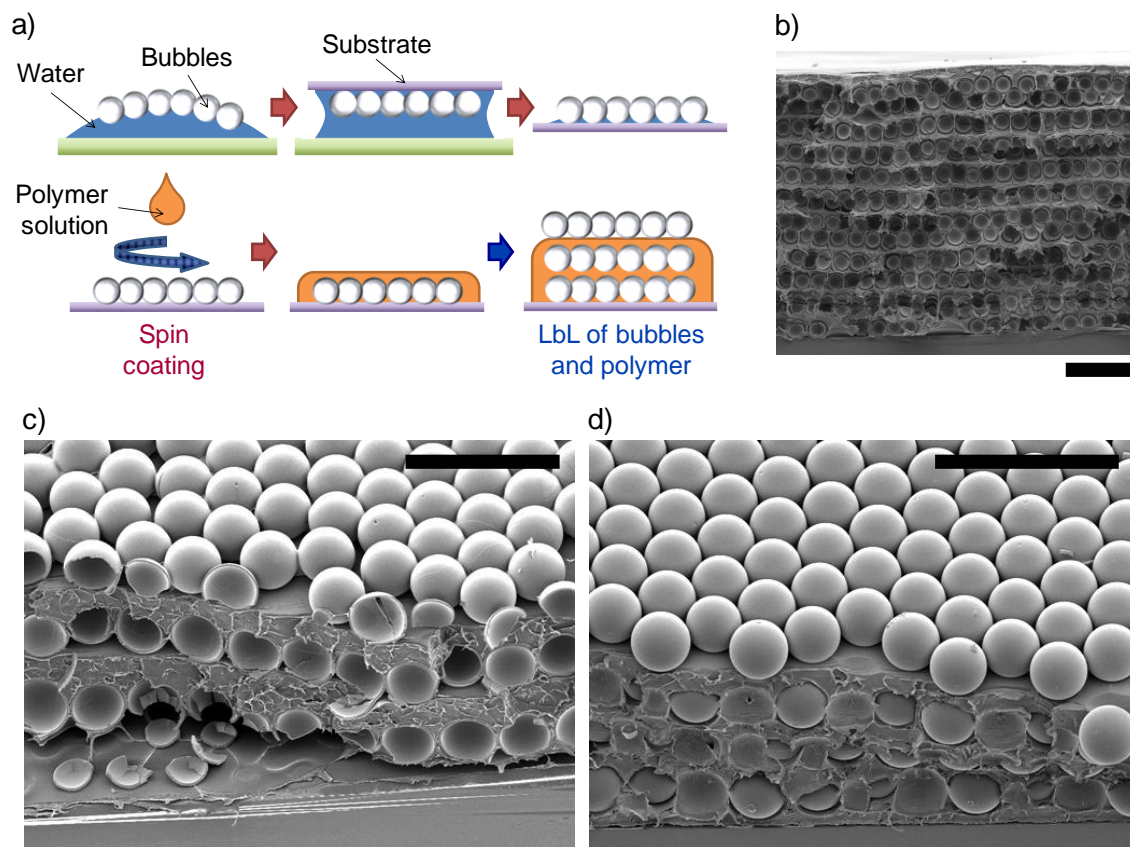


**Figure 3.11** (a) Layer-by-Layer (LbL) method used for the generation of polymer-bubble composites. (b) LbL structure composed of 10 bilayers for a total thickness of approximately 1 mm. (c) LbL structure made of as-assembled bubbles and polystyrene, and (d) LbL structure made of sintered bubbles and polystyrene. Scale bars = 200  $\mu\text{m}$ .

### 3.4 Conclusions

Here, we report the generation of mechanically tunable nanoparticle-shelled bubbles. Nanoparticle-shelled bubbles are generated using microfluidics, and their mechanical properties are tuned by calcination and sintering processes. Both *ex situ* and *in situ* mechanical testing show that the mechanical properties and deformation/failure modes of these bubbles depend considerably on the thermal treatment conditions. In fact, the

strength of the bubbles is increased by more than an order of magnitude upon sintering. As-assembled bubbles exhibit an inelastic response with significant plasticity afforded by the organic materials in the bubble shell. Interestingly, while the deformability of calcined bubbles is diminished due to the loss of organics, the deformability of sintered bubbles is close to that of as-assembled bubbles owing to the largely enhanced elastic range. The failure mode of the as-assembled and sintered bubbles in a polymer-bubble composite is shown to directly depend on the mechanical properties of individual bubbles. The tunable mechanical properties of nanoparticle-shelled bubbles make these hollow particles attractive candidates as fillers for the generation of light-weight materials that have different mechanical requirements. In addition to tuning the mechanical properties of bubbles and the composites containing these bubbles, the incorporation of various functional nanoparticles such as magnetic, semiconducting and plasmonic nanoparticles into the bubble shell will enable the formation of light-weight materials with specific functionality.<sup>120-124</sup>

# Chapter 4. Understanding the Mechanical Properties of Nanoparticle-Shelled Bubbles

Adapted from T. Brugarolas, D. S. Gianola, L. Zhang, G. M. Campbell, J. L. Bassani, G. Feng, and D. Lee. Tailoring and Understanding the Mechanical Properties of Nanoparticle-Shelled Bubbles, 2014, ACS Applied Materials & Interfaces DOI: 10.1021/am502290h. Copyright (2014) American Chemical Society.

## 4.1 Introduction

Chapter 3 presents the microfluidic generation of nanoparticle-shelled bubbles and their structural modification using thermal treatments, which changes their mechanical properties as well. It addresses in detail the mechanical characterization of these shelled bubbles: as-assembled, calcined at 700°C and sintered at 1200°C, using quantitative *ex situ* and *in situ* methods.

Chapter 4 compliments the work of Chapter 3 with finite element analysis (FEA) of the mechanical characterization of the shelled bubbles. FEA helps understanding the stress distribution along the shell during mechanical compression of single bubbles and their failure behavior, showing that the geometry as well as the inelasticity of the bubble shells can significantly affect their mechanical response. Computational simulations are also critical to elucidate the differences observed experimentally between as-assembled and calcined bubbles during the secondary cracking.

Both Chapter 3 and Chapter 4 contribute to the intellectual gap of measuring the physicochemical property of the bubbles, necessary to be addressed if those bubbles are intended to be used in practical applications.

## 4.2 Experimental Section

### 4.2.1 Finite Element Analysis

#### 4.2.1.1 Axisymmetric Problem

ANSYS 13.0 commercially available software is used for the simulation of the mechanical characterization of the single bubbles. Due to the spherical geometry of the shelled bubbles and the contact symmetry, axisymmetry is assumed and the simulations are performed in the two-dimension space using axisymmetric quadratic elements (PLANE183, higher order 2-D, 8-node or 6-node element). The mesh for a cross section of an axisymmetric bubble (see Figure 4.3d) comprises more than 5,000 elements and 15,000 nodes, with at least 16 elements radially spanning from the inner shell surface to the outer surface. The substrate is designed as a  $175 \times 175 \mu\text{m}^2$  elastic silicon block (Young's modulus,  $E = 162 \text{ GPa}$  and Poisson's ratio,  $\nu = 0.22$ ) which is large enough to have a negligible boundary effect on the modeling. For the simulations of the *ex situ* nanoindentation, a  $10 \mu\text{m}$ -radius spherical rigid tip is used for the simulation of the indenter. For the simulations of the *in situ* compression, a flat rigid tip is used for the simulation of the indenter. The contacts between the bubble and the indenter and the bubble and the substrate are assumed frictionless, and the element types used are TARGE169 and CONTA172. For boundary conditions, all lines in the axis  $y = 0$  are fixed in the  $x$  direction, and the boundary at the bottom of the substrate is fixed in both the  $x$  and the  $y$  directions. The application of the load is displacement controlled and was accomplished assigning the corresponding deflection conditions to a pilot node virtually

attached to the indenter geometry. Large deflections of the shell are accounted for in the analysis.

#### **4.2.1.2 Three Dimensional Problem**

Three dimensional analyses of hemispherical bubble shells are performed using ANSYS to understand the failure mechanism of the half shells formed after the first crack occurred under compression. Three dimensional analysis is needed due to the non-symmetry of a hemispherical shell under compression in the equatorial plane, for which axisymmetry is not suitable. To reduce the simulation time two planes of symmetry are applied to the three dimensional geometry. A first plane of symmetry can be drawn by dividing the half shell in two equal parts throughout the load axis, predicting a symmetrical deformation through that plane. A second plane of symmetry can be drawn dividing the hemispherical shell in half through the perpendicular plane to the load axis, assuming the indenter is equal to the substrate, being rigid and with frictionless contact with the half shell. Therefore the three dimensional analysis is performed in an eighth of a bubble shell where the inner area, the outer area and one edge are free surfaces. The simulations of the hemispherical shell under compression assume an ideal initial state in which there are not deformations and the initial state of stress is null.

The element used for the 3D simulations is SOLID187, a 10-node element that has a quadratic displacement behavior, well suited to modeling irregular meshes and with capability for large deflections and strains. The mesh has more than 30000 nodes and 19000 elements, with at least 4 elements radially spanning from the inner shell surface to the outer surface. The indenter is assumed rigid and the contact with the half bubble shell

is assumed frictionless. The element types used for the contact between indenter and substrate are TARGE170 and CONTA174. For boundary conditions, in addition to the symmetries applied, the top node of the shell is restricted in lateral directions (x and y) to avoid sliding of the shell during the simulation. The application of the load is displacement controlled and was accomplished assigning the corresponding failure displacement conditions to a pilot node virtually attached to the indenter geometry. The analysis used is non-linear and allows for large deformations. Spherical coordinates are used for the extraction of the stress and strain components for a better understanding on the distribution of stresses and strains, and possible failure causes.

The hemispherical calcined bubble shell is modeled as a perfect elastic material with two different Young's Moduli of 13.7 GPa and 20GPa, and Poisson ratio of 0.18. The hemispherical as-assembled bubble shell is modeled as a von Mises elastic-perfectly plastic material with Young's Modulus of 6.9 GPa, yield stress of 0.12 GPa, and Poisson ratio of 0.18. The geometric parameters, diameter and thickness, are defined to represent the average values experimentally measured and defined in Table 4.2 for uniform shells.

A Drucker-Prager material model is further used for the simulation of an as-assembled hemispherical shell. In this case, the element type used is SOLID65, a brick like element defined by eight nodes having three degrees of freedom at each node: translations in the nodal x, y, and z directions. A total of approximately 26,000 elements are used for this simulation. An associated flow rule in conjunction with the Drucker-Prager yield function is adopted, which mean that the yield and flow functions are identical.

#### 4.2.2 Nanoparticle Film Generation and Characterization

For the generation of nanoparticle films, hydrophobic SiO<sub>2</sub> nanoparticles (Nissan Chemical Industries, Ltd.) in toluene, at an approximate concentration of 14 wt%, are deposited on a Si wafer (approximated size of 1.5 x 1.5 cm<sup>2</sup>) by spin coating using a WS-400BZ-6NPP/Lite spin coater from Laurell Technologies Corp, at a rotation speed of 2000 rpm for 2 minutes. Prior to spin coating, silicon wafers are treated with octadecyltrichloro-silane (OTS), which renders the substrates hydrophobic. To generate crack-free films that are thick enough for reliable nanoindentation, multideposition of nanoparticles is performed following a method previously reported.<sup>125</sup> An intermediate step of dipping the film in DI water for a few minutes is necessary to allow for a better build-up of films during the multicoating steps. Three depositions are used to build a crack-free film of 450 nm in thickness. To facilitate a homogeneous build-up of crack-free films for calcined and sintered cases, the multideposition by spin coating (3000 rpm for 2 min) on OTS treated quartz slides (approximated size of 1.5 x 1.5 cm<sup>2</sup>) is alternated with 2 hour calcination steps at 700 °C, which results in uniform films (the thickness growth is shown in Figure 4.1). Five depositions are performed to obtain calcined films of 710 nm, and these films are sintered at 1200 °C to obtain sintered films of 500 nm. The verification of obtaining crack-free films is done by optical microscopy and SEM imaging. Film thickness and porosity of the films is determined using a J.A. Woolam  $\alpha$ -Spectroscopic Ellipsometer (SE) with a fixed incidence angle of 70°.<sup>126</sup>

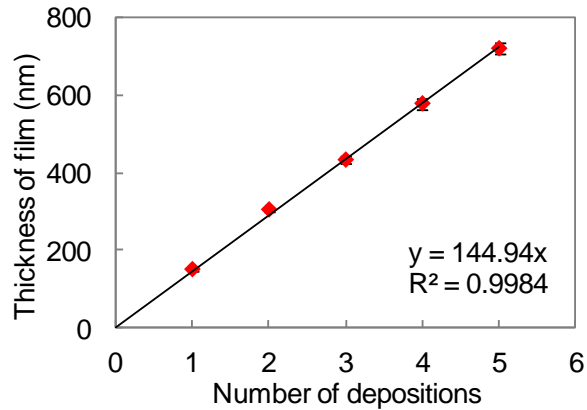


**Figure 4.1** Film thickness growth with number of deposition of particles by spin coating with subsequent calcinations steps between each deposition. The growth rate is 145nm per deposition. Values in graph are averaged from eight samples, and error bars correspond to standard deviation.

The mechanical properties including Young's modulus and hardness of the as-assembled, calcined and sintered films are obtained using nanoindentation performed using a Nano Indenter™ G200 from Agilent™ Technologies Inc. with continuous stiffness measurement using a Berkovich indenter tip following similar methods previously reported.<sup>127-128</sup> The indenter tip area function is calibrated using fused silica, and a constant Young's modulus is achieved in the depth range of 40-100 nm. The indenter is stabilized to achieve a thermal drift rate less than 0.05 nm/s before performing any indentation. The indentation depths of the as-assembled, calcined and sintered films are 200, 300, and 200 nm respectively, with a constant loading strain rate of 0.04s<sup>-1</sup>. The characterization of the plasticity of as-assembled film and the determination of its yield strength is performed by measuring the hardness of the film using Berkovich and cube corner indenter tips following a previously reported method.<sup>129-130</sup> The properties of the nanoparticle films are detailed in Table 4.1.



**Table 4.1** Properties of nanoparticle films

	Thickness of film (nm)	Porosity of film (%)	Young's modulus (GPa)	Yield strength (GPa)
As-assembled film on silicon wafer	453 ± 7 (by ellipsometry)	N/A	6.9 ± 0.9	0.12 ± 0.02
Calcined film on quartz slide	709 ± 6 (by ellipsometry)	31 ± 2	13.7 ± 0.2	N/A
Sintered film on quartz slide	500 ± 30 (by SEM)	0.0 ± 0.4	76 ± 3	N/A

The mechanical characterization of as-assembled films suggests an elastic-perfectly plastic behavior, *i.e.* a material that does not harden beyond the yield point. Calcined and sintered films, in contrast, suggest an ideally elastic behavior. Young's moduli and yield strengths are included in Table 4.1.

## 4.3 Results and Discussion

### 4.3.1 Finite Element Analysis of Bubble Nanoindentation Prior to Fracture

The mechanical response of the nanoparticle-shelled bubbles depends significantly on thermal treatment, as illustrated by the nanoindentation experiments (see Figure 3.6). Notably, the sintered bubbles are stiffer, *i.e.*, support higher loads at the same depth of indentation, (and stronger) than the calcined bubbles which are stiffer than the as-assembled bubbles as seen in Figure 3.6. Comparing the load-deflection curves, we see that the as-assembled bubbles display an inelastic behavior. We also observe some variation in the mechanical response of bubbles with the same thermal treatment as seen in each panel of Figure 3.6.

To quantify how the mechanical properties of the nanoparticle-shelled bubbles depend on thermal treatments and to explore what accounts for variations in the mechanical response of bubbles with the same nominal size and thermal treatment, we perform finite element analyses (FEA) of the bubbles under nanoindentation.<sup>116</sup> The FEA requires the inputs of the mechanical properties (elastic moduli and yield strength) of the bubbles. The mechanical properties of the modeled bubble shells are estimated by nanoindentation testing on SiO<sub>2</sub> nanoparticle films prepared on planar silicon or quartz substrates subjected to the same thermal treatments as the bubbles. Details on the formation of nanoparticle films and their characterization are provided in the experimental section 4.2.2. The nanoindentation results of as-prepared nanoparticle films suggest that the as-assembled bubble shell behaves approximately as an elastic-perfectly-plastic material, *i.e.*, no hardening beyond yielding. Isotropic von Mises yielding criterion is assumed in FEA modeling, in which case the plastic strains are incompressible. As indicated by the nanoindentation results, calcined and sintered films are modeled ideally elastic. The outer diameter, shell modulus and thickness of bubbles are adjusted to reflect the experimental values and are given in Table 4.2. Also, as will be discussed later in more detail, to study the effect of shell-thickness non-uniformity of each individual bubble, both uniform and non-uniform shells are simulated (see Table 4.2). The finite element results presented below account for large axisymmetric deflections of the shell under nanoindentation loading.

**Table 4.2** FEA parameters of simulated as-assembled, calcined and sintered bubbles

	Shell Modulus,* $E$ [GPa]	Shell geometry	Outer diameter, $d$ [ $\mu\text{m}$ ]	Shell thickness, $t$ [ $\mu\text{m}$ ]
As-assembled bubble	6.9	Uniform	40.6	2.9
		Non-uniform	40.6	2.4 (thin), 3.4 (thick)
Calcined bubble	13.7	Uniform	37.8	2.7
		Non-uniform	37.8	2.1 (thin), 3.3 (thick)
Sintered bubble	76	Uniform	34.6	2.6
		Non-uniform	34.6	2 (thin), 3.2 (thick)

\* The elastic moduli are measured on nanoparticle films on planar substrates as explained above

The experimental and the FEA-simulated load-displacement curves are shown in Figure 4.3a-c for each bubble type. For the as-assembled bubbles, two sets of FE simulations were conducted based on pure elasticity and elastic-perfect-plasticity, respectively. Figure 4.3a shows that compared to the experimental results (shaded region), the purely elastic FEA displays linear load-displacement behavior and overestimates the load and stiffness of the bubbles for indentations greater than about 1  $\mu\text{m}$ . However, the elastic-perfectly-plastic model with a uniaxial yield stress  $\sigma_y = 118$  MPa gives a less stiff response and matches the nanoindentation experiments. These results, in contrast to nanoindentation of the calcined and sintered bubbles (see Figure 4.3b and c), indicate that the as-assembled bubbles likely undergo plastic deformation during indentation, accounting for the observed non-linear deformation. The apparent plastic deformation, we believe, is due to the rearrangement of randomly packed silica nanoparticles within the as-assembled bubble shell under load. Such rearrangement

occurs through frictional sliding and causes irreversible deformation, which results in the plasticity of the as-assembled bubbles.<sup>119</sup>

The FEA results of indentation on elastic sintered bubbles with a Young's modulus of  $E = 76$  GPa (Figure 4.3c) display a linear load-displacement response with excellent agreement with the experimental results (shaded area in Figure 4.3c). The simulation results for the elastic calcined bubbles (Figure 4.3b) with a Young's modulus of  $E = 13.7$  GPa also predict the linearity of the response; however, these load-displacement curves lie below the experimental curves. By using a slightly higher modulus of  $E = 20$  GPa for the bubble shell, the FEA prediction agrees better with the experimental results, indicating that the Young's modulus obtained by characterizing a calcined nanoparticle film on a planar substrate underestimates the stiffness of the calcined bubble shell. Such discrepancy may be attributed to the difference in the boundary conditions/confinements; nanoparticle films are bound to a substrate, whereas bubble shells are free standing films of nanoparticle packings.<sup>131</sup>

We hypothesize that variations observed in the load-displacement curves for each bubble type, as seen in Figure 3.6, can be attributed to the non-uniformity in the thickness of the shell for each bubble and cannot be explained solely by small variations of the bubble diameter or the material properties of the shell. FEA results for uniform shells with different outer diameters (and different Young's moduli) are shown in Figure 4.2a (and Figure 4.2b). The variation in the diameters and the elastic moduli represents the standard deviation measured experimentally. The change in diameter and the material properties of the shells does not significantly affect the mechanical response of the shells

and cannot predict the observed experimental results (shaded region). Similarly, FEA results for uniform shells with different thicknesses are shown in Figure 4.2c. The variation in the thickness of the shell represents the standard deviation of the thickness measured experimentally with the assumption that all bubble shells are uniform. Uniformity in the shell thickness is unlikely according to what has been observed experimentally (see for example Figure 3.8 right column). The assumption of uniformity in shell thicknesses predicts large differences on the mechanical responses that solely do not explain the observed experimental results.

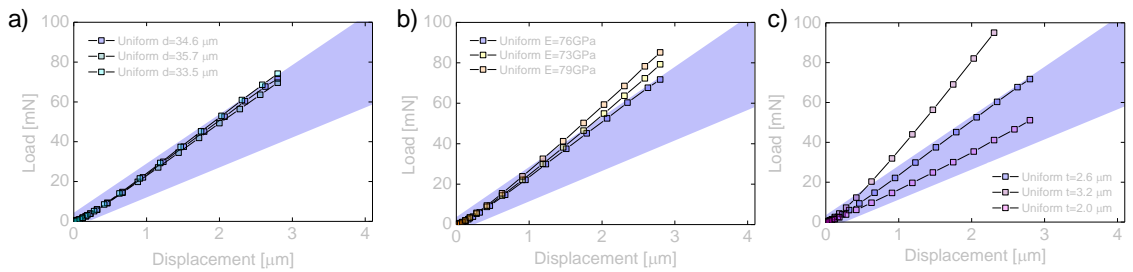


**Figure 4.2** Load-displacement simulation results of sintered bubbles. (a) Different outer diameters with constant  $t=2.6\ \mu\text{m}$  and  $E=76\ \text{GPa}$ , (b), (b) different Young's moduli with constant  $d=34.6\ \mu\text{m}$  and  $t=2.6\ \mu\text{m}$ , and (c) different thicknesses with constant  $d=34.6\ \mu\text{m}$  and  $E=76\ \text{GPa}$ . The deviation of each parameter represents the standard deviation measured experimentally.

In fact, recent reports have shown that non-uniformity in the shell thickness of vesicles can drastically change their deformation behaviors under hydrostatic pressure.<sup>132-</sup>

<sup>133</sup> Also, Carlisle *et al.* investigated the failure mechanisms of carbon “microballoons” (linear elastic brittle materials) with finite element modeling, predicting a change in failure mode depending on the non-uniformity of the shell.<sup>116</sup> SEM observation of broken bubbles shows that the bubble shell thickness does vary for each bubble (see for example,

Figure 3.8 right column), most likely due to the buoyancy of the gaseous core during solvent evaporation from the middle phase (oil) of the G/O/W compound bubbles. The effect of shell thickness variation is approximated in the finite element simulations by off-setting the two centers of two spherical surfaces that define the shells, incorporating a thin section at the top or at the bottom of the bubble. The thinnest and thickest sections of the bubble shell reflect the standard deviation of the shell thickness summarized in Table 4.2.

Load-displacement curves for the non-uniform shells are extracted from the FEA simulations and compared with the experimental results. Figure 4.3a-c show the simulated load-displacement curves for bubbles with uniform and non-uniform shells for each bubble type. It is interesting to note that for all bubble types, the stiffness for the non-uniform geometries is predicted to be less than the stiffness of a uniform bubble with a wall thickness equal to the average thickness of the non-uniform ones. Bubbles that are thinnest under the indenter display the least stiff response. That is, at a given depth of indentation, the load required for non-uniform shells is always smaller than that of uniform shells with comparable wall thickness. Shell thickness non-uniformity also results in greater stress concentrations (see Figure 4.3d and the discussion below), which likely causes fracture to occur in the non-uniform bubbles at smaller indentation depths compared to failure of the uniform bubbles.

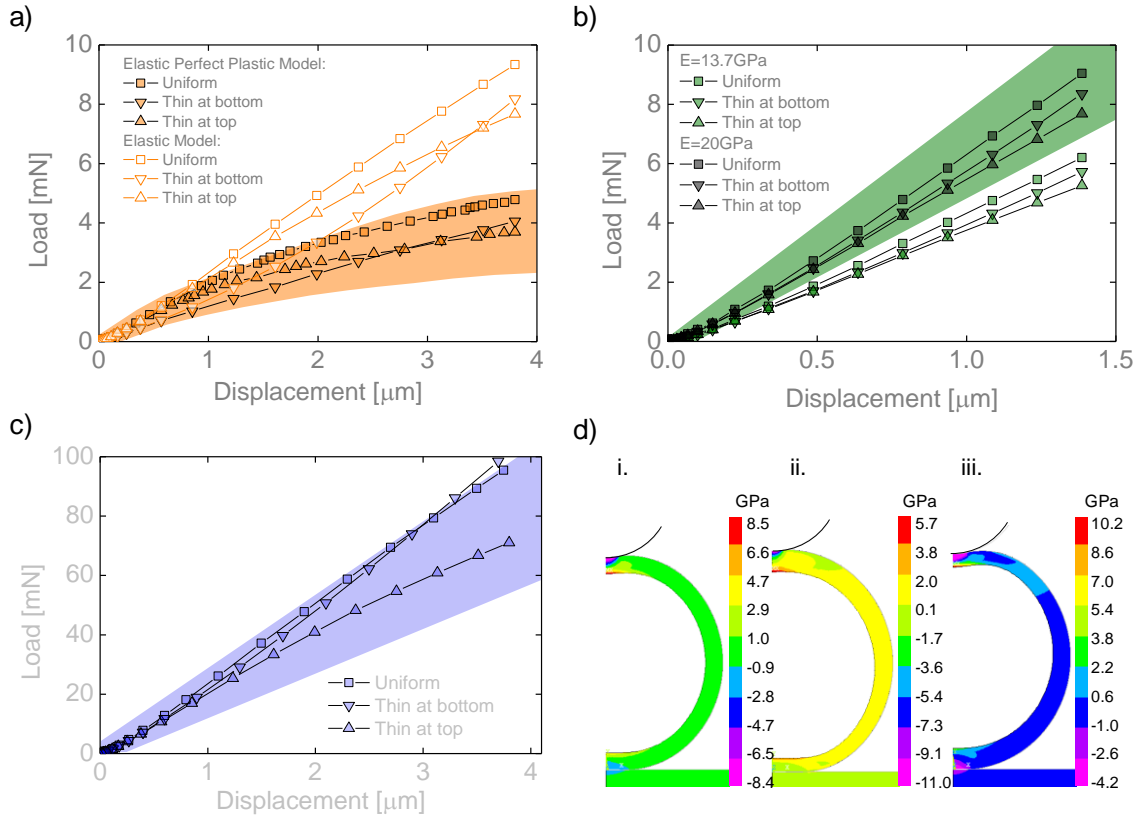


**Figure 4.3** (a), (b) and (c) are load-displacement curves simulated using FEA for as-assembled, calcined and sintered bubbles, respectively, with comparisons to the experimental results (shaded regions). (d) Contour plots from FEA showing first principal stress of a sintered bubble under a spherical indenter at an indentation depth, in each case, corresponding to the average of the first fracture observed in the experimental nanoindentation *ex situ* tests. Figures i, ii, and iii, represent different shell geometries (uniform, thin at bottom, and thin at top) indicating the differences in the first principal stress distribution along the shell at the maximum indentation depth predicted from the FEA.

The distributions of stresses and strains observed in the FE simulations can provide insight into failure mechanisms. For example, for the sintered bubble, principal stress distributions are plotted in Figure 4.3d at indentation depths, for each case, that correspond to the average of the first observable fractures. In each case, the maximum principal stress occurs at the inner surface of the shell beneath the initial point of contact

with the spherical indenter, regardless of the shell geometry (uniform vs. non-uniform thickness). At that location, the maximum principal stress corresponds to a circumferential stress component with respect to the axis of symmetry. That stress would cause a (brittle) crack to initiate along a meridian. The magnitude of the principal stress as well as the stress distribution at the average displacement that causes fracture for each bubble, however, varies noticeably depending on the shell geometry. The magnitude of the maximum principal tensile stresses varies from  $\sigma_1 = 8.5, 5.7$  and  $10.2$  GPa, for the shell with uniform thickness, the shell that is thin at the bottom, and the shell that is thin at the top, respectively (Figure 4.3d). These differences in the magnitude of the maximum principal stresses suggest that fracture would occur at different loads for different geometries. For the different bubble types, as-assembled, calcined and sintered, the magnitude of the maximum principal stress at the average failure deflection for uniform shells are  $\sigma_1 = 135$  MPa,  $528$  MPa (for  $E=13.7$ GPa;  $769$  MPa for  $E=20$ GPa) and  $8.5$  GPa, respectively, which is an indicative of the critical fracture strength of the shell materials.

## **4.3.2 Finite Element Analyses of *In situ* Experiments to Failure**

### **4.3.2.1 Load-Displacement Prediction**

*In situ* experiments presented in Section 3.3.3 complement the mechanical analysis done with nanoindentation. Using FEA, we predict the overall load-displacement curves of the *in situ* experiments to failure of both the as-assembled and calcined bubbles as shown in



Figure 4.4a and b. The load-displacement behavior is predicted for the full bubble under flat plate indentation (axisymmetric) showing consistency with the experimental results. As in the previous FEA, the as-assembled bubbles are modeled as an elastic-perfectly-plastic von Mises material. The calcined bubbles are modeled as ideally elastic, once again using two different Young's moduli of  $E = 13.7$  GPa and 20 GPa (Figure 4.4b). Both simulation results agree well within the range of experimental tests. Although we cannot perform *in situ* testing on sintered bubbles because they are too stiff and strong for our *in situ* indentation system, we are able to predict their response using FEA with a Young's modulus of  $E = 76$  GPa as shown in Figure 4.4c, demonstrating the utility of our computational approach to understand the mechanical response of these small hollow structures.

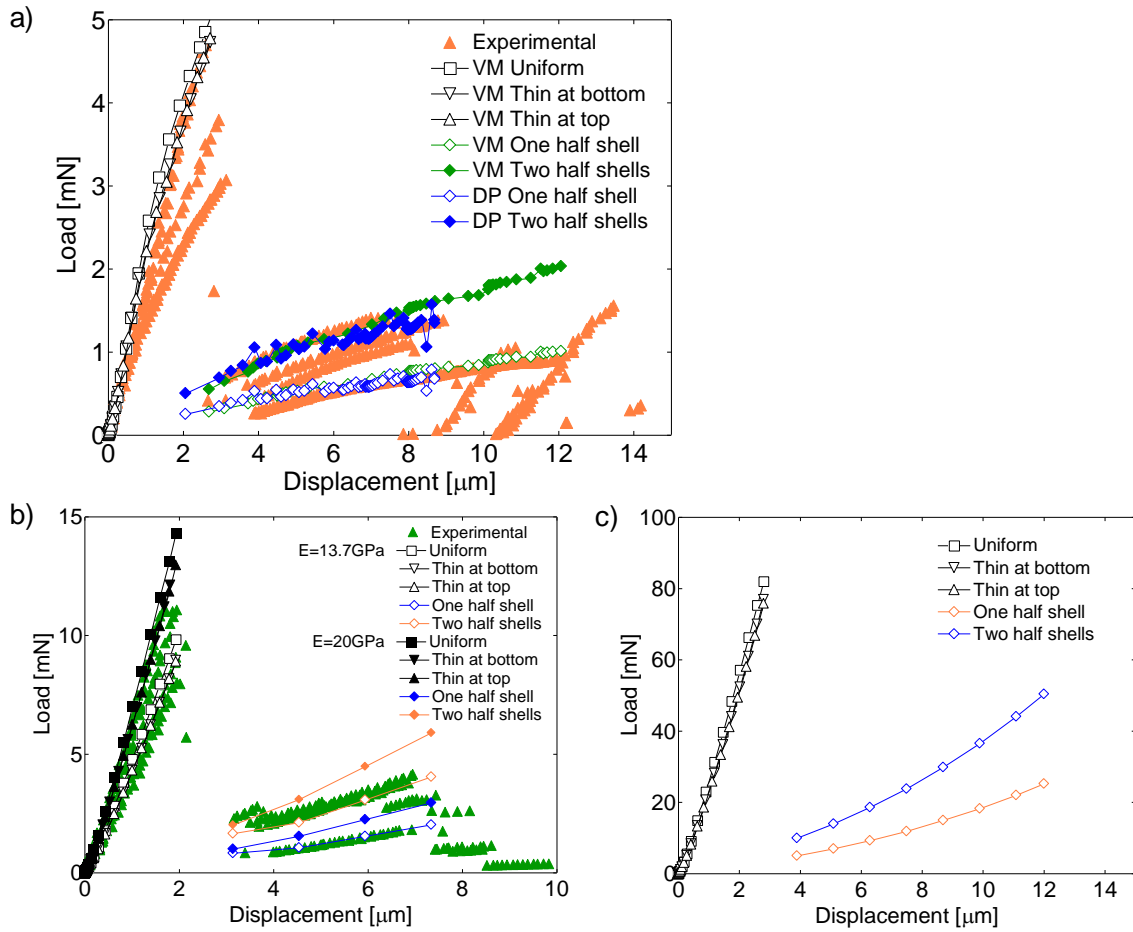


**Figure 4.4** Load-displacement curves of *in situ* compression of (a) four as-assembled bubbles, and (b) four calcined bubbles, including both the first failure event as well as the secondary cracking events that occur on loaded remnants of the fracture shells. FEA results for the first failure event are included in the graphs for three different shell geometries (uniform shell, thin at top, and thin at bottom). FEA results for secondary cracks for uniform shells are also plotted including the responses when one or two halves of the shell remain under load between the indenter and the substrate. (c) Simulation results for the failure prediction of a sintered bubble lacking of experimental values. As-assembled bubbles (a) are simulated with elastic perfectly plastic von Mises (VM) and Drucker-Prager (DP) models. Calcined bubbles (b), and sintered (c) are simulated with an elastic model.

#### 4.3.2.2 Finite Element Analysis of Secondary Cracking

To better understand the nature of secondary cracking and the load-displacement response of fractured bubbles under compression, we carry out a series of FE calculations of the half shell that arise after the first fracture. The load-displacement predictions for the secondary cracking depend on whether the two half shells remain in full contact with the indenter or only one of the two half shells are under load after the first fracture event (*i.e.*, when the fractured pieces of the shell are expelled out of the field-of-view due to the large elastic energy accumulated in the broken shell, or when a piece loses contact between the flats during the further compression). In the case of the calcined half shell, the computed first principal stress distribution is maximum under the indenter (see Figure 4.5), and that corresponds to a circumferential normal stress component which is consistent with the vertical secondary cracks in the *in situ* tests. Consequently, we believe that the mechanism of cracking in the calcined bubbles is reasonably well understood.

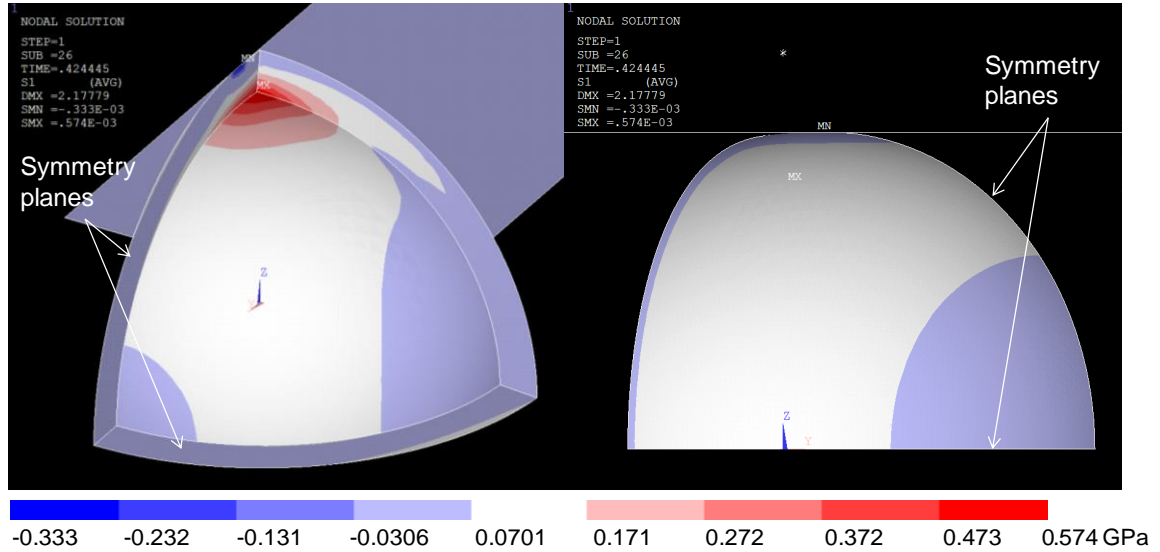


**Figure 4.5** Three dimensional FEA of calcined half shell modeled as a perfect elastic material. The maximum first principal stress is concentrated beneath the indenter presumably causing the secondary vertical cracks. The magnitude of the maximum principal stress at failure deflection (0.574 GPa) is consistent with the stress observed during first crack (0.617GPa) from the two dimensional FEA.

The mechanism that leads to the formation of horizontal cracks in the half shells of as-assembled bubbles is a more challenging problem. The role of plasticity in redistributing the stress in as-assembled bubbles during compression may provide insight. We carry out a series of FE simulations on a hemispherical as-assembled shell. The first set of calculations is based on the von Mises elastic-perfectly plastic material model. Although those results can reasonably predict the overall load-displacement curves (see Figure 4.4a), they do not display definitive trends with respect to distributions of stress and strain components throughout the bubble that can explain the horizontal cracking. At levels of indentation that are consistent with the initiation of the horizontal crack, results from the FE calculations for the von Mises material model are studied in detail. For example, we compute and plot the components of strain in spherical coordinates to

investigate if a concentration in the component of strain acting perpendicular to the incipient horizontal fracture surface exists. We also monitor stress components including the von Mises effective stress (see Figure 4.6a) and the hydrostatic pressure (Figure 4.7a) as well as the effective plastic strain (Figure 4.8a). None of those measures can explain the initiation of a horizontal crack in the as-assembled bubble on a surface that is roughly one-half a bubble radius below the indenter. A few points about the von Mises plasticity model are warranted at this point. The von Mises yield criterion and its associated flow rule are independent of hydrostatic pressure, which is a good approximation for a fully dense, typically crystalline material. On the other hand, the as-assembled nanoparticle shelled bubbles likely display significant pressure sensitivity in yielding and plastic flow due to sliding between the nanoparticles.

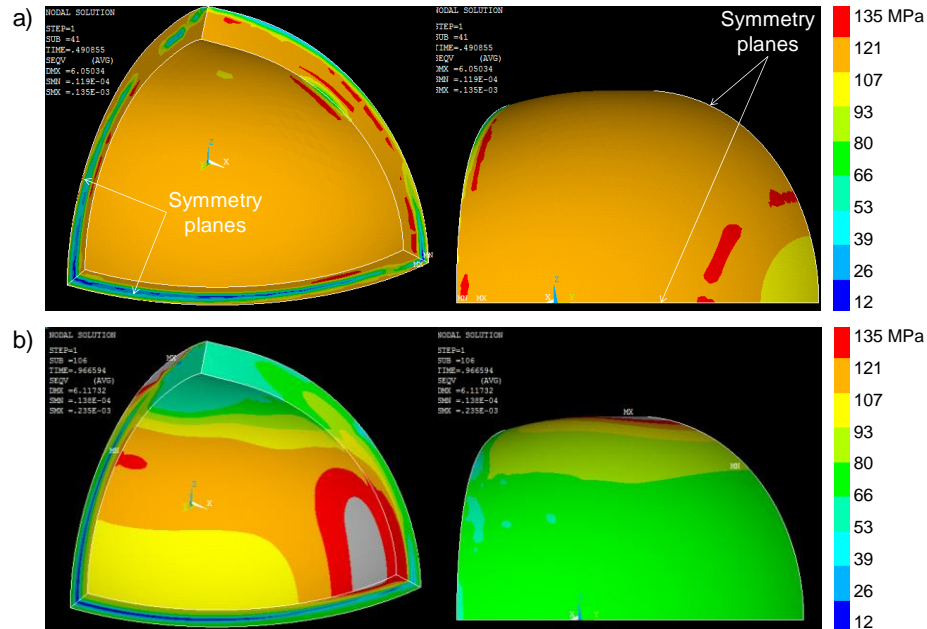


**Figure 4.6** Von Mises stress in the inner and outer surfaces of a hemispherical as-assembled bubble shell. The hemispherical as-assembled shell is modeled using a von Mises material model (a), and a Drucker-Prager material model (b).

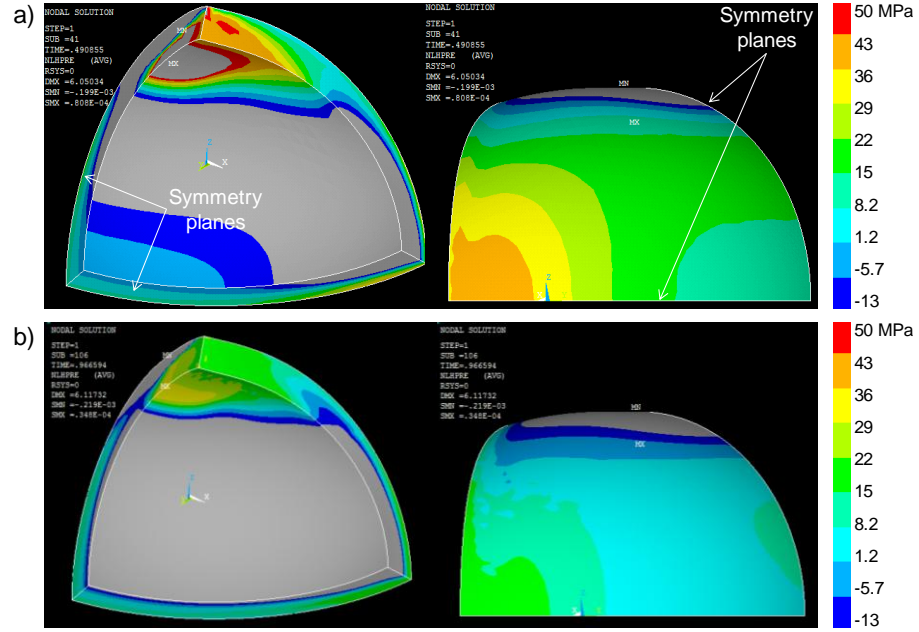


**Figure 4.7** Mean stress in the inner and outer surfaces of a hemispherical as-assembled bubble shell. The hemispherical as-assembled shell is modeled using (a) the von Mises material model and (b) the Drucker-Prager material model.

A classical model, originally developed for granular materials and soils, is the Drucker-Prager yield criterion,<sup>134</sup> which adds a pressure dependent term to the von Mises effective stress. Furthermore, the associated plastic flow rule for the von Mises model is incompressible whereas the Drucker-Prager model includes plastic dilation. The Drucker-Prager yield criterion can be expressed as:<sup>135</sup>

$$\sigma_{VM} + 3\beta\sigma_m = \sigma_Y \quad 4.1$$

where  $\sigma_{VM}$  is the pressure-independent von Mises effective stress ( $\sigma_{VM}^2 = \frac{3}{2}s_{ij}s_{ij}$ , where  $s_{ij} = \sigma_{ij} - \frac{1}{3}\sigma_{kk}\delta_{ij}$  is the deviatoric stress), and  $\sigma_m = \frac{1}{3}\sigma_{kk}$  is the mean stress. The material parameters entering the Drucker-Prager criterion are the pressure sensitivity  $\beta$

and  $\sigma_Y$ . Note that the yield stress in uniaxial tension is  $\sigma_T = \sigma_Y / (1 + \beta)$  and the yield stress in uniaxial compression is  $\sigma_C = \sigma_Y / (1 - \beta)$ . For granular (frictional) materials, typically  $\sigma_C > \sigma_T$ , which implies  $\beta > 0$ . Based upon the overall load-displacement curves for the half shells of as-assembled bubbles, *i.e.* after the first cracking event, the parameters chosen for the Drucker-Prager material are  $\beta = 0.29$  and  $\sigma_Y = 83.6$  MPa. Those parameters correspond to a compressive yield stress  $\sigma_C = 118$  MPa, which agrees with the yield stress used for the von Mises model, and to a ratio of the compressive and tensile yield stress  $\sigma_C / \sigma_T = 1.82$  (also, the friction angle which is commonly used to characterize pressure sensitivity is  $22^\circ$ ). An associated flow rule is adopted,<sup>136</sup> which leads to plastic dilatancy.

The overall load-displacement curves calculated using the Drucker-Prager model are similar to those predicted using the von Mises model (see Figure 4.4a DP vs. VM curves), and both are in good agreement with experiments. Nevertheless, the predicted distributions of stresses and strains display considerable differences as one might expect due to the difference in incompressible and dilatant plastic flow. We investigate and compare various components of stresses and strains and find some significant differences. Comparisons of the effective plastic strains for each model are plotted in Figure 4.8 for half as-assembled bubbles compressed up to a deflection of  $9 \mu\text{m}$ , which approximately corresponds to the initiation of the horizontal crack, averaged for the 4 specimens from the *in situ* tests. Given that the deformations on the outer surface of the shell are predominately tensile, while they are predominately compressive on the inner surface, we

expect the secondary cracking to initiate on the outer surface. As seen in Figure 4.8a for the von Mises material, the magnitude of the effective plastic strain on the outer surface is less than 0.016 except right under the indenter, while the effective strain for the Drucker-Prager material (Figure 4.8b) reaches a significantly higher level, up to 0.037 in a region near the mid-meridian plane of the half shell at a latitude near where horizontal cracks are observed to form. Those differences, which occur at approximately the same overall load levels (see Figure 4.4a) are significant and indirectly lead to the conclusion that pressure-sensitive yielding is characteristic of the as-assembled bubbles, as one would expect. Nevertheless, further detailed studies beyond the scope of these analyses are required, keeping in mind that the Drucker-Prager model is a simple extension of the von Mises model to include pressure sensitivity and plastic dilation. We also note that as-assembled bubbles also likely display rate-dependent mechanical behavior due to the presence of organic materials, which could affect the deformation and failure mechanisms under different loading conditions (*i.e.*, strain rate, stress relaxation).<sup>119</sup>



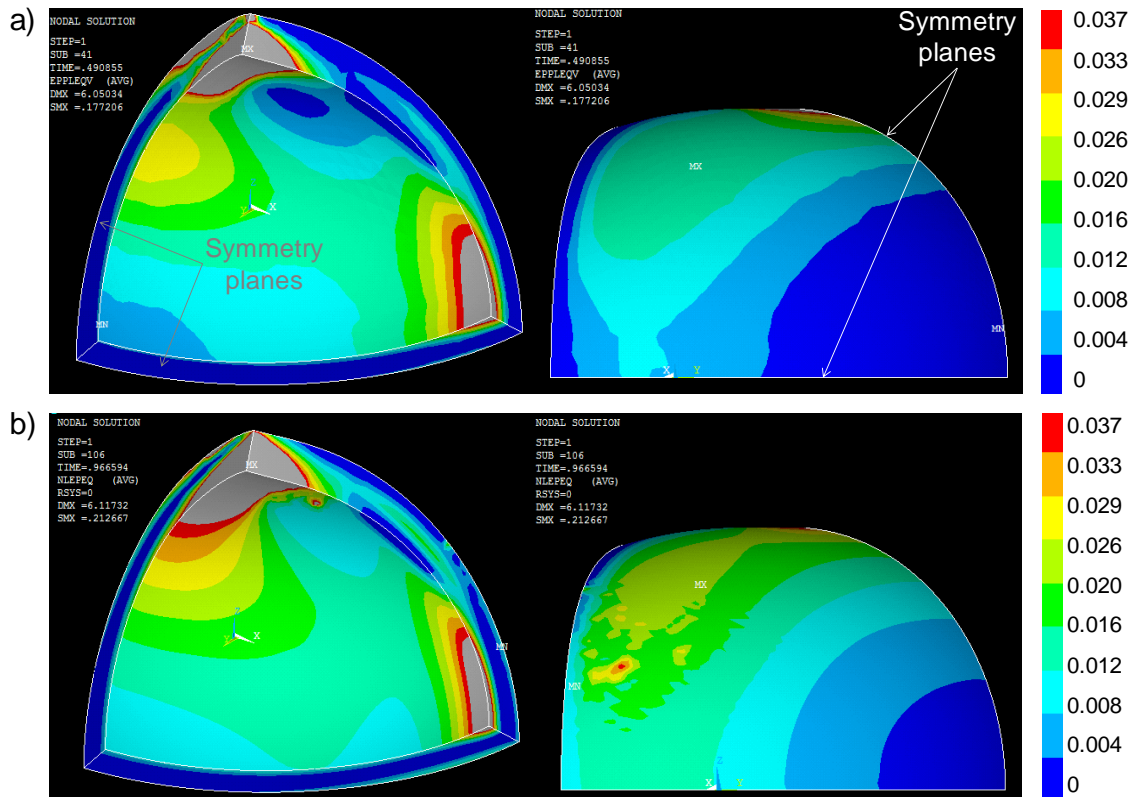


**Figure 4.8** Finite element simulation of half as-assembled bubble modeled as a von Mises material (a), and a Drucker-Prager material (b). In each case, the appropriate effective plastic strain is plotted over the inner and outer surfaces. Note the elevation of plastic strain near the mid-meridian plane for the Drucker-Prager material.

## 4.4 Conclusions

The simulation work presented in this chapter complements the experimental work of Chapter 3. Finite element analysis is carried out to elucidate the differences in the observed mechanical response compression of the as-assembled, calcined and sintered nanoparticle-shelled bubbles.

The simulation of the nanoindentation tests agrees well with the experimental results, indicating that the as-assembled bubbles can be modeled as elastic-perfectly plastic materials predicting the inelastic behavior of their response. Calcined and sintered can be modeled as perfect elastic materials showing a good agreement with the nanoindentation results. We find that the shell geometry has a significant impact on the response of these bubbles under load, and the non-uniformity of the shell can be responsible of the variations observed in the nanoindentation load-displacement curves for each bubble type.

In addition, we use FEA to confirm the *in situ* compression tests, extracting the overall load-displacement curves. Using the same material models used for the simulation of the nanoindentation results, the load-displacement curves of the *in situ* compression can also be predicted. The utility of our computational approach is demonstrated with our ability to predict the behavior of sintered bubbles under *in situ* compression although we cannot perform those tests experimentally due to the high strength and stiffness displayed by these bubbles that exceeds the capacity of our *in situ* indentation system.

FEA is also used to study the secondary cracking events on as-assembled and calcined bubbles which experimentally are observed to be horizontal and vertical respectively. We can predict the horizontal cracking of half as-assembled bubbles with the use of an elastic-perfectly plastic Drucker-Prager material model that accounts for pressure-sensitive yielding and plastic dilation, whereas the use of a perfect elastic Von Mises material model predicts the vertical crack of half calcined bubbles.

# Chapter 5. Effect of Roughness and Porosity on the Mechanical Response of Shelled-Bubbles/Polymer Composites

## 5.1 Introduction

Syntactic foams are close cell structured foams made with hollow particles distributed in a polymeric matrix material.<sup>89</sup> In general, syntactic foams present low density and low moisture absorption, excellent hydrostatic and compressive strength, high energy absorption during deformation, and good thermal and acoustic insulation.<sup>5</sup> Syntactic foams are currently used in deep-water equipment,<sup>81, 137</sup> buoyancy modules,<sup>75</sup> aerospace vehicles,<sup>72</sup> pipeline thermal insulation, thermoformed packaging material, etc. The selection of the fillers and the matrices provide syntactic foams with great design versatility for targeted applications.<sup>79, 88, 138-140</sup> The hollow microparticles will mainly affect the compressive properties of the syntactic foam, whereas the matrix material used will impact the tensile properties.<sup>5</sup> However, although the properties of the components affect the mechanical response of the composite, if the filler-matrix interface is weak, the mechanical stability will be easily compromised.<sup>141</sup> Therefore, the interface between the hollow microparticles and the polymeric matrix plays a critical role.<sup>5, 7</sup> To improve the adhesion between fillers and matrix in syntactic foams, previous studies have used different surface treatments,<sup>8</sup> or have reinforced the composite incorporating fibers,<sup>9</sup> or graphene platelets.<sup>142</sup> The results of these efforts have shown a slight increase or even

negative effect on the interface strength. Hence, new mechanisms to increase the interfacial strength between fillers and matrix in syntactic foams are necessary.

In our approach, we use silica nanoparticle-shelled bubbles generated with a microfluidic technique,<sup>12</sup> which allows us to prepare monodisperse bubbles with precise control over the geometry of the final shelled-bubbles. These shelled bubbles are further modified with thermal processes to change their shell structure and their mechanical properties. The end products are two types of shelled bubbles: one with a rough and porous surface (calcined at 1000 °C) and the other with a smooth and non-porous surface (sintered at 1200 °C). Sintered bubbles present strength and stiffness that are an order of magnitude higher than that of calcined bubbles (see Chapter 3).

In this study we evaluate the compressive mechanical properties of composites using both rough/porous bubbles (calcined) and smooth/non-porous bubbles (sintered) mixed with UV-curable polyurethane acrylate. We show that the mechanical properties of composites with calcined bubbles under compression present higher strength, higher stiffness, larger strains at peak stress, and higher toughness than composites with sintered bubbles. We hypothesize that the roughness and porosity of the bubble shells plays a major role in the properties of the final composite, by means of greatly enhancing the adhesion between the matrix and the fillers, by allowing interpenetration of the polymer throughout the pores and wrinkles in the shell before curing.

## 5.2 Experimental Section

### 5.2.1 Generation and Preparation of Nanoparticle-Shelled Bubbles

The generation of nanoparticle-shelled bubbles is performed following the microfluidic method described in section 2.2.1.<sup>12, 98</sup> After setting the flow rates and the gas pressure for the desired bubble geometry and letting the flow rates to stabilize, the nanoparticle-shelled bubbles generated are collected at the end of the device in a petri-dish. The generation is allowed to continue for 2-3 hours to obtain a large volume of bubbles (~1.5ml of dried bubbles).

The methods used for the thermal processes of calcination and sintering of the nanoparticle-shelled bubbles are similar to the methods reported in section 3.2.2 modified to obtain a higher throughput. 1-2 ml of a highly concentrated suspension of bubbles in water (obtained by removing the excess of water of the collected bubbles after generation) is placed in a ceramic crucible. The water remaining in the sample is pipetted out of the crucible and any water left is allowed to evaporate at normal conditions in an open-air environment. The ceramic crucible containing the dried nanoparticle-shelled bubbles is then subjected to the thermal treatment of calcination or sintering, with set temperatures of 1000 °C and 1200 °C respectively, using a Thermo Scientific Thermolyne Furnace Benchtop Muffle type F47900 for 1 hour. The furnace is then turned off and the sample is allowed to slowly cool down to room temperature inside the furnace. When the sample is cooled down, the bubbles are transferred into a vial for a later use. To detach the sintered bubbles from each other, the bubble aggregates are transferred into a vial

with DI water and put in a vertical rotating disk overnight. The detached floating sintered bubbles are then transferred to a new vial and allowed to dry in open air at room temperature.

The surface functionalization is carried out using different bonding agents: methacryloxypropyltrimethoxysilane (MPS), 3-acryloxypropyltrimethoxysilane (APS), and a blend of two silane coupling agents, APS and *bis*[3-(trimethoxysilyl)propyl]amine (BSA). The functionalization is carried out following a previously reported method.<sup>143</sup> 1ml of the solution containing 4ml of ethanol, 1ml DI water, 0.75 ml of  $\text{NH}_3\cdot\text{H}_2\text{O}$  with 30 $\mu\text{l}$  of silane bonding agent (MPS, APS, or 30 $\mu\text{l}$  of APS and 15 $\mu\text{l}$  of BSA) is mixed with approximately 0.5 ml of dried bubbles. The suspension is thoroughly mixed during 24h at room temperature. After the surface modification, the solution is discarded and the treated bubbles washed with ethanol to remove any excess of silane. The resulting treated bubbles are then dried in a vacuum oven at 40-60 °C until completely dried.

### **5.2.2 Composite Mold Casting and Sample Preparation**

The polymer used to form the matrix of the final composite is UV-curable polyurethane acrylate (PUA, 100BSR, from Minuta Technology, Korea, with viscosity ~50cps at 25°C, and Young's modulus after curing ~125MPa). PUA is pipetted into an eppendorf tube containing the dried calcined or sintered nanoparticle shelled bubbles to a set weight percent of 10, 20, or 30%. Each sample is then gently mixed using a wood applicator until the bubbles are homogenously distributed. The molds used to shape the samples are

laser cut cylindrical orifices on a 1/8" clear acrylic sheet. The acrylic mold is glued to a glass slide to form the base of the mold. The bubble-PUA mixture is then poured into the orifices of the mold and covered with another glass slide carefully avoiding trapping any excess air in the samples. The top glass slide is pressed against the mold and tight with a piece of parafilm. The sample is then attached to a 7 rpm - 12 V DC geared motor connected to a DC power supply set to 3 rpm (5V) while UV light is exposed to the sample. After 15-30 minutes of exposure the parafilm is then removed and the sample is left rotating under UV exposure for at least an additional 8h. After the samples are cured inside the molds, the edges are polished removing any excess of cured mixture, and flattened for the compression testing.

To remove the cured composite samples from the mold and prepare them for the mechanical testing compression, the glass slides of the top and bottom of the mold are removed. Some excess of cured PUA-bubble mixture might remain outside of the mold after curing, and is removed with mechanical polishing using sand paper and gentle application, until both sides are smooth. The generated dust is removed using a slightly wet wipe and compressed air. The composite samples are taken out of the acrylic mold by cutting the mold open using a razor blade, without damaging the samples. Several cuts can be made on the acrylic mold to release the cured composite sample without applying any stress on it. The dimensions of each sample, diameter, height and weight, are then measured, and the density of each sample is calculated from the weight of the sample and the average volume. The laser cutter used to shape the molds on the acrylic sheet produces a slight tapering with a nominal kerf of 0.007 inches. To consider this variation

on the dimensions of the samples, the diameter is averaged from the measured diameter at the top and at the bottom of the sample. The final aspect ratio (height/diameter) of the samples is  $\sim 1$ . All length measurements are done with a calibrated electronic caliper and the reported values correspond to the average of three independent measurements.

The composite samples with different silane treatments (MPS, APS, and APS/BSA) are made from sintered bubbles of the same batch (outer diameter,  $d \sim 38 \mu\text{m}$ , thickness,  $t \sim 1.2 \mu\text{m}$ ). A second batch of sintered bubbles ( $d \sim 39 \mu\text{m}$ , and  $t \sim 1.1 \mu\text{m}$ ) is used to generate the composites with non-treated and APS/BSA treated surface, and different volume fractions of bubbles. A different batch of bubbles is used to generate calcined bubbles ( $d \sim 39 \mu\text{m}$ , and  $t \sim 1.5 \mu\text{m}$ ) and prepare the composites with non-treated and APS/BSA treated surface, and different volume fractions.

### **5.2.3 Mechanical Testing of Composites**

The compressive properties of the composite samples are obtained by mechanical compression to failure using a flat circular indenter (diameter 1/2 inch). The indenter is connected to a 1 kN load cell attached to an Instron (Model 5848 Microtester, Instron, Canton, MA) for a precise control of the vertical displacement. The uniaxial compression tests are displacement controlled with constant nominal strain rate of  $\dot{\varepsilon} = 0.0005 \text{ s}^{-1}$  (80-85  $\mu\text{m}/\text{sec}$ ). Load-deflection data is tracked during the experiment and extracted for analysis. The compressive stress (engineering stress) is calculated by  $\sigma = P/A$ , where  $P$  is the load and  $A$  is the initial cross sectional area of the sample. The strain (engineering



strain) is calculated by  $\varepsilon = \delta/h_0$ , where  $h_0$  is the initial height of the sample and  $\delta$  the deflection imposed on the sample. All stress and strain values reported represent the engineering stress and engineering strain, respectively.

The elastic modulus or stiffness ( $E$ , MPa) is calculated from the slope of the initial linear region of the stress-strain curve. The compressive strength ( $\sigma_c$ , MPa) is the maximum stress that is reached before the sample fails. The peak strain ( $\varepsilon_{peak}$ , m/m) corresponds to the strain imposed when the maximum stress is reached before failure. The toughness ( $U$ , kJ/m<sup>3</sup>) is determined by measuring the area under the curve prior to fracture. Since the density of the samples changes significantly with the weight fraction of bubbles, the specific properties<sup>144</sup> (mechanical properties normalized by the density,  $\rho$ , g/ml) are calculated and studied.

The reported values for the sintered samples at 20 wt% of bubble content with different surface treatments: NT, MPS, APS, and APS/BSA, correspond to the average of 4, 4, 4, and 5 independent compression tests respectively.

The reported values for the calcined samples NT 10, 20, 30%, correspond to the average of 8, 8, and 7 independent tests respectively. The values for the calcined samples APS/BSA 10, 20, 30% correspond to the average of 7, 6, and 3 independent tests respectively. The values for the sintered samples NT 10, 20, 30% correspond to the average of 6, 5, and 5 independent tests respectively. The values for the sintered samples APS/BSA 10, 20, 30% correspond to the average of 6, 6, and 5 independent tests

respectively. The reported values for the PUA samples correspond to the average of 7 samples, from which 2 of them were mechanically compressed to failure.

## 5.3 Results and Discussion

Bubble-polymer composites in this study are generated using silica nanoparticle-shelled bubbles as fillers and UV-curable polyurethane acrylate as matrix. Silica nanoparticle-shelled bubbles are generated using a previously reported microfluidic technique that allows generating monodisperse bubbles with a precise control over the final geometry. These silica-shelled bubbles can be further modified with thermal treatments to enhance their mechanical properties and to modify the shell structure.

We use two different types of bubbles in our present study. The calcined bubbles are silica nanoparticle-shelled bubbles that present a rough outer surface and a porous shell (porosity  $\sim 30\%$ ), after being calcined at  $1000\text{ }^\circ\text{C}$ . The sintered bubbles, in contrast, have a smooth surface and their shell is non-porous, after sintering at  $1200\text{ }^\circ\text{C}$ . In our previous study we showed that sintered bubbles, compared to calcined ones, are much stronger, stiffer and can absorb greater energy before failure when tested individually to compression (see section 3.3.4), due to the loss of porosity.

The most commonly used matrix material for syntactic foams is epoxy resins, due to the high stiffness and strength, thermal stability, water resistance, and low shrinkage.<sup>145</sup> However, syntactic foams have been made of many different matrix

materials to provide the final composite with specific properties.<sup>5</sup> In our work, we use polyurethane acrylate (PUA) that due to its composition provides the composite with rigidity and flexibility, and it has been previously used in mold casting for photolithography techniques.<sup>146</sup> Its viscosity before curing is low allowing for a better mixing with the shelled-bubbles. In addition, the chosen PUA cures with UV exposure without the need of heating or applying vacuum while curing. Since the prepared composites samples are of relatively small size (~2 mm), UV-curable PUA is an appropriate candidate.

The composites are simply prepared by gently mixing the shelled bubbles with the polymeric matrix, for a set weight percent of the components, and poured into the mold for casting (see experimental section for details). The molds are previously prepared by laser cutting onto a commercially available acrylic sheet of 1/8" thickness, as shown in Figure 5.1a. The mixture of bubbles and polymer is covered with a glass slide before it is exposed to UV-light for cross linking of the matrix, to avoid oxygen to scavenge for the radicals.<sup>147</sup> During curing of the composite, the samples are placed in a rotation fixture turning at 3 rpm to prevent the buoyant bubbles to accumulate in the top most part of the sample before is completely cured. After the samples are cured inside the molds, the edges are polished to remove any excess of cured mixture, and to flatten them for the compression testing. The final aspect ratio (AR, height/diameter) is chosen to be 1 to optimize the maximum capacity of the available load cell and avoiding buckling and shearing of samples under compression when  $AR > 2$ .<sup>148</sup>

The density of the samples is measured after they are cured. In this way, any air unavoidably trapped between the filler and the binder is taken into account in the density value. The density of the composites decreases with the increase in percentage of bubbles, since a larger amount of bubbles will incorporate larger volume of air causing a decrease of the final weight, see Figure 5.1b. The density drops considerably with the increase in weight percent of bubbles, amounting to an approximate 20% density loss between the samples containing 10 and 30 wt% of shelled bubbles on them, as it could be expected calculated from the density of the bubbles ( $\rho_{bubble} \sim 0.5 - 0.7$  g/ml) and the density of the PUA ( $\rho_{PUA} \sim 1.15$  g/ml).

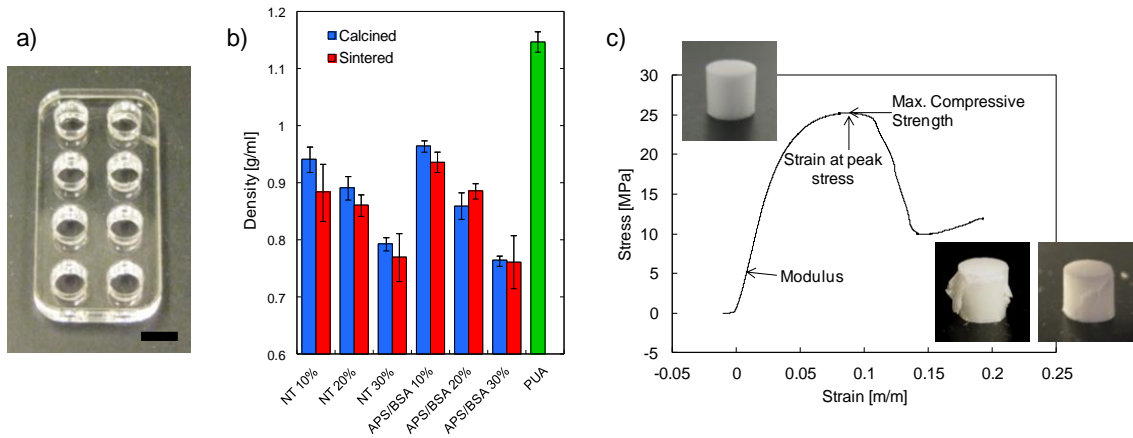


**Figure 5.1** (a) Laser cut mold in acrylic sheet, 1/8” thick, for composite sample preparation (scale bar 2 mm), (b) density of samples, (d) typical stress-strain curve obtained from compression testing of composite, insets correspond to samples before and after testing (height of samples ~1.8 mm). NT refers to non-treated surface. APS/BSA refers to the coupling agents used to treat the surface.

The different composites are mechanically characterized under compression, deflection controlled with constant strain rate  $\dot{\epsilon} = 0.0005 \text{ s}^{-1}$ , using a flat indenter

attached to an Instron with a maximum capacity of 1 kN (see experimental section for details). Load-deflection data is tracked during the experiment and extracted for analysis. A typical stress-strain curve extracted from a compression test of a composite sample is shown in Figure 5.1c. As it can be seen in the inset images, the composite specimens fail with a brittle fracture, when one or multiple cracks propagate through the composite. The crack initiates at the peak stress, indicating point of failure of the composite.

The elastic modulus or stiffness ( $E$ , MPa) is calculated from the slope of the initial linear region of the stress-strain curve. The compressive strength ( $\sigma_c$ , MPa) is the maximum stress that is reached before the sample fails. The peak strain ( $\varepsilon_{peak}$ , m/m) corresponds to the strain imposed when the maximum stress is reached before failure. The toughness ( $U$ , kJ/m<sup>3</sup>) is determined by measuring the area under the curve prior to fracture. Since the density of the samples changes significantly with the weight fraction of bubbles, the specific properties<sup>144</sup> (mechanical properties normalized by the density,  $\rho$ , g/ml) are calculated and studied.

The surface of the bubbles is further modified by a silanization reaction on the surface of the silica shell of the bubbles to enhance the strength of the interface between matrix and fillers. Different silane coupling agents previously reported as binders in particulate composites are tested on the surface of the sintered bubbles: methacryloxypropyltrimethoxysilane (MPS),<sup>149</sup> 3-acryloxypropyltrimethoxysilane (APS),<sup>150</sup> and a blend of two silane coupling agents, APS and *bis*[3-(trimethoxysilyl)propyl]amine (BSA).<sup>143</sup> Composites using sintered bubbles, with non-

treated (NT) and functionalized surfaces are prepared at 20 wt% bubble content, to determine which of the coatings better enhances the adhesion between filler and matrix. Compression testing on the composite samples (see experimental section for details) is performed to determine which treatment provides the better response. As it is shown in Figure 5.2, the treatment with APS/BSA mixture seems to slightly enhance the specific stiffness, strength, and toughness. APS/BSA blend is used as coupling agent for the following tests.

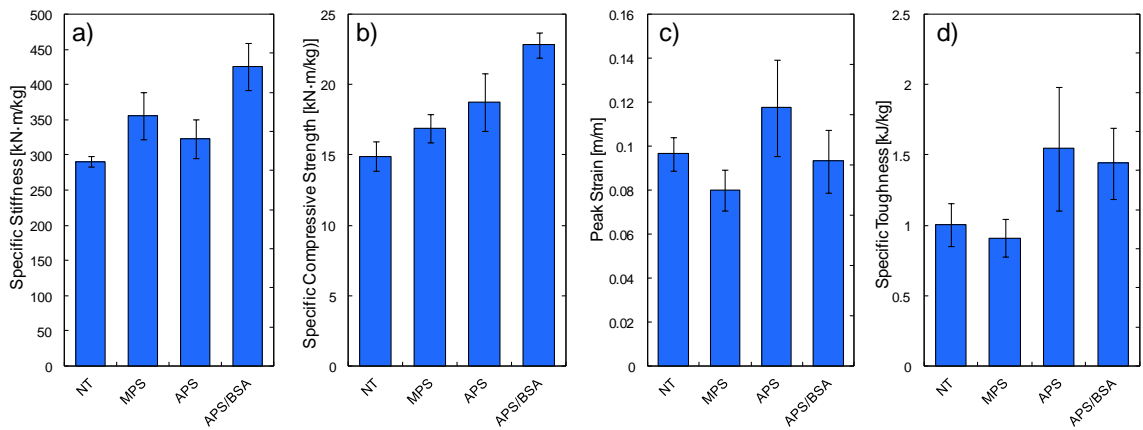


**Figure 5.2** Mechanical response of composites using sintered bubbles with different surface treatments: non-treated (NT), MPS, APS, and a combination of APS and BSA. (a) Specific stiffness, (b) specific compressive strength, (c) peak strain, and (d) specific toughness.

Composite samples containing rough/porous bubbles (calcined), and composite samples with smooth/non-porous bubbles (sintered), are then prepared. In addition, calcined and sintered bubbles are treated with the APS/BSA bonding agents in an attempt to improve the adhesion between fillers and binder. It is important to note that calcined and sintered bubbles in these results were generated from different initial batches of nanoparticle-shelled bubbles (different average diameters, and shell thicknesses, see

experimental section) and some of the observable differences when incorporated in composites might be affected by it. Further experiments using the same initial batch of nanoparticle-shelled bubbles to produce calcined and sintered bubbles are performed to corroborate the results shown in this Chapter. Those additional experiments and results are described in the Appendix 2.

The results of the mechanical characterization of the composites are shown in Figure 5.3. It is interesting to note, before looking at the effects of volume fraction and surface treatment on the mechanical properties, that the composites prepared with calcined bubbles, rough and porous in their shell, have a better mechanical response than the composites prepared with sintered bubbles, smooth and non-porous. Calcined bubble composites display higher specific stiffness, much larger specific strength, higher values of peak strains, and a noticeably larger toughness (see Figure 5.3a-d). These results seem counterintuitive since the mechanical properties of individual sintered bubbles are much higher than calcined bubbles. We hypothesize that the cause for the outstanding response of the calcined bubble composites relay in the roughness and porosity of the shell, that provides the fillers with greater adhesion to the matrix, largely increasing the interfacial strength. Previous studies have used chemical bonding agents, such as the ones we also test in our study (MPS, APS, APS/BSA), to modify the interfacial strength, however, to the best of our knowledge, the use of rough bubbles has not been studied as a physical mean to enhance adhesion in syntactic foams.

In addition, we observe that the specific stiffness of the composites increases with the volume fraction of bubbles, which indicates that incorporating shelled bubbles in the

soft matrix, stiffens the composite reaching a value almost 10x higher for the calcined-30wt% composite (see Figure 5.3a). However, the increase of the volume fraction decreases the strain at peak and consequently the specific toughness (see Figure 5.3c and **d**), indicating that the flexibility of the matrix is compromised and the deflection to failure lowered when more bubbles are incorporated.

From the results for the non-treated bubbles (NT) on Figure 5.3b, we observe that the volume fraction does not have an effect on the specific compressive strength, which could indicate that failure is governed by debonding of the fillers and the matrix through the interface. It seems however that the functionalization of the surface with the silane bonding agents (APS and BSA), helps strengthening the interface, and this is more pronounced at higher volume fraction of bubbles and larger interfacial area. The peak strain and the toughness seem to be less affected by the surface modification.



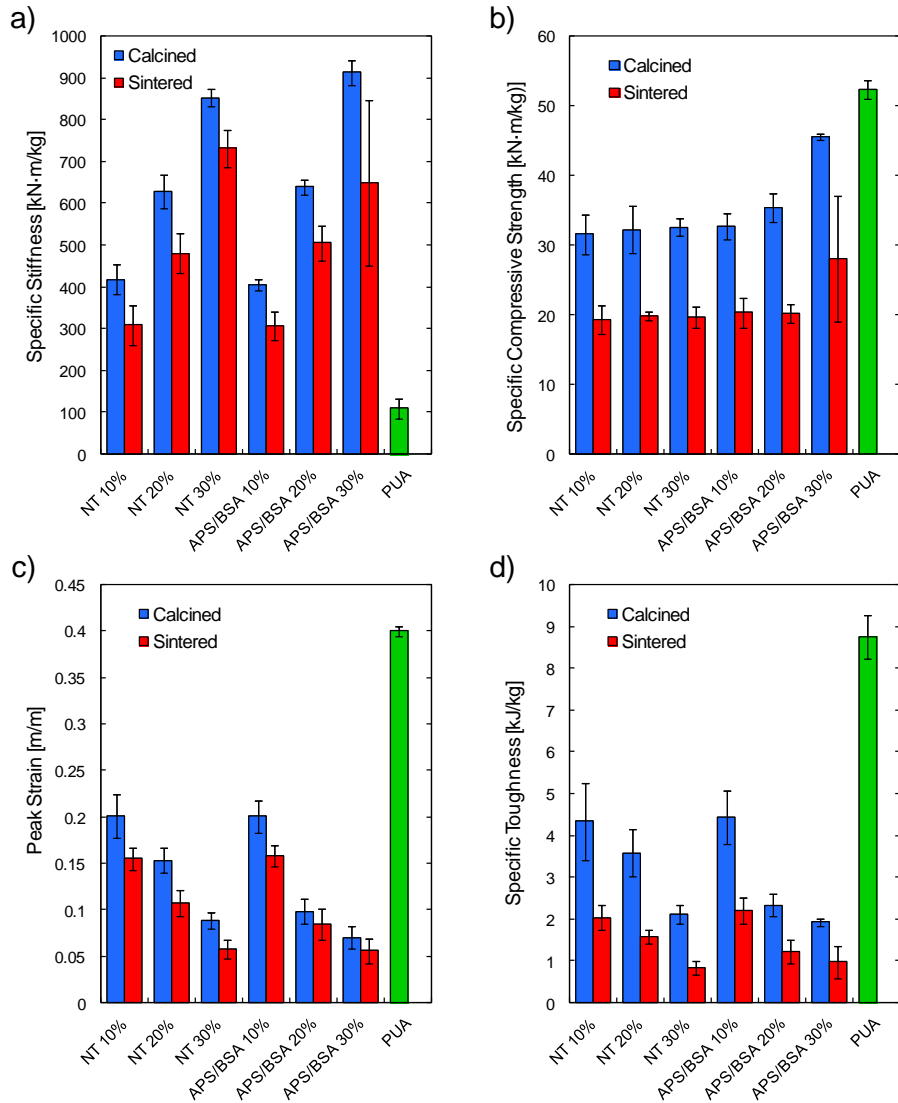


**Figure 5.3** Bar charts representing the mechanical properties of composites extracted from the compression testing to failure. (a) specific stiffness, (b) specific compressive strength, (c) peak strain, and (d) specific toughness.

Observation of the fracture surfaces after the mechanical compression provides some information on the different failure mechanisms. SEM images of different samples are shown in Figure 5.4. Figures a and c show the surface of calcined and sintered bubbles respectively, revealing roughness of the calcined shell not apparent on the

sintered shell. The presence of pores in the calcined shells can be deduced from the cross section image (inset of figure a) in which individual particles can be observed, and the interstices between them form the pores.

The surface of a fractured composite prepared with calcined bubbles (APS/BSA-30%) can be seen in Figure 5.4b. This image shows thin layers of PUA partially covering bubbles (indicated by the red arrows) that are not observed for the sintered bubble composite (APS/BSA-30%) of Figure 5.4d. The presence of these thin layers of PUA on the surface of the calcined bubbles suggests penetration of the polymer throughout the undulations of the shell resulting in a larger interfacial area between bubbles and polymer, and greater adhesion, and consequently better mechanical response as observed before.

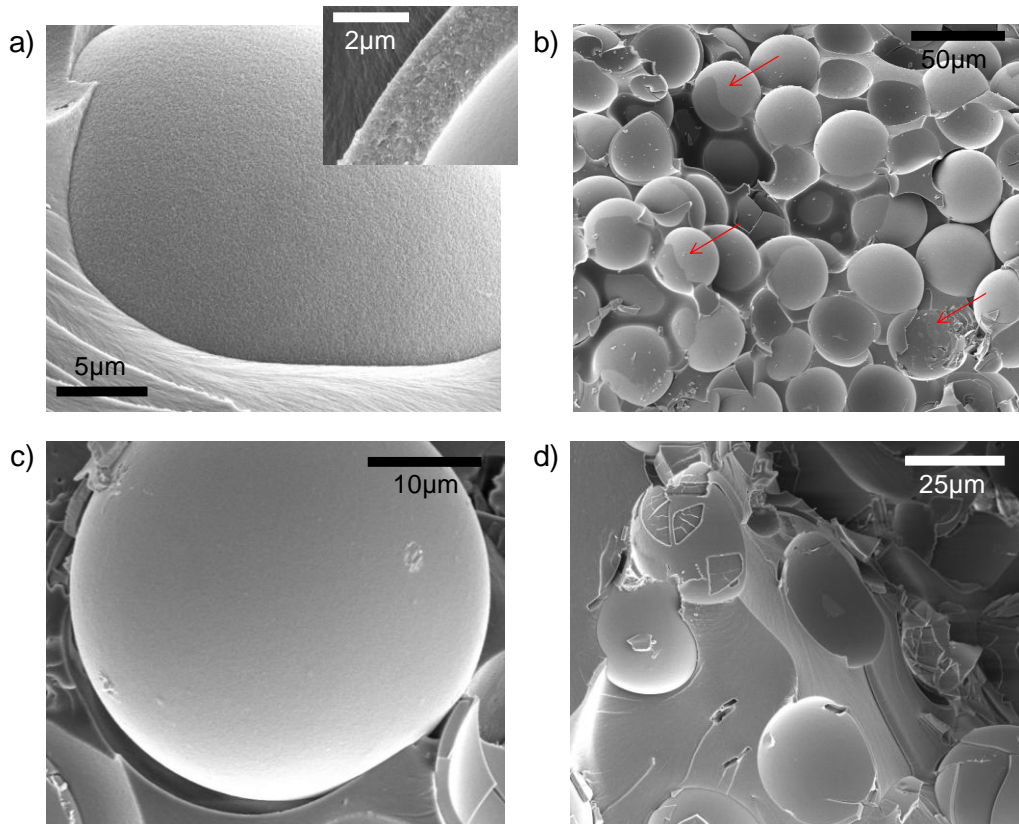


**Figure 5.4** SEM images of bubbles in composites after mechanical testing: (a) Surface of a calcined bubble showing roughness, inset is a cross-section of a calcined shell in which individual particles can be observed; (b) Fracture surface of calcined APS/BSA 30% composite; (c) Surface of a sintered bubble with a smooth surface; and (d) Fracture surface of sintered NT 30% composite.

## 5.4 Conclusions

In this study, we report the preparation of polymer-bubble composites, or syntactic foams, using thermally processed microfluidic nanoparticle-shelled bubbles as fillers and UV-curable polyurethane acrylate as matrix. Two types of bubbles are used, rough/porous calcined bubbles and smooth/non-porous sintered bubbles. In addition, we

study the effects of volume fraction of bubbles and surface functionalization on the mechanical response of these composites under compression.

Calcined bubbles, less stiff and strong than sintered ones, provide the composite with better mechanical response (higher stiffness, strength, and toughness). This staggering result indicates that the interface between fillers and matrix plays a critical role on the mechanical response of composites. We have observed that the contribution of the interface is more decisive than the mechanical properties of the fillers forming the composite. Hence, a weaker interface will compromise the mechanical response even if highly stiff, strong and tough bubbles are used. We also conclude that roughness and porosity are critical variables to enhance the interfacial adhesiveness, since the polymer chains are able to penetrate through the undulations and pores of the surface providing a larger contact area between the components. From our study, we cannot convey the independent contribution of the porosity or roughness since the bubbles used are both rough and porous, or smooth and non-porous. Independently on which of these properties have a stronger impact, the overall result opens a myriad of possibilities to improve the mechanical response of composites by controlling the surface roughness/porosity of the bubble shells.

We also study the effect of the volume fraction and surface treatment. An increasing incorporation of shelled-bubbles in the polymer composite increases the specific stiffness while decreases the strain at peak and the specific toughness, and does not have an effect on the specific compressive strength. The use of bonding agents (APS and BSA) slightly strengthens the interface between bubbles and polymer and causes an

increment of the specific compressive strength at higher volume fractions. The peak strain and specific toughness seem to be independent on the interface modification.

## Chapter 6. Conclusions and Outlook

The principal goal of this thesis is the generation of hierarchical lightweight materials with desired mechanical properties. The work in this thesis contributes toward this objective in different levels, assembling nanoparticles using microfluidic bubbles as templates, exploring the ability to modify the surface and tailor the structure and mechanical properties of these shelled bubbles, and incorporating these nanoparticle-shelled bubbles in composites observing the effect of the hierarchical assembly on the overall macroscopic properties.

*Chapter 1* describes the challenges present on the generation of lightweight materials with high stiffness, strength and toughness. It summarizes the current approaches of generating syntactic foams, using hollow microparticles and polymers in composites, and the limitations present when the hollow microparticles used are generated using conventional bulk methods. Chapter 1 presents microfluidics as a method to generate nanoparticle-shelled bubbles and its benefits over conventional bulk methods, and summarizes the goals and approaches of this thesis.

*Chapter 2* presents the potential of nanoparticle assemblies using microfluidic bubbles. It shows that a precise control over the conditions during the microfluidic generation of gas-in-oil-in-water (G/O/W) bubbles enables the generation of ultra-stable nanoparticle-shelled bubbles that withstand drying without breaking or compromising their structure. This finding allows for a deeper exploration of the potential of these nanoparticle assemblies, for example, this chapter also describes the assembly of these

nanoparticle-shelled bubbles at interfaces in hexagonal close packed arrays or in fractal-like structures when the surface is partially modified. A deep fundamental study of the behavior at the interface of these bubbles is also presented.

*Chapter 3* proposes the use of these nanoparticle-shelled bubbles as building blocks for the generation of lightweight materials. It describes the ability to tailor the structure of these shelled bubbles using thermal treatments that provides the shelled bubbles with different mechanical properties, optimal for targeted applications. Therefore this chapter presents the potential of these nanoparticle-shelled bubbles and provides an in depth study of the structure-property relation, necessary for the practical application of these materials. In Chapter 3 the mechanical properties of shelled bubbles are studied using nanoindentation and *in situ* compression tests.

*Chapter 4*, complementing Chapter 3, uses simulation work to explain the mechanical behavior of the different nanoparticle-shelled bubbles described in the previous chapter. As-assembled bubbles can be modeled using an elastic-perfectly plastic material, while calcined and sintered bubbles display an elastic behavior. The differences in the secondary cracking events observed *in situ* are explained by FEA using a Drucker-Prager material model for the as-assembled bubbles that incorporates pressure sensitivity and plastic dilation. In addition to the material models the simulation work of this chapter reveals that the geometry of the shells have a significant impact on the mechanical behavior. The modeling of the shelled bubbles in this chapter provides invaluable information for designing purposes.

*Chapter 5* presents the preparation and mechanical characterization of syntactic foams using the previously studied nanoparticle-shelled bubbles, calcined (at 1000 °C) and sintered (at 1200 °C), as fillers. This chapter addresses the goal of generating three dimensional assembly of the nanoparticle-shelled bubbles in composites. A great emphasis is placed on enhancing the interfacial strength between fillers and matrix since it is a current challenge that can easily compromise the mechanical properties of the composite. The mechanical properties of composites made using porous and rough calcined bubbles display better mechanical properties than composites made with smooth and non-porous sintered bubbles despite the fact that individual sintered bubbles present much better properties than calcined bubbles (see Chapter 3 and Chapter 4). The roughness and porosity of the calcined bubble shells by means of increasing the surface area and contact area with the polymeric matrix, greatly enhances the interfacial strength of the composite. These results show that hierarchically assembled nanoparticles using microfluidic bubbles as templates, gave us the opportunity to make rough and porous bubbles to generate lightweight materials with high mechanical properties.

Some fundamental questions and challenges are still open to be resolved and explored. For example, it will be important to quantify the interfacial strength of the nanoparticle-shelled bubbles in the polymer composites to better understand the effect that roughness and porosity of the bubbles can impart. Several studies have suggested methods to measure the interfacial strength in particulate composites by determining the debonding stress by acoustic emission experiments,<sup>151</sup> or more commonly by measuring



the macroscopic tensile properties of the composite and determining the interfacial strength with semi-empirical equations.<sup>152</sup>

It will be of interest to explore the potential of the microfluidic generation of bubbles, further exploring the generation of non-spherical bubbles, which could result in anisotropic materials when arranged in three dimensional regular structures. Platelet shaped bubbles can be formed by compression of A/O/W compound bubbles before complete solvent evaporation as shown the preliminary result in Figure 6.1. The compression is performed between two flat substrates. The final aspect ratio is controlled using spacers of different sizes.

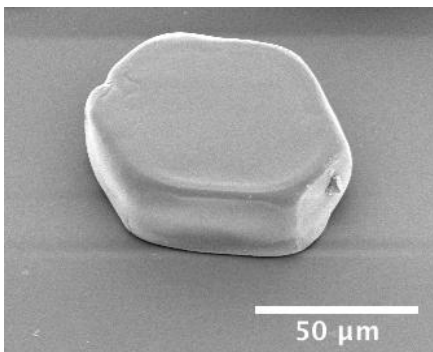


**Figure 6.1** SEM image of a platelet bubble

Other fundamental questions remain to be answered in the two-dimensional assembly of bubbles at interfaces, in which a controlled Janus boundary could lead to interesting arrangements for practical applications.

We have observed that the interfacial strength of the bubble/polymer composites notably increases when roughness and porosity are present in the bubbles. Therefore, it

will be important to explore the potential of this finding. For example, study different ways to control the porosity and roughness of the bubble shells using different nanoparticle sizes to form the shell, or different materials, that when thermally processed will melt at different temperatures. Another way to enhance the interfacial strength will be to combine methods of polymer infiltration through the nanoparticles forming the shell using for example temperature and vacuum that will increase the interfacial area between nanoparticles and polymer.

Another interesting study will be to perform finite element analysis of the bubble-polymer composites. Simulations can provide a detailed independent analysis of the effects of the structural variables of the composite (volume fraction of bubbles, mechanical properties of constituents, polydispersity on the geometry and/or mechanical properties of the fillers, etc.) on the overall mechanical response of the composite. This understanding will be critical for designing purposes in the generation of functional lightweight materials.

# Appendix 1. Finite Element Analysis Code

The following code was developed to simulate the mechanical response of single bubbles under compression similarly to the experimental tests performed (see Chapters 3 and 4). This code and its variations were used with ANSYS 13.0 commercially available software.

## A1.1 Axisymmetric FEA

```
/config,NRES,10000      !Increase the total number of substeps from 1000(default) to 10000
/PREP7

!This file contains the summary of all axisymmetric simulations performed for the study,
!which results are included in the paper:
!Brugarolas, T.; Gianola, D. S.; Zhang, L.; Campbell, G. M.; Bassani, J. L.; Feng, G.; Lee, D.,
!"Tailoring and Understanding the Mechanical Properties of Nanoparticle-Shelled Bubbles.
!ACS Applied Materials & Interfaces 2014. with DOI: 10.1021/am502290h
!
!This file includes:
! - Variation on the indenter shape
! - Variation on the mechanical properties of bubbles (Young's Modulus, yield strength,...)
! - Variation on the uniformity of the bubble shell (uniform, thin at top, thin at bottom)
! - Variation on the average diameter and shell thickness for the different cases

!*****Element type: 2D axisymmetric quadratic element
ET,1,PLANE183
KEYOPT,1,1,0      !Keyopt(1,1) element shape: 8-node quadrilateral; 6-node triangle
KEYOPT,1,3,1      !Keyopt(1,3) element behavior: 0-plane stress; 1-axisymmetric; 3-plane stress with
thickness (TK) real constant input; 5-generalized plane strain
KEYOPT,1,6,0      !Keyopt(1,6) element formulation: 0-use pure displacement formulation (default); 1-use
mixed u-P formulation (not valid with plane stress)

!*****Material properties of the bubble shell material (Material 1):
!As-assembled bubbles: E = 6.8642077e-3 N/um^2 = 6.8642077 GPa;
!sigmaY = 0.1175610e-3 N/um^2 = 117.5610 MPa
!Poisson ratio assumed: nu = 0.18
!For as-assembled bubbles the material properties are input as follows (elastic-perfectly
!plastic material, tang=0):
MPTEMP,,,,,,,,
MPTEMP,1,0
MPDATA,EX,1,,6.8642077e-3      !N/um^2
MPDATA,PRXY,1,,0.18
TB,BISO,1,1,2,
TBTEMP,0
TBDATA,,0.1175610e-3,0,,,
```

!Calcined bubbles (700C): E = 13.6802611e-3 !N/um<sup>2</sup> ; also used E = 20GPa  
 !Sintered bubbles (1200C): E = 75.9861953e-3 !N/um<sup>2</sup>  
 !Poisson ratio assumed:  $\nu = 0.18$   
 !For calcined and sintered bubbles the material properties are input as follows since the  
 !material is perfect elastic:  
 !MPTEMP,,,,,,,,  
 !MPTEMP,1,0  
 !MPDATA,EX,1,,13.6802611e-3 !N/um<sup>2</sup> This value needs to be updated to the corresponding E  
 !MPDATA,PRXY,1,,0.18

!\*\*\*\*\*Material properties of the silicon substrate (Material 2)  
 !E = 162GPa;  $\nu = 0.22$   
 MPTEMP,,,,,,,,  
 MPTEMP,1,0  
 MPDATA,EX,2,,162e-3 !N/um<sup>2</sup>  
 MPDATA,PRXY,2,,0.22

!\*\*\*\*\*Geometry of substrate defined by its coordinates (x,y)=(0,0) and width and height  
 !(square shape 175x175 um<sup>2</sup>)  
 BLC4,0,0,175,-175

!\*\*\*\*\*Geometry of the Bubble defined as two circles, and subtracting the outer circle  
 !to the inner circle(concentric or not, to provide uniform shape or non-uniform shape  
 !respectively)

!As-assembled uniform shell:

CYL4,0,20.3,20.3

CYL4,0,20.3,17.4

ASBA,2,3

!As-assembled thin at top:

!CYL4,0,20.3,20.3

!CYL4,0,20.8,17.4

!ASBA,2,3

!As-assembled thin at bottom:

!CYL4,0,20.3,20.3

!CYL4,0,18.9,17.4

!ASBA,2,3

!For calcined and sintered bubbles the outer diameter changes, and the thickness of the  
 !shell changes. These values need to be updated reflecting that:

!Calcined uniform:

!CYL4,0,18.9,18.9

!CYL4,0,18.9,16.2

!ASBA,2,3

!Calcined thin at top:

!CYL4,0,18.9,18.9

!CYL4,0,19.5,16.2

!ASBA,2,3

!Calcined thin at bottom:

!CYL4,0,18.9,18.9

!CYL4,0,18.3,16.2

!ASBA,2,3

!Sintered uniform:

!CYL4,0,17.3,17.3

!CYL4,0,17.3,14.7

```

!ASBA,2,3
!Sintered thin at top:
!CYL4,0,17.3,17.3
!CYL4,0,17.9,14.7
!ASBA,2,3
!Sintered thin at bottom:
!CYL4,0,17.3,17.3
!CYL4,0,16.7,14.7
!ASBA,2,3

```

```

!*****Geometry of the bubble: Delete half particle for axisymmetric problem:
!This code remains the same for all cases if the definition of the whole shell is defined
!as stated in the lines above. The deletion of half of the bubble is done using nodes and
!they are numbered in the same order if the above commands are kept as they are. If the
!above commands are changed (i.e. the geometry changes from circular to other shape, or the
!definition of the indenter is done before the definition of the shell) the following will
!need to be updated accordingly
LSTR,4,12    !Generate 1 small line between top apices of both circles, creation of line 13
LSTR,10,6    !Generate 1 small line between bottom apices of both circles, creation of line 14
FLST,3,2,4,ORDE,2    !Selection of area 3
FITEM,3,13    !Selection of line 13
FITEM,3,-14    !Selection of line 14
ASBL,4,P51X    !Divides selected area with selected lines
ADELE,3, , ,1    !Delete area 3 (left part of shell)

```

```

!*****Geometry of indenter. The shape of indenter needs to be updated depending on which
!simulations are being done
!Simulating nano-indentation with spheroconical indenter (spherical indenter is needed)
!Simulating in situ compression with flat indenter (flat indenter is needed)
!--Spherical indenter of 10um in radius
!For as-assembled bubble:
K,13,0,50.6,0,
CIRCLE,13,10
!For calcined bubble:
!K,13,0,47.8,0,
!CIRCLE,13,10
!For sintered bubble:
!K,13,0,44.6,0,
!CIRCLE,13,10
!--Flat indenter of 50um in width (since it is an axisymmetric problem only half the
!indenter needs to be drawn 25um)
!For as-assembled bubble:
!K,13,0,40.6,0,
!K,14,25,40.6,0
!L,13,14
!For calcined bubble:
!K,13,0,37.8,0,
!K,14,25,37.8,0
!L,13,14
!For sintered bubble:
!K,13,0,34.6,0,
!K,14,25,34.6,0
!L,13,14

```

```

!*****Material attribution to areas before meshing
!If materials are defined as above and in the same order, this part of the code doesn't
!need to change when simulating as-assembled, calcined or sintered bubbles.
!Material 1(SiO2 with different values of E and sigmaY for as-assembled, calcined and
!sintered) associated to area A3(shell)
CM,_Y,AREA
ASEL, , , 2
CM,_Y1,AREA
CMSEL,S,_Y
!*
CMSEL,S,_Y1
AATT, 1, , 1, 0,
CMSEL,S,_Y
CMDELE,_Y
CMDELE,_Y1
!Material 2(Si) associated to area A1(substrate)
CM,_Y,AREA
ASEL, , , 1
CM,_Y1,AREA
CMSEL,S,_Y
!*
CMSEL,S,_Y1
AATT, 2, , 1, 0,
CMSEL,S,_Y
CMDELE,_Y
CMDELE,_Y1

!*****Meshing of substrate
!The substrate is defined with lines 1-4, therefore meshing can be done as follows:
LESIZE,3, , ,120,0.01, , ,1 !Meshing of line 3
LESIZE,4, , ,120,100, , ,1 !Meshing of line 4
LESIZE,1, , ,15,1, , ,1 !Meshing of line 1
LESIZE,2, , ,15,1, , ,1 !Meshing of line 2
! Mesh the area based on the mesh of the lines
AMESH,1

!*****Meshing of the shell
!The shell is defined with lines 8,9,12,14, and 15, therefore the meshing can be done as
!follows for all cases.
!This meshing comprises more than 5000 elements and 15000 nodes with at least 16 elements
!radially spanning from the inner shell surface to the outer shell surface:
LESIZE,14, , ,30,1, , ,1
LESIZE,15, , ,30,1, , ,1
LESIZE,5, , ,180,1, , ,1
LESIZE,8, , ,180,1, , ,1
LESIZE,9, , ,135,1, , ,1
LESIZE,12, , ,135,1, , ,1
AMESH,2

!*****Contact between pairs of elements.
!The contact pairs are defined using the wizard
!Located in: Main Menu>Preprocessor>Modeling>Create>Contact Pair

```

```

!The log data (List>Files>Log File) of the contact pair is substituted here for each case
!--Contact pair 1(Shell-Substrate)--- (This section needs to be updated if geometry and meshing changes)
!The contact is assumed frictionless and the element types used are TARGE169, CONTA172
/COM, CONTACT PAIR CREATION - START
CM,_NODECM,NODE
CM,_ELEMCM,ELEM
CM,_KPCM,KP
CM,_LINECM,LINE
CM,_AREACM,AREA
CM,_VOLUCM,VOLU
/GSAV,cwz,gsav,,temp
MP,MU,1,
MAT,1
R,3
REAL,3
ET,2,169
ET,3,172
KEYOPT,3,9,0
KEYOPT,3,10,2
R,3,
RMORE,
RMORE,,0
RMORE,0
! Generate the target surface
LSEL,S,,,8
CM,_TARGET,LINE
TYPE,2
NSLL,S,1
ESLN,S,0
ESURF
CMSEL,S,_ELEMCM
! Generate the contact surface
LSEL,S,,,3
CM,_CONTACT,LINE
TYPE,3
NSLL,S,1
ESLN,S,0
ESURF
ALLSEL
ESEL,ALL
ESEL,S,TYPE,,2
ESEL,A,TYPE,,3
ESEL,R,REAL,,3
/PSYMB,ESYS,1
/PNUM,TYPE,1
/NUM,1
EPLOT
ESEL,ALL
ESEL,S,TYPE,,2
ESEL,A,TYPE,,3
ESEL,R,REAL,,3
CMSEL,A,_NODECM
CMDEL,_NODECM

```

```

CMSEL,A,_ELEMCM
CMDEL,_ELEMCM
CMSEL,S,_KPCM
CMDEL,_KPCM
CMSEL,S,_LINECM
CMDEL,_LINECM
CMSEL,S,_AREACM
CMDEL,_AREACM
CMSEL,S,_VOLUCM
CMDEL,_VOLUCM
/GRES,cwz,gsav
CMDEL,_TARGET
CMDEL,_CONTACT
/COM, CONTACT PAIR CREATION - END

```

```

!---Contact pair 2(indenter-shell)--- (This section needs to be updated if geometry and meshing changes)
!The contact is assumed frictionless and the element types used are TARGE169, CONTA172
!The contact between indenter and shell is done using a pilot node on the indenter that
!will be used later to control the displacement during the simulation.

```

```

/COM, CONTACT PAIR CREATION - START

```

```

CM,_NODECM,NODE
CM,_ELEMCM,ELEM
CM,_KPCM,KP
CM,_LINECM,LINE
CM,_AREACM,AREA
CM,_VOLUCM,VOLU
/GSAV,cwz,gsav,,temp
MP,MU,1,0

```

```

MAT,1

```

```

R,4

```

```

REAL,4

```

```

ET,4,169

```

```

ET,5,172

```

```

KEYOPT,5,9,0

```

```

KEYOPT,5,10,2

```

```

R,4,

```

```

RMORE,

```

```

RMORE,,0

```

```

RMORE,0

```

```

! Generate the target surface

```

```

LSEL,S,,11

```

```

CM,_TARGET,LINE

```

```

TYPE,4

```

```

LATT,-1,4,4,-1

```

```

TYPE,4

```

```

LMESH,ALL

```

```

! Create a pilot node

```

```

N,28793, 0,50,0

```

```

TSHAP,PILO

```

```

E,28793

```

```

! Generate the contact surface

```

```

LSEL,S,,5

```

```

CM,_CONTACT,LINE

```



```

TYPE,5
NSLL,S,1
ESLN,S,0
ESURF
*SET,_REALID,4
ALLSEL
ESEL,ALL
ESEL,S,TYPE,,4
ESEL,A,TYPE,,5
ESEL,R,REAL,,4
LSEL,S,REAL,,4
/PSYMB,ESYS,1
/PNUM,TYPE,1
/NUM,1
EPLOT
/ZOOM,1,SCRN,-0.392143,0.869231,-0.345978,0.715385
ESEL,ALL
ESEL,S,TYPE,,4
ESEL,A,TYPE,,5
ESEL,R,REAL,,4
LSEL,S,REAL,,4
CMSEL,A,_NODECM
CMDEL,_NODECM
CMSEL,A,_ELEMCM
CMDEL,_ELEMCM
CMSEL,S,_KPCM
CMDEL,_KPCM
CMSEL,S,_LINECM
CMDEL,_LINECM
CMSEL,S,_AREACM
CMDEL,_AREACM
CMSEL,S,_VOLUCM
CMDEL,_VOLUCM
/GRES,cwz,gsav
CMDEL,_TARGET
CMDEL,_CONTACT
/COM, CONTACT PAIR CREATION - END

!*****Boundary conditions
!Main Menu>Preprocessor>Loads>Define Loads>Apply>Structural>Displacement>On Lines
!Boundary conditions for the substrate:
!The line corresponding to the base of the substrate (line 1), has displacement in x,
!in y and all rotations set to zero
!The line along x=0, due to axisymmetry, displacement in x is set to zero
DL,1, ,ALL,0
DL,4, ,UX,0
!Boundary condition for the Bubble Shell:
!The lines along x=0 (lines 14 and 15), due to axisymmetry, displacement in x is set to zero
FLST,2,2,4,ORDE,2
FITEM,2,14
FITEM,2,-15
!*
/GO

```

DL,P51X,UX,0

!\*\*\*\*\*Definition of the indentation depth for the simulation  
!The depths of indentations are defined on the pilot node.  
!The pilot node number needs to be updated here!  
!The displacement in x is set to zero, the displacement in Y is set to the maximum  
!displacement to be reached in the simulation.  
!The values vary for each case (as-assembled, calcined and sintered) and represent  
!the average maximum displacement to fracture observed experimentally.  
!The values are also different for nanoindentation simulations (with spherical indenter)  
!and in-situ compression simulations (with flat indenter)  
!As-assembled nanoindentation (spherical indenter): depth = 3.8um  
D,28793,0,,UX,,,,,  
D,28793,-3.8,,UY,,,,,  
!As-assembled in-situ compression (flat indenter): depth = 2.723um  
!Calcined nanoindentation (spherical indenter): depth = 0.99um  
!Calcined in-situ compression (flat indenter): depth = 1.933um  
!Sintered nanoindentation (spherical indenter): depth = 2.8um  
!Sintered in-situ compression (flat indenter): depth = 2.8um (this value is the same as  
!nanoindentation value, since we could not test this bubbles under in-situ)

!\*\*\*\*\*Solution Controls and Solve  
!The analysis used is non-linear and allows for large deformations.  
FINISH  
/SOL  
ANTYPE,0 !Static analysis  
NLGEOM,1 !Non linear  
DELTIM,1e-5,1e-8,0.1  
OUTRES,ERASE  
OUTRES,ALL,ALL !recording conditions  
TIME,1 !time  
  
SAVE  
SOLVE

## A1.2 Three Dimensional FEA with Von Mises Material Model

```
/config,NRES,10000      !Increase the total number of substeps from 1000(default) to 10000
/PREP7
```

```
!This file contains the summary of 3D simulations using Von Mises Material Model performed for
!the study, which results are included in the paper:
```

```
!Brugarolas, T.; Gianola, D. S.; Zhang, L.; Campbell, G. M.; Bassani, J. L.; Feng, G.; Lee, D.,
!"Tailoring and Understanding the Mechanical Properties of Nanoparticle-Shelled Bubbles.
!ACS Applied Materials & Interfaces 2014. with DOI: 10.1021/am502290h
!
```

```
!This simulations is done for:
```

```
! - As-assembled, calcined and sintered
! - Variation on the mechanical properties of bubbles (Young's Modulus, yield strength,...)
! - Variation on the average diameter and shell thickness for the different cases
! - Uniform shells
! - Flat indenter
! - Assuming an ideal initial state in which there are not deformations and the initial
!state of stress is null
! - Using Von Mises Material Model
```

```
!*****Element type: 3D solid 187
```

```
ET,1,SOLID187      ! Solid187 is a 10-node element that has a quadratic displacement
!behavior, well suited to modeling irregular meshes and with capability for large deflections
!and strains.
```

```
!*****Material properties of the bubble shell material:
```

```
!3D problem does not include substrate
```

```
!As-assembled bubbles: E = 6.8642077e-3 N/um^2 = 6.8642077 GPa;
```

```
!sigmaY = 0.1175610e-3 N/um^2 = 117.5610 MPa
```

```
!Poisson ratio assumed:  $\nu = 0.18$ 
```

```
!For as-assembled bubbles the material properties are input as follows (elastic-perfectly
!plastic material, tang=0):
```

```
MPTEMP,,,,,,,,
```

```
MPTEMP,1,0
```

```
MPDATA,EX,1,,6.8642077e-3      !N/um^2
```

```
MPDATA,PRXY,1,,0.18
```

```
TB,BISO,1,1,2,
```

```
TBTEMP,0
```

```
TBDATA,,0.1175610e-3,0,,,
```

```
!Calcined bubbles (700C): E = 13.6802611e-3 !N/um^2 ; also used E = 20GPa
```

```
!Sintered bubbles (1200C): E = 75.9861953e-3 !N/um^2
```

```
!Poisson ratio assumed:  $\nu = 0.18$ 
```

```
!For calcined and sintered bubbles the material properties are input as follows since the
!material is perfect elastic:
```

```
!MPTEMP,,,,,,,,
```

```
!MPTEMP,1,0
```

```
!MPDATA,EX,1,,13.6802611e-3 !N/um^2 This value needs to be updated to the corresponding E
```

```
!MPDATA,PRXY,1,,0.18
```

```

!*****Geometry of the Bubble
!Problem designed by applying symmetries. Only an 8th of a bubble shell is drawn.
!Define an eight of a shell
PCIRC,20.3,17.4,0,90,    !variables are outer radius, inner radius, from angle -90 to 90
!For calcined bubble:
!PCIRC,18.9,16.2,0,90,
!For sintered bubble:
!PCIRC,17.3,14.7,0,90,
!Define two key points on the Y axis for revolving purposes.
K, 5, 0, 0, 0 ! Defines key point number 5
K, 6, 0, 20.3, 0 ! Defines key point number 6
!For calcined bubble:
!K, 6, 0, 18.9, 0
!For sintered bubble:
!K, 6, 0, 17.3, 0
!Revolve the area (Main Menu>Preprocessor>Operate>Extrude>Areas>About Axis)
FLST,2,1,5,ORDE,1
FITEM,2,1
FLST,8,2,3
FITEM,8,6
FITEM,8,5
VROTAT,P51X, , , , ,P51X, ,90, ,    !!Positive Z axis, 1st quadrant

```

```

!*****Geometry of Indentor
!All 3D simulations are done using flat indenter (other shape indenters can be used)
!For as-assembled bubble:
K, 15, 0, 25, 20.3 !Defines key point number 15
K, 16, 25, 25, 20.3 !Defines key point number 16
K, 17, 25, -25, 20.3 !Defines key point number 17
K, 18, 0, -25, 20.3 !Defines key point number 18
!For calcined bubble:
!K, 15, 0, 25, 18.9 !Defines key point number 15
!K, 16, 25, 25, 18.9 !Defines key point number 16
!K, 17, 25, -25, 18.9 !Defines key point number 17
!K, 18, 0, -25, 18.9 !Defines key point number 18
!For sintered bubble:
!K, 15, 0, 25, 17.3 !Defines key point number 15
!K, 16, 25, 25, 17.3 !Defines key point number 16
!K, 17, 25, -25, 17.3 !Defines key point number 17
!K, 18, 0, -25, 17.3 !Defines key point number 18
!
FLST,2,4,3
FITEM,2,15
FITEM,2,16
FITEM,2,17
FITEM,2,18
A,P51X

```

```

!*****Material attribution to shell before meshing
!Attribution of material properties 1, to shell
CM,_Y,VOLU
VSEL, , , , 1
CM,_Y1,VOLU

```

```

CMSEL,S,_Y
!*
CMSEL,S,_Y1
VATT, 1, , 1, 0
CMSEL,S,_Y
CMDELE,_Y
CMDELE,_Y1

!*****Meshing of the shell
!The meshing of the shell is done by selecting lines 5, 30 and 40 and indicating
!the divisions that each of those lines composing the shell should have
FLST,5,3,4,ORDE,3
FITEM,5,2
FITEM,5,4
FITEM,5,7
CM,_Y,LINE
LSEL, , , ,P51X
CM,_Y1,LINE
CMSEL,,_Y
!*
LESIZE,_Y1, , ,5, , , , ,1
!*
FLST,5,3,4,ORDE,3
FITEM,5,3
FITEM,5,6
FITEM,5,9
CM,_Y,LINE
LSEL, , , ,P51X
CM,_Y1,LINE
CMSEL,,_Y
!*
LESIZE,_Y1, , ,30, , , , ,1
!*
FLST,5,3,4,ORDE,3
FITEM,5,1
FITEM,5,5
FITEM,5,8
CM,_Y,LINE
LSEL, , , ,P51X
CM,_Y1,LINE
CMSEL,,_Y
!*
LESIZE,_Y1, , ,40, , , , ,1
!*
!Mesh volume according to division of the lines.
!The mesh has more than 30000 nodes and 19000 elements, with at least 4 elements radially
!spanning from the inner shell surface to the outer surface.
CM,_Y,VOLU
VSEL, , , , 1
CM,_Y1,VOLU
CHKMSH,'VOLU'
CMSEL,S,_Y
!*

```

```

VMESH,_Y1
!*
CMDELE,_Y
CMDELE,_Y1
CMDELE,_Y2
!*

!*****Contact between shell and indenter
!--Contact pair (indenter-shell)--- (This section needs to be updated if geometry and meshing changes)
!The indenter is assumed rigid and the contact with the half bubble shell is assumed frictionless.
!The element types used for the contact between indenter and substrate are TARGE170 and CONTA174.
!The contact between indenter and shell is done using a pilot node on the indenter that
!will be used later to control the displacement during the simulation.
/COM, CONTACT PAIR CREATION - START
CM,_NODECM,NODE
CM,_ELEMCM,ELEM
CM,_KPCM,KP
CM,_LINECM,LINE
CM,_AREACM,AREA
CM,_VOLUCM,VOLU
/GSAV,cwz,gsav,,temp
MP,MU,1,
MAT,1
R,3
REAL,3
ET,2,170
ET,3,174
KEYOPT,3,9,0
KEYOPT,3,10,2
R,3,
RMORE,
RMORE,,0
RMORE,0
! Generate the target surface
ASEL,S,,,6
CM,_TARGET,AREA
AATT,-1,3,2,-1
TYPE,2
AMESH,ALL
! Create a pilot node
N,30357, 0,0,25
TSHAP,PILO
E,30357
! Generate the contact surface
ASEL,S,,,2
CM,_CONTACT,AREA
TYPE,3
NSLA,S,1
ESLN,S,0
NSLE,A,CT2 ! CZMESH patch (fsk qt-40109 8/2008)
ESURF
*SET,_REALID,3
ALLSEL

```

```

ESEL,ALL
ESEL,S,TYPE,,2
ESEL,A,TYPE,,3
ESEL,R,REAL,,3
ASEL,S,REAL,,3
/PSYMB,ESYS,1
/PNUM,TYPE,1
/NUM,1
EPlot
! Reverse target normals
ESEL,ALL
ESEL,S,TYPE,,2
ESEL,A,TYPE,,3
ESEL,R,REAL,,3
ASEL,S,REAL,,3
/PSYMB,ESYS,1
/PNUM,TYPE,1
/NUM,1
EPlot
! Reverse target normals
ESEL,ALL
ESEL,S,TYPE,,2
ESEL,A,TYPE,,3
ESEL,R,REAL,,3
ASEL,S,REAL,,3
/PSYMB,ESYS,1
/PNUM,TYPE,1
/NUM,1
EPlot
ESEL,ALL
ESEL,S,TYPE,,2
ESEL,A,TYPE,,3
ESEL,R,REAL,,3
ASEL,S,REAL,,3
CMSEL,A,_NODECM
CMDEL,_NODECM
CMSEL,A,_ELEMCM
CMDEL,_ELEMCM
CMSEL,S,_KPCM
CMDEL,_KPCM
CMSEL,S,_LINECM
CMDEL,_LINECM
CMSEL,S,_AREACM
CMDEL,_AREACM
CMSEL,S,_VOLUCM
CMDEL,_VOLUCM
/GRES,cwz,gsav
CMDEL,_TARGET
CMDEL,_CONTACT
/COM, CONTACT PAIR CREATION - END

```

```

!*****Boundary conditions
!Symmetry boundary conditions:

```

```

!Main Menu>Preprocessor>Loads>Define>Apply>Structural>Displacement>Symmetry B.C>OnAreas
DA, 5,SYMM !Mirror Symmetry (planar symmetry) on plane Y-Z
DA, 1,SYMM !Mirror Symmetry (planar symmetry) on plane X-Y
! Top node in shell not allowed to move in y direction, motion in X and Z need to be allowed
FLST,2,1,1,ORDE,1
FITEM,2,2
!*
/GO
D,P51X, ,0, , , ,UY, , , ,

!*****Definition of the indentation depth for the simulation
!The depths of indentations are defined on the pilot node.
!The pilot node number needs to be updated here!
!The displacement in x,y are set to zero, the displacement in Y is set to the maximum
!displacement to be reached in the simulation.
D,30357, ,0, , , ,UX,UY, , , ,
D,30357, ,-4.5, , , ,UZ, , , , ! b/c symmetry the total displacement is 9um
!As-assembled displacement of secondary crack = 9um
!Calcined displacement of secondary crack = 7um
!Sintered displacement of secondary crack = 12um (assumption since these bubbles were
!not experimentally fractured under in-situ)

!*****Solution Controls and Solve
!The analysis used is non-linear and allows for large deformations.
FINISH
/SOL
ANTYPE,0 !Static analysis
NLGEOM,1 !Non linear
DELTIM,1e-5,1e-8,0.1
OUTRES,ERASE
OUTRES,ALL,ALL !recording conditions
TIME,1 !time

SAVE
SOLVE

```



## A1.3 Three dimensional FEA with Drucker-Prager Material Model

```
/config,NRES,10000      !Increase the total number of substeps from 1000(default) to 10000
/PREP7
```

```
!This file contains the summary of 3D simulations using Drucker-Prager Material Model performed
!for the study, which results are included in the paper:
```

```
!Brugarolas, T.; Gianola, D. S.; Zhang, L.; Campbell, G. M.; Bassani, J. L.; Feng, G.; Lee, D.,
```

```
!"Tailoring and Understanding the Mechanical Properties of Nanoparticle-Shelled Bubbles.
```

```
!ACS Applied Materials & Interfaces 2014. with DOI: 10.1021/am502290h
```

```
!
```

```
!These simulations are done for:
```

```
! - As-assembled bubbles
```

```
! - Uniform shell
```

```
! - Flat indenter
```

```
! - Assuming an ideal initial state in which there are not deformations and the initial
```

```
!state of stress is null
```

```
! - Using Drucker-Prager Material Model
```

```
!*****Element type: 3D solid 65
```

```
ET,1,SOLID65      ! Solid65 brick like element defined by 8 nodes having 3 degrees of
```

```
!freedom at each node: translations in the nodal x, y, and z directions.
```

```
!*****Material properties of the bubble shell material:
```

```
!3D problem does not include substrate
```

```
!As-assembled bubbles: E = 6.8642077e-3 N/um^2 = 6.8642077 GPa;
```

```
!sigmaY = 0.1175610e-3 N/um^2 = 117.5610 MPa
```

```
!Poison ratio assumed:  $\nu = 0.18$ 
```

```
!For as-assembled bubbles the material properties are input as follows (elastic-perfectly
!plastic material, tang=0):
```

```
!Using a Drucker-Prager material, cohesion value, and frictional angle are also inputs.
```

```
!(the input parameters for the DP model are calculated as explained in the paper)
```

```
MPTEMP,,,,,,,,
```

```
MPTEMP,1,0
```

```
MPDATA,EX,1,,6.8642077e-3
```

```
MPDATA,PRXY,1,,0.18
```

```
TB,DP,1,,
```

```
TBMODIF,1,1,0.0000394732785257507
```

```
TBMODIF,1,2,22.2343595013517
```

```
TBMODIF,1,3,22.2343595013517
```

```
!*****Geometry of the Bubble
```

```
!Problem designed by applying symmetries. Only an 8th of a bubble shell is drawn.
```

```
!Define an eight of a shell
```

```
PCIRC,20.3,17.4,0,90,      !variables are outer radius, inner radius, from angle -90 to 90
```

```
!Define two key points on the Y axis for revolving purposes.
```

```
K, 5, 0, 0, 0 !Defines key point number 5
```

```
K, 6, 0, 20.3, 0 !Defines key point number 6
```

```
!Revolve the area (Main Menu>Preprocessor>Operate>Extrude>Areas>About Axis)
```

```
FLST,2,1,5,ORDE,1
```

```

FITEM,2,1
FLST,8,2,3
FITEM,8,6
FITEM,8,5
VROTAT,P51X, , , ,P51X, ,90, ,    !!Positive Z axis, 1st quadrant

!*****Geometry of Indentor
!All 3D simulations are done using flat indenter (other shape indenters can be used)
!For as-assembled bubble:
K, 15, 0, 25, 20.3 !Defines key point number 15
K, 16, 25, 25, 20.3 !Defines key point number 16
K, 17, 25, -25, 20.3 !Defines key point number 17
K, 18, 0, -25, 20.3 !Defines key point number 18
FLST,2,4,3
FITEM,2,15
FITEM,2,16
FITEM,2,17
FITEM,2,18
A,P51X

!*****Material attribution to shell before meshing
!Attribution of material properties 1, to shell
CM,_Y,VOLU
VSEL, , , , 1
CM,_Y1,VOLU
CMSEL,S,_Y
!*
CMSEL,S,_Y1
VATT, 1, , 1, 0
CMSEL,S,_Y
CMDELE,_Y
CMDELE,_Y1

!*****Meshing of the shell
!The meshing of the shell is done by selecting lines and indicating
!the divisions that each of those lines composing the shell should have
FLST,5,3,4,ORDE,3
FITEM,5,2
FITEM,5,4
FITEM,5,7
CM,_Y,LINE
LSEL, , , ,P51X
CM,_Y1,LINE
CMSEL,,_Y
!*
LESIZE,_Y1, , ,7, , , ,1
!!*
FLST,5,3,4,ORDE,3
FITEM,5,3
FITEM,5,6
FITEM,5,9
CM,_Y,LINE
LSEL, , , ,P51X

```

```

CM,_Y1,LINE
CMSEL,_,Y
!*
LESIZE,_Y1, , ,60, , , ,1
!*
FLST,5,3,4,ORDE,3
FITEM,5,1
FITEM,5,5
FITEM,5,8
CM,_Y,LINE
LSEL, , , ,P51X
CM,_Y1,LINE
CMSEL,_,Y
!*
LESIZE,_Y1, , ,70, , , ,1
!*
!Mesh volume according to division of the lines.
!The mesh has more than 30000 nodes and 19000 elements, with at least 4 elements radially
!spanning from the inner shell surface to the outer surface.
CM,_Y,VOLU
VSEL, , , , 1
CM,_Y1,VOLU
CHKMSH,'VOLU'
CMSEL,S,_Y
!*
VMESH,_Y1
!*
CMDELE,_Y
CMDELE,_Y1
CMDELE,_Y2

!*****Contact between shell and indenter
!--Contact pair (indenter-shell)--- (This section needs to be updated if geometry and meshing changes)
!The indenter is assumed rigid and the contact with the half bubble shell is assumed frictionless.
!The element types used for the contact between indenter and substrate are TARGE170 and CONTA174.
!The contact between indenter and shell is done using a pilot node on the indenter that
!will be used later to control the displacement during the simulation.
/COM, CONTACT PAIR CREATION - START
CM,_NODECM,NODE
CM,_ELEMCM,ELEM
CM,_KPCM,KP
CM,_LINECM,LINE
CM,_AREACM,AREA
CM,_VOLUCM,VOLU
/GSAV,cwz,gsav,.,temp
MP,MU,1,
MAT,1
MP,EMIS,1,7.88860905221e-031
R,3
REAL,3
ET,2,170
ET,3,174
R,3,,1.0,0.1,0,

```

```

RMORE,,,1.0E20,0.0,1.0,
RMORE,0.0,0,1.0,,1.0,0.5
RMORE,0,1.0,1.0,0.0,,1.0
KEYOPT,3,4,0
KEYOPT,3,5,0
KEYOPT,3,7,0
KEYOPT,3,8,0
KEYOPT,3,9,0
KEYOPT,3,10,2
KEYOPT,3,11,0
KEYOPT,3,12,0
KEYOPT,3,5,1
KEYOPT,3,2,0
KEYOPT,2,1,0
KEYOPT,2,2,0
KEYOPT,2,3,0
KEYOPT,2,5,1
! Generate the target surface
ASEL,S,,,6
CM,_TARGET,AREA
AATT,-1,3,2,-1
TYPE,2
AMESH,ALL
! Create a pilot node
N,30277, 0,0,25
TSHAP,PILO
E,30277
! Generate the contact surface
ASEL,S,,,2
CM,_CONTACT,AREA
TYPE,3
NSLA,S,1
ESLN,S,0
NSLE,A,CT2 ! CZMESH patch (fsk qt-40109 8/2008)
ESURF
*SET,_REALID,3
ALLSEL
ESEL,ALL
ESEL,S,TYPE,,2
ESEL,A,TYPE,,3
ESEL,R,REAL,,3
ASEL,S,REAL,,3
/PSYMB,ESYS,1
/PNUM,TYPE,1
/NUM,1
EPLOT
ESEL,ALL
ESEL,S,TYPE,,2
ESEL,A,TYPE,,3
ESEL,R,REAL,,3
ASEL,S,REAL,,3
CMSEL,A,_NODECM
CMDEL,_NODECM

```

```

CMSEL,A,_ELEMCM
CMDEL,_ELEMCM
CMSEL,S,_KPCM
CMDEL,_KPCM
CMSEL,S,_LINECM
CMDEL,_LINECM
CMSEL,S,_AREACM
CMDEL,_AREACM
CMSEL,S,_VOLUCM
CMDEL,_VOLUCM
/GRES,cwz,gsav
CMDEL,_TARGET
CMDEL,_CONTACT
/COM, CONTACT PAIR CREATION - END

```

CNCHECK,AUTO !It is highly recommended to use the auto contact setting option by issuing !CNCHECK,AUTO command for this problem in order to achieve better convergence.

```

!*****Boundary conditions
!Symmetry boundary conditions:
!Main Menu>Preprocessor>Loads>Define>Apply>Structural>Displacement>Symmetry B.C>OnAreas
DA, 5,SYMM !Mirror Symmetry (planar symmetry) on plane Y-Z
DA, 1,SYMM !Mirror Symmetry (planar symmetry) on plane X-Y
!No y motion in bottom out node between symmetries
FLST,2,1,3,ORDE,1
FITEM,2,2
!*
/GO
DK,P51X, ,0, ,0,UY, , , , ,

```

```

!*****Definition of the indentation depth for the simulation
!The depths of indentations are defined on the pilot node.
!The pilot node number needs to be updated here!
!The displacement in x,y are set to zero, the displacement in Y is set to the maximum
!displacement to be reached in the simulation.
D,30277, ,0, , , ,UX,UY, , , ,
D,30277, ,-4.5, , , ,UZ, , , , , ! b/c symmetry the total displacement is 9um
!As-assembled displacement of secondary crack = 9um

```

```

!*****Solution Controls and Solve
!The analysis used is non-linear and allows for large deformations.
FINISH
/SOL
ANTYPE,0 !Static analysis
NLGEOM,1 !Non linear
DELTIM,1e-5,1e-8,0.1
OUTRES,ERASE
OUTRES,ALL,ALL !recording conditions
TIME,1 !time

SAVE
SOLVE

```

## Appendix 2. Supplemental Results

Additional experiments are performed to corroborate the results shown in Chapter 5, in which it is observed that differences in the nanoscale structure of the shells calcined – rough and porous– and sintered –smooth and non-porous– bubbles greatly affects the behavior of the composites containing these types of bubbles. To provide a better understanding, a new set of experiments are performed. All experiments described in this Appendix are based on the Experimental Section described in Chapter 5.

In this case, the microfluidic generation of nanoparticle-shelled bubbles is run for 6-7 hours to increase the throughput, yielding up to a resulting volume of approx. 5 ml of dried bubbles. The bubbles generated from the microfluidic technique are washed and divided in 5 parts and placed in different crucibles after the excess water is removed. The bubbles are dried in open air conditions at room temperature. The crucibles containing the dried bubbles are then ready for thermal treatments at different temperatures: no thermal treatment (as-assembled), treated at 700, 850, 1000, and 1150 °C. The thermal treatments on the bubbles are done similarly to the previously explained methods (see Chapter 5). After the thermal treatments the bubbles are transferred to eppendorf tubes and vortexed to assist the detachment of bubbles forming clusters. Bubbles treated at higher temperatures (1000, and 1150 °C) are more likely to form clusters and be more difficult to disperse. We believe this is due to the fact that sintering is taking place at high temperatures and bubbles or small debris are melting together during the process. After

vortexing all bubbles –as-assembled, 700, 850, 1000, and 1150– are detached and free flowing inside the tubes. At this point, the bubbles are characterized.

The density of the bubbles is approximated by measuring the tapped density of the dried bubbles and assuming a random close packing (packing fraction of 0.64). As we have previously observed (see Chapter 3), thermal treatment densifies the bubble shells. Previously we observed a slight decrease in bubble diameter and shell thickness. We also observed that the porosity of the shell is reduced until the shell is non-porous when sintered at 1200 °C. The bubble density is shown in Figure A2.1a

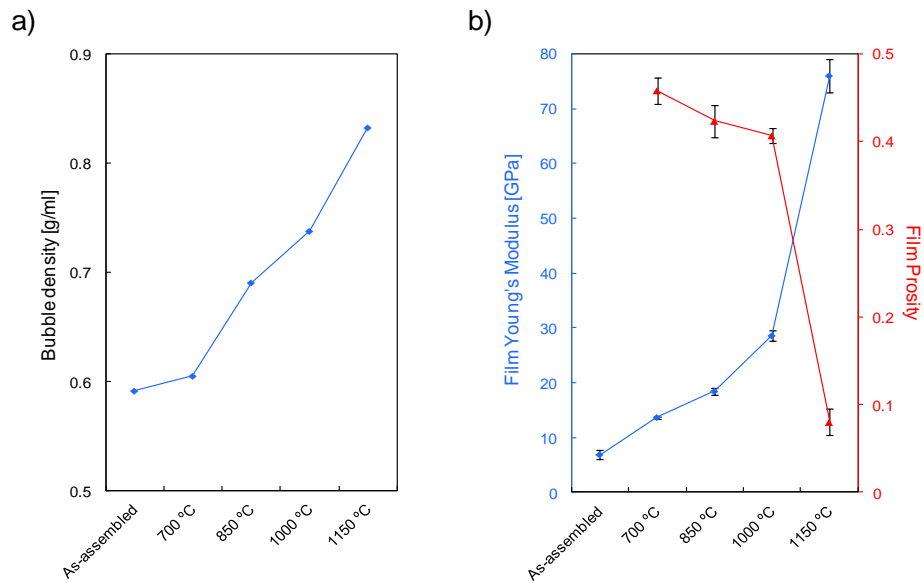


**Figure A2.1** (a) Bubble density approximated from the measured tapped density of dried bubbles and assuming a random close packing. (b) Young's modulus and porosity of nanoparticle films subjected to the same thermal treatments than the bubbles.

In Chapter 3 and 4 the characterization of the bubble shells were approximated by nanoparticle films deposited onto a Si or quartz substrate, which allows the measurement of the porosity using ellipsometry and the determination of the hardness, elastic modulus

and yield strength with nanoindentation (at small indentation depths between 40-100nm). Similarly, in this study, additional nanoparticle films are prepared on quartz substrates and treated thermally at 850 and 1000 °C. The porosity values and Young's modulus are plotted in Figure A2.1b. Consistent with our previous results, the porosity of the films decreases until it shows a lack of porosity when the films are thermally treated above 1150 °C. Also, the Young's moduli of the films increases at higher temperature treatments reaching an order of magnitude higher between as-assembled films and films treated at 1150 °C.

These changes in the bubble geometry and structure have a great impact on the mechanical properties of the bubbles, as shown in the summary of the mechanical characterization in Section 3.3.4 of this thesis, in which we compared as-assembled bubbles, calcined bubbles treated at 700 °C and sintered bubbles treated at 1200 °C. The strength and stiffness of the bubbles are highly increased upon sintering. As-assembled bubbles exhibit an inelastic response with significant plasticity afforded by the organic materials in the bubble shell. While the deformability of calcined bubbles is diminished due to the loss of organics, the deformability of sintered bubbles is close to that of as-assembled bubbles owing to the largely enhanced elastic range.

These bubbles can be incorporated into composites, similarly to the way described in Chapter 5. Two different weight fractions of bubbles are used for the composite preparation (20 wt% and 30 wt%) with as-assembled, 700, 850, 1000 and 1150 bubbles and UV-curable polyurethane-acrylate. See experimental section of Chapter 5 for the description of the composite preparation and characterization.



The density of the composites is shown in Figure A2.2. The incorporation of bubbles decreases the density of the composite. The samples containing a 30wt% of bubbles display a lower density than the ones containing 20wt% of bubbles. The density of the composite samples increases when the bubbles used are treated at higher temperatures, due to the densification of the bubble; the individual bubbles are denser (see Figure A2.1a) therefore the same weight fraction results in higher density of composite samples. The mixing of the bubbles and the polymer during the composite generation unavoidably traps air in the composite sample. Knowing the density of the bubbles and the polymer, the weight fraction of bubbles and the density of the composite, the void content can be approximated, resulting in an 8-14 vol% similarly to what others have observed.<sup>118</sup>

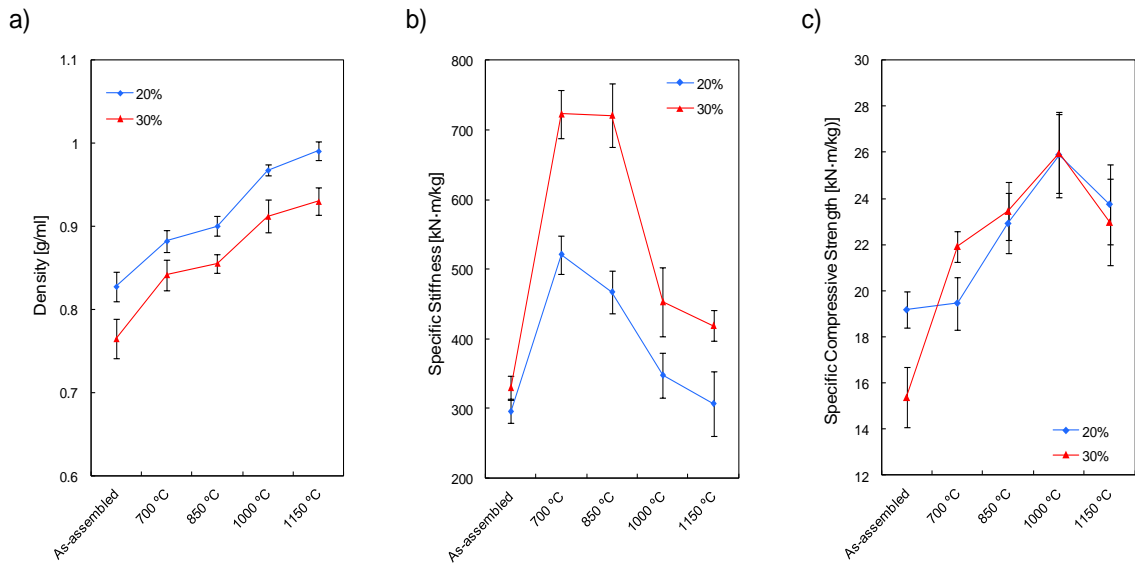


**Figure A2.2** (a) Density, (b) specific stiffness, and (c) specific compressive strength of composite samples made with as-assembled, 700, 850, 1000 and 1150 °C bubbles at 20 and 30 weight fraction of bubbles.

The composite samples containing the different thermally treated bubbles are then tested under compression, and their mechanical characterization is analyzed in terms of their specific properties (similarly to Chapter 5). Special considerations are taken during the mechanical testing of these samples to compression to avoid any friction effects affecting the results. Lubricant was added on the substrate and the indenter previous to the mechanical compression in 2 of the 7 or 8 samples tested in each case, showing no differences in the results.

The mechanical properties of these composites display some striking results. The specific stiffness (and the specific compressive strength) first increases to a maximum for the 700-850 °C bubbles (1000 °C bubbles) but it then drops notably for the 1150 °C bubbles (see Figure A2.2b and c). The specific stiffness and the specific compressive strength of these composites do not follow the trends observed for individual bubbles. Bubbles are stiffer and stronger when treated at higher temperatures but the composites that contain them are less stiff and strong than the ones containing bubbles treated at lower temperatures. The nanostructure of bubbles treated at high and medium temperatures are very different, smooth and non-porous vs. rough and porous respectively. The nanostructure differences, the lack of porosity and roughness, seem to be the responsible of the weakened stiffness and strength of the 1150 °C bubbles. The strain at peak and the toughness of the composites is shown in Figure A2.3. Similarly to the specific stiffness and strength, 1150 °C bubbles present a lower strain at peak and specific toughness than 1000 °C bubbles, that can also be attributed to the nanostructure differences.

It is interesting to note that the peak strain and the specific toughness present a high value for as-assembled bubbles compared to the thermally treated ones. As previously mentioned as-assembled bubbles present an inelastic behavior with significant plasticity afforded by the organic materials in the bubble shell (see Chapters 3 and 4). This plasticity that characterizes as-assembled bubbles seems to be the responsible of the enhanced toughness and strain at peak.

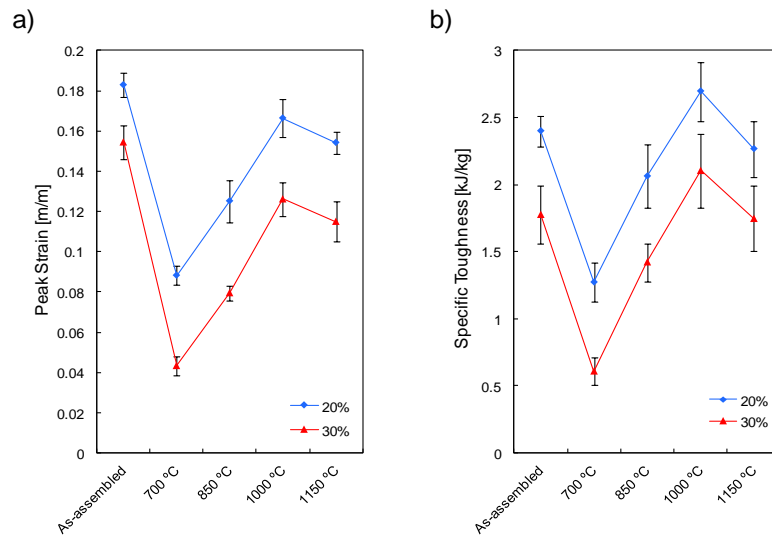


**Figure A2.3** (a) Strain at peak and (b) specific toughness of composite samples containing as-assembled, 700, 850, 1000 and 1150 °C bubbles at 20 and 30 weight fraction of bubbles.

This additional set of tests supports the hypothesis presented in Chapter 5. The use of the same initial bubbles for the thermal treatment and further composite generation allows us to neglect geometrical factors in the understanding of the mechanical differences observed. In addition, the use of thermal treatments at temperatures between 700 and 1150 °C allows us to better understand the structure-property relationship. We observe that the nanostructure plays a critical role not only on the mechanical behavior of

single bubbles but also it has an important effect on the properties of composites. In some cases, the contribution of the interface is more decisive than the mechanical properties of the fillers forming the composite. We believe the nanostructure of the shelled bubbles, the roughness and porosity of 700-1000 °C, is a critical factor that enhances the mechanical response of composites by means of improving the interfacial strength between the shelled-bubbles and the polymeric matrix.

# Bibliography

1. Blackert, P.; Compston, P. In *Application of Advanced Lightweight Materials for Optimisation of Function and Weight in Vehicle Platforms*, Proceedings ICED 05, the 15th International Conference on Engineering Design, **2005**.
2. Rostami, H.; Brooks, R.; Tovia, F.; Bahador, M., Development of Lightweight Construction Material from Alkali Activated Fly Ash. *Journal of Solid Waste Technology and Management* **2009**, 35 (3), 127-134.
3. Fleck, N. A.; Deshpande, V. S.; Ashby, M. F., Micro-Architected Materials: Past, Present and Future. *Proceedings of the Royal Society A: Mathematical, Physical and Engineering Science* **2010**, 466 (2121), 2495-2516.
4. Patankar, S. N.; Kranov, Y. A., Hollow Glass Microsphere Hdpe Composites for Low Energy Sustainability. *Mater. Sci. Eng., A* **2010**, 527 (6), 1361-1366.
5. John, B.; Nair, C. P. R., *Update on Syntactic Foams*. iSmithers Rapra Publishing: **2010**.
6. Kyung H. Moh, S. P. M. N.; Harold G. Sowman, S. P. M. N.; Thomas E. Wood, S. P. M. N. Sol Gel-Derived Ceramic Bubbles. US 5077241, **1991**.
7. Tagliavia, G.; Porfiri, M.; Gupta, N., Analysis of Flexural Properties of Hollow-Particle Filled Composites. *Composites Part B: Engineering* **2010**, 41 (1), 86-93.
8. Koopman, M.; Chawla, K. K.; Carlisle, K. B.; Gladysz, G. M., Microstructural Failure Modes in Three-Phase Glass Syntactic Foams. *Journal of Materials Science* **2006**, 41 (13), 4009-4014.
9. Gupta, N.; Woldesenbet, E.; Kishore, Compressive Fracture Features of Syntactic Foams-Microscopic Examination. *Journal of Materials Science* **2002**, 37 (15), 3199-3209.
10. Shah, R. K.; Shum, H. C.; Rowat, A. C.; Lee, D.; Agresti, J. J.; Utada, A. S.; Chu, L.-Y.; Kim, J.-W.; Fernandez-Nieves, A.; Martinez, C. J.; Weitz, D. A., Designer Emulsions Using Microfluidics. *Materials Today* **2008**, 11 (4), 18-27.
11. Ralf, S.; Martin, B.; Thomas, P.; Stephan, H., Droplet Based Microfluidics. *Reports on Progress in Physics* **2012**, 75 (1), 016601.

12. Lee, M. H.; Prasad, V.; Lee, D., Microfluidic Fabrication of Stable Nanoparticle-Shelled Bubbles. *Langmuir* **2009**, *26* (4), 2227-2230.
13. Lee, M. H.; Lee, D., Elastic Instability of Polymer-Shelled Bubbles Formed from Air-in-Oil-in-Water Compound Bubbles. *Soft Matter* **2010**, *6* (18), 4326-4330.
14. Brugarolas, T.; Park, B. J.; Lee, M. H.; Lee, D., Generation of Amphiphilic Janus Bubbles and Their Behavior at an Air–Water Interface. *Adv Funct Mater* **2011**, *21* (20), 3924-3931.
15. Yao, H.-B.; Fang, H.-Y.; Wang, X.-H.; Yu, S.-H., Hierarchical Assembly of Micro-/Nano-Building Blocks: Bio-Inspired Rigid Structural Functional Materials. *Chemical Society Reviews* **2011**, *40* (7), 3764-3785.
16. Park, J. I.; Nie, Z.; Kumachev, A.; Abdelrahman, A. I.; Binks, B. P.; Stone, H. A.; Kumacheva, E., A Microfluidic Approach to Chemically Driven Assembly of Colloidal Particles at Gas–Liquid Interfaces. *Angewandte Chemie International Edition* **2009**, *48* (29), 5300-5304.
17. Pancholi, K.; Stride, E.; Edirisinghe, M., Dynamics of Bubble Formation in Highly Viscous Liquids. *Langmuir* **2008**, *24* (8), 4388-4393.
18. Garstecki, P.; Gitlin, I.; DiLuzio, W.; Whitesides, G. M.; Kumacheva, E.; Stone, H. A., Formation of Monodisperse Bubbles in a Microfluidic Flow-Focusing Device. *Applied Physics Letters* **2004**, *85* (13), 2649-2651.
19. Dollet, B.; van Hoeve, W.; Raven, J.-P.; Marmottant, P.; Versluis, M., Role of the Channel Geometry on the Bubble Pinch-Off in Flow-Focusing Devices. *Physical Review Letters* **2008**, *100* (3), 034504.
20. Subramaniam, A. B.; Abkarian, M.; Stone, H. A., Controlled Assembly of Jammed Colloidal Shells on Fluid Droplets. *Nat Mater* **2005**, *4* (7), 553-556.
21. Unger, E. C.; Porter, T.; Culp, W.; Labell, R.; Matsunaga, T.; Zutshi, R., Therapeutic Applications of Lipid-Coated Microbubbles. *Advanced Drug Delivery Reviews* **2004**, *56* (9), 1291-1314.
22. Shen, H.; Forssberg, E.; Pugh, R. J., Selective Flotation Separation of Plastics by Chemical Conditioning with Methyl Cellulose. *Resources, Conservation and Recycling* **2002**, *35* (4), 229-241.

23. Liu, Y.; Miyoshi, H.; Nakamura, M., Encapsulated Ultrasound Microbubbles: Therapeutic Application in Drug/Gene Delivery. *Journal of Controlled Release* **2006**, *114* (1), 89-99.
24. Klibanov, A., Preparation of Targeted Microbubbles: Ultrasound Contrast Agents for Molecular Imaging. *Medical and Biological Engineering and Computing* **2009**, *47* (8), 875-882.
25. Grainger, S. J.; Serna, J. V.; Sunny, S.; Zhou, Y.; Deng, C. X.; El-Sayed, M. E. H., Pulsed Ultrasound Enhances Nanoparticle Penetration into Breast Cancer Spheroids. *Molecular Pharmaceutics* **2010**, *7* (6), 2006-2019.
26. Stride, E.; Edirisinghe, M., Novel Microbubble Preparation Technologies. *Soft Matter* **2008**, *4* (12), 2350-2359.
27. Walther, A.; Muller, A. H. E., Janus Particles. *Soft Matter* **2008**, *4* (4), 663-668.
28. McConnell, M. D.; Kraeutler, M. J.; Yang, S.; Composto, R. J., Patchy and Multiregion Janus Particles with Tunable Optical Properties. *Nano Letters* **2010**, *10* (2), 603-609.
29. Lee, K. J.; Yoon, J.; Lahann, J., Recent Advances with Anisotropic Particles. *Current Opinion in Colloid & Interface Science* **2010**, *In Press, Corrected Proof*.
30. Ku, J.; Aruguete, D. M.; Alivisatos, A. P.; Geissler, P. L., Self-Assembly of Magnetic Nanoparticles in Evaporating Solution. *Journal of the American Chemical Society* **2011**, *133* (4), 838-848.
31. Kim, J.-W.; Lee, D.; Shum, H. C.; Weitz, D. A., Colloid Surfactants for Emulsion Stabilization. *Advanced materials* **2008**, *20* (17), 3239-3243.
32. Jiang, S.; Granick, S., Janus Balance of Amphiphilic Colloidal Particles. *The Journal of Chemical Physics* **2007**, *127* (16), 161102-4.
33. Jiang, H.-R.; Yoshinaga, N.; Sano, M., Active Motion of a Janus Particle by Self-Thermophoresis in a Defocused Laser Beam. *Physical Review Letters* **2010**, *105* (26), 268302.
34. Gangwal, S.; Pawar, A.; Kretzschmar, I.; Velev, O. D., Programmed Assembly of Metallo-dielectric Patchy Particles in External Ac Electric Fields. *Soft Matter* **2010**, *6* (7), 1413-1418.

35. Cui, J.-Q.; Kretzschmar, I., Surface-Anisotropic Polystyrene Spheres by Electroless Deposition. *Langmuir* **2006**, *22* (20), 8281-8284.
36. Chen, Q.; Whitmer, J. K.; Jiang, S.; Bae, S. C.; Luijten, E.; Granick, S., Supracolloidal Reaction Kinetics of Janus Spheres. *Science* **2011**, *331* (6014), 199-202.
37. Howse, J. R.; Jones, R. A. L.; Ryan, A. J.; Gough, T.; Vafabakhsh, R.; Golestanian, R., Self-Motile Colloidal Particles: From Directed Propulsion to Random Walk. *Physical Review Letters* **2007**, *99* (4), 048102.
38. Walther, A.; Hoffmann, M.; Müller, A. H. E., Emulsion Polymerization Using Janus Particles as Stabilizers. *Angewandte Chemie International Edition* **2008**, *47* (4), 711-714.
39. Binks, B. P.; Fletcher, P. D. I., Particles Adsorbed at the Oil–Water Interface: A Theoretical Comparison between Spheres of Uniform Wettability and “Janus” Particles. *Langmuir* **2001**, *17* (16), 4708-4710.
40. Leroy, V.; Bretagne, A.; Fink, M.; Willaime, H.; Tabeling, P.; Tourin, A., Design and Characterization of Bubble Phononic Crystals. *Applied Physics Letters* **2009**, *95* (17), 171904-3.
41. de Gennes, P. G., Soft Matter. *Reviews of Modern Physics* **1992**, *64* (3), 645.
42. Paunov, V. N.; Cayre, O. J., Supraparticles and “Janus” Particles Fabricated by Replication of Particle Monolayers at Liquid Surfaces Using a Gel Trapping Technique. *Advanced materials* **2004**, *16* (9-10), 788-791.
43. Paunov, V. N., Novel Method for Determining the Three-Phase Contact Angle of Colloid Particles Adsorbed at Air–Water and Oil–Water Interfaces. *Langmuir* **2003**, *19* (19), 7970-7976.
44. Cayre, O. J.; Paunov, V. N., Contact Angles of Colloid Silica and Gold Particles at Air-Water and Oil-Water Interfaces Determined with the Gel Trapping Technique. *Langmuir* **2004**, *20* (22), 9594-9.
45. Ulman, A., Formation and Structure of Self-Assembled Monolayers. *Chemical Reviews* **1996**, *96* (4), 1533-1554.
46. Nuzzo, R. G.; Allara, D. L., Adsorption of Bifunctional Organic Disulfides on Gold Surfaces. *Journal of the American Chemical Society* **1983**, *105* (13), 4481-4483.



47. Love, J. C.; Estroff, L. A.; Kriebel, J. K.; Nuzzo, R. G.; Whitesides, G. M., Self-Assembled Monolayers of Thiolates on Metals as a Form of Nanotechnology. *Chemical Reviews* **2005**, *105* (4), 1103-1170.
48. Bain, C. D.; Troughton, E. B.; Tao, Y. T.; Evall, J.; Whitesides, G. M.; Nuzzo, R. G., Formation of Monolayer Films by the Spontaneous Assembly of Organic Thiols from Solution onto Gold. *Journal of the American Chemical Society* **1989**, *111* (1), 321-335.
49. Takei, H.; Shimizu, N., Gradient Sensitive Microscopic Probes Prepared by Gold Evaporation and Chemisorption on Latex Spheres. *Langmuir* **1997**, *13* (7), 1865-1868.
50. Stancik, E. J.; Fuller, G. G., Connect the Drops: Using Solids as Adhesives for Liquids. *Langmuir* **2004**, *20* (12), 4805-4808.
51. Reynaert, S.; Moldenaers, P.; Vermant, J., Control over Colloidal Aggregation in Monolayers of Latex Particles at the Oil-Water Interface. *Langmuir* **2006**, *22* (11), 4936-4945.
52. Bragg, L.; Nye, J. F., A Dynamical Model of a Crystal Structure. *Proceedings of the Royal Society of London. Series A, Mathematical and Physical Sciences* **1947**, *190* (1023), 474-481.
53. Casagrande, C.; Veysie, M., Janus Beads - Realization and 1st Observation of Interfacial Properties. *Comptes Rendus De L Academie Des Sciences Serie Ii* **1988**, *306* (20), 1423-1425.
54. Ondarcuhu, T.; Fabre, P.; Raphael, E.; Veysie, M., Specific Properties of Amphiphilic Particles at Fluid Interfaces. *J. Phys. France* **1990**, *51* (14), 1527-1536.
55. Pawar, A. B.; Kretzschmar, I., Multifunctional Patchy Particles by Glancing Angle Deposition. *Langmuir* **2009**, *25* (16), 9057-9063.
56. Conradi, M.; Ravnik, M.; Bele, M.; Zorko, M.; Zumer, S.; Musevic, I., Janus Nematic Colloids. *Soft Matter* **2009**, *5* (20), 3905-3912.
57. Stamou, D.; Duschl, C.; Johannsmann, D., Long-Range Attraction between Colloidal Spheres at the Air-Water Interface: The Consequence of an Irregular Meniscus. *Physical Review E* **2000**, *62* (4), 5263.

58. Kralchevsky, P. A.; Denkov, N. D.; Danov, K. D., Particles with an Undulated Contact Line at a Fluid Interface: Interaction between Capillary Quadrupoles and Rheology of Particulate Monolayers. *Langmuir* **2001**, *17* (24), 7694-7705.
59. Chan, D. Y. C.; Henry, J. D.; White, L. R., The Interaction of Colloidal Particles Collected at Fluid Interfaces. *Journal of Colloid and Interface Science* **1981**, *79* (2), 410-418.
60. Loudet, J. C.; Alsayed, A. M.; Zhang, J.; Yodh, A. G., Capillary Interactions between Anisotropic Colloidal Particles. *Physical Review Letters* **2005**, *94* (1), 4.
61. Brenner, H.; Leal, L. G., A Micromechanical Derivation of Fick's Law for Interfacial Diffusion of Surfactant Molecules. *Journal of Colloid and Interface Science* **1978**, *65* (2), 191-209.
62. Radoev, B.; Nedyalkov, M.; Dyakovich, V., Brownian Motion at Liquid-Gas Interfaces. 1. Diffusion Coefficients of Macroparticles at Pure Interfaces. *Langmuir* **1992**, *8* (12), 2962-2965.
63. Alonso, C.; Zasadzinski, J. A., Linear Dependence of Surface Drag on Surface Viscosity. *Physical Review E* **2004**, *69* (2), 021602.
64. Crocker, J. C.; Grier, D. G., Methods of Digital Video Microscopy for Colloidal Studies. *Journal of Colloid and Interface Science* **1996**, *179* (1), 298-310.
65. Park, B. J.; Brugarolas, T.; Lee, D., Janus Particles at an Oil-Water Interface. *Soft Matter* **2011**, *7* (14), 6413-6417.
66. Park, B. J.; Vermant, J.; Furst, E. M., Heterogeneity of the Electrostatic Repulsion between Colloids at the Oil-Water Interface. *Soft Matter* **2010**, *6* (21), 5327-5333.
67. Chen, W.; Tan, S.; Huang, Z.; Ng, T.-K.; Ford, W. T.; Tong, P., Measured Long-Ranged Attractive Interaction between Charged Polystyrene Latex Spheres at a Water-Air Interface. *Physical Review E* **2006**, *74* (2), 021406.
68. Cheung, D. L.; Bon, S. A. F., Stability of Janus Nanoparticles at Fluid Interfaces. *Soft Matter* **2009**, *5* (20), 3969-3976.
69. Rye, R. R.; Mann, J. A.; Yost, F. G., The Flow of Liquids in Surface Grooves. *Langmuir* **1996**, *12* (2), 555-565.

70. Romero, L. A.; Yost, F. G., Flow in an Open Channel Capillary. *Journal of Fluid Mechanics* **1996**, *322*, 109-129.
71. De Coninck, J.; Blake, T. D., Wetting and Molecular Dynamics Simulations of Simple Liquids. *Annual Review of Materials Research* **2008**, *38* (1), 1-22.
72. Rohatgi, P. K.; Gupta, N.; Weiss, D.; Miracle, D. In *Synthesis and Applications of Cast Metal Matrix Composites and Syntactic Foams*, **2006**.
73. Peter, S. L.; Mylavarapu, P.; Woldesenbet, E. In *High Strain Rate Properties of Nanoparticulate Syntactic Foams*, **2007**; pp 1916-1926.
74. Konka, H. P.; Wahab, M. A.; Lian, K. In *Sandwich Structures with Smart Composite Face Skin*, **2011**; pp 157-166.
75. Conover, D.; Nikolaus, R., Innovation and Unity in Advancing Ocean Sciences. *Sea Technology* **2013**, *54* (1), 19-20.
76. Ashby, M. F.; Gibson, L. J.; Wegst, U.; Olive, R., The Mechanical Properties of Natural Materials. I. Material Property Charts. *Proceedings: Mathematical and Physical Sciences* **1995**, *450* (1938), 123-140.
77. Wegst, U. G. K.; Ashby, M. F., The Mechanical Efficiency of Natural Materials. *Philosophical Magazine* **2004**, *84* (21), 2167-2186.
78. Jang, D.; Meza, L. R.; Greer, F.; Greer, J. R., Fabrication and Deformation of Three-Dimensional Hollow Ceramic Nanostructures. *Nat Mater* **2013**, *12* (10), 893-898.
79. Patankar, S. N.; Kranov, Y. A., Hollow Glass Microsphere Hdpe Composites for Low Energy Sustainability. *Materials Science and Engineering A: Structural Materials Properties Microstructure and Processing* **2010**, *527* (6), 1361-1366.
80. Fiedler, T.; Richards, H. S.; Belova, I. V.; Öchsner, A.; Murch, G. E., Experimental Analysis on the Thermal Anisotropy of Syntactic Hollow Sphere Structures. *Experimental Thermal and Fluid Science* **2013**, *44* (0), 637-641.
81. Grosjean, F.; Bouchonneau, N.; Choqueuse, D.; Sauvant-Moynot, V., Comprehensive Analyses of Syntactic Foam Behaviour in Deepwater Environment. *Journal of Materials Science* **2009**, *44* (6), 1462-1468.

82. Lee, J.-H.; Singer, J. P.; Thomas, E. L., Micro-/Nanostructured Mechanical Metamaterials. *Advanced materials* **2012**, *24* (36), 4782-4810.
83. Dombrovsky, L. A.; Randrianalisoa, J. H.; Baillis, D., Infrared Radiative Properties of Polymer Coatings Containing Hollow Microspheres. *International Journal of Heat and Mass Transfer* **2007**, *50* (7-8), 1516-1527.
84. Shunmugasamy, V. C.; Pinisetty, D.; Gupta, N., Thermal Expansion Behavior of Hollow Glass Particle/Vinyl Ester Composites. *Journal of Materials Science* **2012**, *47* (14), 5596-5604.
85. Colombo, P.; Degischer, H. P., Highly Porous Metals and Ceramics. *Materials Science and Technology* **2010**, *26* (10), 1145-1158.
86. Bunn, P.; Mottram, J. T., Manufacture and Compression Properties of Syntactic Foams. *Composites* **1993**, *24* (7), 565-571.
87. Gupta, N.; Kishore; Woldesenbet, E.; Sankaran, S., Studies on Compressive Failure Features in Syntactic Foam Material. *Journal of Materials Science* **2001**, *36* (18), 4485-4491.
88. Gupta, N., A Functionally Graded Syntactic Foam Material for High Energy Absorption under Compression. *Materials Letters* **2007**, *61* (4-5), 979-982.
89. Kallas, D. H.; Chatten, C. K., Buoyancy Materials for Deep Submergence. *Ocean Engineering* **1969**, *1* (4), 421-431.
90. Chen, Z.; Xu, C.; Ma, C.; Ren, W.; Cheng, H.-M., Lightweight and Flexible Graphene Foam Composites for High-Performance Electromagnetic Interference Shielding. *Advanced materials* **2013**, *25* (9), 1296-1300.
91. Göransson, P. In *Advanced Materials and Structures for Noise Control*, **2006**.
92. Tochizawa, M.; Tanaka, M. In *Development of Lightweight Single Bumper Shield*, **2003**; pp 3629-3635.
93. A New Concept for a Flexible Structure Composite Helmet. *JEC Composites Magazine* **2004**, (13), 52.

94. d'Almeida, J. R. M., An Analysis of the Effect of the Diameters of Glass Microspheres on the Mechanical Behavior of Glass-Microsphere/Epoxy-Matrix Composites. *Composites Science and Technology* **1999**, *59* (14), 2087-2091.
95. Garza-Cruz, T.; Nakagawa, M., On a Hybrid Method to Characterize the Mechanical Behavior of Thin Hollow Glass Microspheres. *Granular Matter* **2012**, *14* (3), 309-318.
96. Koopman, M.; Gouadec, G.; Carlisle, K.; Chawla, K. K.; Gladysz, G., Compression Testing of Hollow Microspheres (Microballoons) to Obtain Mechanical Properties. *Scripta Materialia* **2004**, *50* (5), 593-596.
97. Gladysz, G. M.; Perry, B.; McEachen, G.; Lula, J., Three-Phase Syntactic Foams: Structure-Property Relationships. *Journal of Materials Science* **2006**, *41* (13), 4085-4092.
98. Brugarolas, T.; Park, B. J.; Lee, M. H.; Lee, D., Generation of Amphiphilic Janus Bubbles and Their Behavior at an Air-Water Interface. *Adv Funct Mater* **2011**, *21* (20), 3924-3931.
99. Brugarolas, T.; Tu, F.; Lee, D., Directed Assembly of Particles Using Microfluidic Droplets and Bubbles. *Soft Matter* **2013**, *9* (38), 9046-9058.
100. Magagnosc, D. J.; Ehrbar, R.; Kumar, G.; He, M. R.; Schroers, J.; Gianola, D. S., Tunable Tensile Ductility in Metallic Glasses. *Sci. Rep.* **2013**, *3*.
101. Santhanam, V.; Andres, R. P., Microcontact Printing of Uniform Nanoparticle Arrays. *Nano Letters* **2003**, *4* (1), 41-44.
102. Silpe, J. E.; Nunes, J. K.; Poortinga, A. T.; Stone, H. A., Generation of Antibubbles from Core-Shell Double Emulsion Templates Produced by Microfluidics. *Langmuir* **2013**, *29* (28), 8782-8787.
103. Kotula, A. P.; Anna, S. L., Probing Timescales for Colloidal Particle Adsorption Using Slug Bubbles in Rectangular Microchannels. *Soft Matter* **2012**, *8* (41), 10759-10772.
104. Duncanson, W. J.; Abbaspourrad, A.; Shum, H. C.; Kim, S.-H.; Adams, L. L. A.; Weitz, D. A., Monodisperse Gas-Filled Microparticles from Reactions in Double Emulsions. *Langmuir* **2012**, *28* (17), 6742-6745.

105. Chen, H.; Li, J.; Wan, J.; Weitz, D. A.; Stone, H. A., Gas-Core Triple Emulsions for Ultrasound Triggered Release. *Soft Matter* **2013**, *9* (1), 38-42.
106. Tumarkin, E.; Park, J. I.; Nie, Z.; Kumacheva, E., Temperature Mediated Generation of Armoured Bubbles. *Chemical Communications* **2011**, *47* (47), 12712-12714.
107. Yang, L.; Wang, K.; Mak, S.; Li, Y.; Luo, G., A Novel Microfluidic Technology for the Preparation of Gas-in-Oil-in-Water Emulsions. *Lab on a Chip* **2013**, *13* (17), 3355-3359.
108. Lankveld, J. M. G.; Lyklema, J., Adsorption of Polyvinyl Alcohol on the Paraffin—Water Interface. I. Interfacial Tension as a Function of Time and Concentration. *Journal of Colloid and Interface Science* **1972**, *41* (3), 454-465.
109. Wu, Z.; Lee, D.; Rubner, M. F.; Cohen, R. E., Structural Color in Porous, Superhydrophilic, and Self-Cleaning SiO<sub>2</sub>/TiO<sub>2</sub> Bragg Stacks. *Small* **2007**, *3* (8), 1445-1451.
110. Choi, S. Y.; Mamak, M.; von Freymann, G.; Chopra, N.; Ozin, G. A., Mesoporous Bragg Stack Color Tunable Sensors. *Nano Letters* **2006**, *6* (11), 2456-2461.
111. Yaghoubi, H.; Taghavinia, N.; Alamdari, E. K.; Volinsky, A. A., Nanomechanical Properties of TiO<sub>2</sub> Granular Thin Films. *ACS Applied Materials & Interfaces* **2010**, *2* (9), 2629-2636.
112. O'Hayre, R.; Feng, G.; Nix, W. D.; Prinz, F. B., Quantitative Impedance Measurement Using Atomic Force Microscopy. *Journal of Applied Physics* **2004**, *96* (6), 3540-3549.
113. Pauchard, L.; Rica, S., Contact and Compression of Elastic Spherical Shells: The Physics of a 'Ping-Pong' Ball. *Philosophical Magazine Part B* **1998**, *78* (2), 225-233.
114. Gianola, D. S.; Sedlmayr, A.; Monig, R.; Volkert, C. A.; Major, R. C.; Cyrankowski, E.; Asif, S. A. S.; Warren, O. L.; Kraft, O., In Situ Nanomechanical Testing in Focused Ion Beam and Scanning Electron Microscopes. *Review of Scientific Instruments* **2011**, *82* (6), 063901-12.
115. Brugarolas, T.; Gianola, D. S.; Zhang, L.; Campbell, G. M.; Bassani, J. L.; Feng, G.; Lee, D., Tailoring and Understanding the Mechanical Properties of Nanoparticle-Shelled Bubbles. *ACS Applied Materials & Interfaces* **2014**.

116. Carlisle, K. B.; Lewis, M.; Chawla, K. K.; Koopman, M.; Gladysz, G. M., Finite Element Modeling of the Uniaxial Compression Behavior of Carbon Microballoons. *Acta Materialia* **2007**, *55* (7), 2301-2318.
117. Carlisle, K. B.; Koopman, M.; Chawla, K. K.; Kulkarni, R.; Gladysz, G. M.; Lewis, M., Microstructure and Compressive Properties of Carbon Microballoons. *Journal of Materials Science* **2006**, *41* (13), 3987-3997.
118. Gupta, N.; Woldeesenbet, E.; Mensah, P., Compression Properties of Syntactic Foams: Effect of Cenosphere Radius Ratio and Specimen Aspect Ratio. *Composites Part A: Applied Science and Manufacturing* **2004**, *35* (1), 103-111.
119. Lee, D.; Jia, S.; Banerjee, S.; Bevk, J.; Herman, I. P.; Kysar, J. W., Viscoplastic and Granular Behavior in Films of Colloidal Nanocrystals. *Physical Review Letters* **2007**, *98* (2), 026103.
120. Bardella, L.; Genna, F., On the Elastic Behavior of Syntactic Foams. *International Journal of Solids and Structures* **2001**, *38* (40-41), 7235-7260.
121. Chen, Z.; Yan, Q.; Huang, Z.; Shen, Q.; Zhang, L., Preparation and Characterization of Novel Functional Gradient Syntactic Foam. **2009**; Vol. 66, pp 284-287.
122. Glikman, Z.; Altus, E. In *Strain Measurement in Syntactic Foam Using an Embedded Fiber-Optic Sensor*, **2007**; pp 475-483.
123. Xu, W.; Li, G., Constitutive Modeling of Shape Memory Polymer Based Self-Healing Syntactic Foam. *International Journal of Solids and Structures* **2010**, *47* (9), 1306-1316.
124. Xue, X. B.; Zhao, Y. Y.; Kearns, V.; Williams, R. L. In *Mechanical and Biological Properties of Titanium Syntactic Foams*, **2010**; pp 129-135.
125. Prosser, J. H.; Brugarolas, T.; Lee, S.; Nolte, A. J.; Lee, D., Avoiding Cracks in Nanoparticle Films. *Nano Letters* **2012**, *12* (10), 5287-5291.
126. Lee, D.; Rubner, M. F.; Cohen, R. E., All-Nanoparticle Thin-Film Coatings. *Nano Letters* **2006**, *6* (10), 2305-2312.

127. Zhang, L.; Prosser, J. H.; Feng, G.; Lee, D., Mechanical Properties of Atomic Layer Deposition-Reinforced Nanoparticle Thin Films. *Nanoscale* **2012**, *4* (20), 6543-6552.
128. Zhang, L.; Feng, G.; Zeravcic, Z.; Brugarolas, T.; Liu, A. J.; Lee, D., Using Shape Anisotropy to Toughen Disordered Nanoparticle Assemblies. *ACS Nano* **2013**, *7* (9), 8043-8050.
129. Feng, G.; Qu, S.; Huang, Y.; Nix, W. D., An Analytical Expression for the Stress Field around an Elastoplastic Indentation/Contact. *Acta Materialia* **2007**, *55* (9), 2929-2938.
130. Bucaille, J. L.; Stauss, S.; Felder, E.; Michler, J., Determination of Plastic Properties of Metals by Instrumented Indentation Using Different Sharp Indenters. *Acta Materialia* **2003**, *51* (6), 1663-1678.
131. Bassani, J. L., Linear Densification and Microcracking in Sintering Compacts. *Mechanics of Materials* **1991**, *12* (2), 119-130.
132. Datta, S. S.; Kim, S.-H.; Paulose, J.; Abbaspourrad, A.; Nelson, D. R.; Weitz, D. A., Delayed Buckling and Guided Folding of Inhomogeneous Capsules. *Physical Review Letters* **2012**, *109* (13), 134302.
133. Paulose, J.; Nelson, D. R., Buckling Pathways in Spherical Shells with Soft Spots. *Soft Matter* **2013**.
134. Drucker, D. C.; Prager, W., Soil Mechanics and Plastic Analysis or Limit Design. *Q. Appl. Math.* **1952**, *10* (2), 157-165.
135. Alejano, L. R.; Bobet, A., Drucker–Prager Criterion. *Rock Mech Rock Eng* **2012**, *45* (6), 995-999.
136. Lubliner, J., *Plasticity Theory*. Macmillan Publishing: **1990**.
137. Seamark, M. J., Use of Syntactic Foams for Subsea Buoyancy. *Cellular Polymers* **1991**, *10* (4), 308-321.
138. Thomas, C. R., Syntactic Carbon Foams. *Materials Science and Engineering* **1973**, *12* (5–6), 219-233.



139. Luong, D. D.; Strbik Iii, O. M.; Hammond, V. H.; Gupta, N.; Cho, K., Development of High Performance Lightweight Aluminum Alloy/Sic Hollow Sphere Syntactic Foams and Compressive Characterization at Quasi-Static and High Strain Rates. *Journal of Alloys and Compounds* **2013**, *550*, 412-422.
140. Li, G.; John, M., A Self-Healing Smart Syntactic Foam under Multiple Impacts. *Composites Science and Technology* **2008**, *68* (15–16), 3337-3343.
141. Meyers, M. A.; McKittrick, J.; Chen, P.-Y., Structural Biological Materials: Critical Mechanics-Materials Connections. *Science* **2013**, *339* (6121), 773-779.
142. Zegeye, E.; Ghamsari, A. K.; Woldesenbet, E., Mechanical Properties of Graphene Platelets Reinforced Syntactic Foams. *Composites Part B: Engineering* **2014**, *60* (0), 268-273.
143. Lung, C. Y.; Kukk, E.; Matinlinna, J. P., Shear Bond Strength between Resin and Zirconia with Two Different Silane Blends. *Acta Odontologica Scandinavica* **2012**, *70* (5), 405-13.
144. Wouterson, E. M.; Boey, F. Y. C.; Hu, X.; Wong, S.-C., Specific Properties and Fracture Toughness of Syntactic Foam: Effect of Foam Microstructures. *Composites Science and Technology* **2005**, *65* (11–12), 1840-1850.
145. Li, G.; John, M., A Crumb Rubber Modified Syntactic Foam. *Materials Science and Engineering: A* **2008**, *474* (1–2), 390-399.
146. Suh, D.; Choi, S. J.; Lee, H. H., Rigiflex Lithography for Nanostructure Transfer. *Advanced materials* **2005**, *17* (12), 1554-1560.
147. Yoo, P. J.; Choi, S.-J.; Kim, J. H.; Suh, D.; Baek, S. J.; Kim, T. W.; Lee, H. H., Unconventional Patterning with a Modulus-Tunable Mold: From Imprinting to Microcontact Printing. *Chemistry of Materials* **2004**, *16* (24), 5000-5005.
148. *Asm Handbook Volume 8: Mechanical Testing and Evaluation*. ASM International: Materials Park, OH 44073-0002, **2000**.
149. Michael, J. O., 3-Methacryloxypropyltrimethoxysilane. In *Progress in Silicones and Silicone-Modified Materials*, American Chemical Society: **2013**; Chapter 4, pp 47-56.

150. Jo, H.; Blum, F. D., Structure and Adsorption of 3-Acryloxypropyltrimethoxysilane. *Langmuir* **1999**, *15* (7), 2444-2449.
151. Renner, K.; Móczó, J.; Vörös, G.; Pukánszky, B., Quantitative Determination of Interfacial Adhesion in Composites with Strong Bonding. *European Polymer Journal* **2010**, *46* (10), 2000-2004.
152. Demjén, Z.; Pukánszky, B.; Nagy, J., Evaluation of Interfacial Interaction in Polypropylene/Surface Treated Caco3 Composites. *Composites Part A: Applied Science and Manufacturing* **1998**, *29* (3), 323-329.